LUT
Lappeenranta
University of Technology

Elvira Baygildina

THERMAL LOAD ANALYSIS AND MONITORING OF DOUBLY-FED WIND POWER CONVERTERS IN LOW WIND SPEED CONDITIONS

Thesis for the degree of Doctor of Science (Technology) to be presented with due permission for public examination and criticism in the Auditorium of the Student Union House at Lappeenranta University of Technology, Lappeenranta, Finland on the 30th of November, 2017, at noon.

Acta Universitatis
Lappeenrantaensis 770

Supervisors Professor Olli Pyrhönen
LUT School of Energy Systems
Lappeenranta University of Technology
Finland

Reviewers Professor Stig Munk-Nielsen
Department of Energy Technology
Aalborg University
Denmark

Professor Teuvo Suntio
Department of Electrical Engineering
Tampere University of Technology
Finland

Opponent Professor Roy Nilsen
Department of Electric Power Engineering
Norwegian University of Science and Technology
Norway

ISBN 978-952-335-157-8
ISBN 978-952-335-158-5 (PDF)
ISSN-L 1456-4491
ISSN 1456-4491

Lappeenrannan teknillinen yliopisto
Yliopistopaino 2017

Abstract

Elvira Baygildina
Lappeenranta 2017
149 pages
Acta Universitatis Lappeenrantaensis 770
Diss. Lappeenranta University of Technology
ISBN 978-952-335-157-8, ISBN 978-952-335-158-5 (PDF),
ISSN-L 1456-4491, ISSN 1456-4491

State-of-the-art wind power technology allows multi-megawatt installations in low wind areas. Meanwhile, the present development is focused on aerodynamic improvement, enhanced efficiency, and reliability. Research is carried out on power electronics reliability issues of wind turbines installed on low wind speed sites. Reliability issues associated with power electronics arise as a result of the increasing power capacity of a single wind turbine, which also increases the power density of the module. The power converter as part of a doubly-fed induction generator (DFIG) based wind turbine (WT) is subjected to a considerable thermal stress, especially, in operation close to and at the synchronous operating point. Moreover, low wind speed conditions and a high turbulence level make the power electronics more vulnerable, thereby inducing degradation mechanisms and reducing its lifetime.

A comprehensive method to perform a mission-oriented reliability analysis of a wind power converter covers three areas of research, namely the wind speed characteristics, the DFIG operation, and the failure mechanisms of the power electronics. A lifetime estimation method for the insulated-gate bipolar transistor (IGBT) is implemented. The method comprises transformation steps from the turbulent wind speed profile, the wind turbine dynamic response, the corresponding power converter thermal stress, and the consumed lifetime estimation. The modelling results show that the thermal stress of the power converter is considerably affected by the low operating frequency of the rotor circuit and the bidirectional flow of the rotor power. The obtained results for the lifetime consumption indicate that an IGBT failure caused by the bond wire lift-off has a higher probability than a failure resulting from solder fatigue. Additionally, the strong influence of the site-specific wind characteristics on the lifetime consumption is demonstrated.

In the present research, application of a gradient heat flux sensor (GHFS) in power electronics is analysed. The GHFS, thanks to its thinness, can be attached between the power device base plate and the heat sink, and it provides direct heat flux measurements. The test results are compared with the modelled IGBT power losses, and a good accuracy is found between them. Furthermore, the GHFS is used to detect power device degradation, and consequently, a possible solution is proposed for the GHFS-based condition monitoring system implemented in the WT.

Keywords: turbulence intensity, wind speed, power electronics, thermal analysis, lifetime estimation, reliability, IGBT, failure mechanism, doubly-fed induction generator, gradient heat flux sensor, condition monitoring.

Acknowledgements

This doctoral dissertation covers research carried out at Lappeenranta University of Technology, Finland, between 2011 and 2017. I would like to gratefully thank my supervisors, Professor Olli Pyrhönen, Dr. Katja Hynynen, and Dr. Pasi Peltoniemi for their continuing support over the years and promoting a passion for wind energy. I am also very grateful to Professor Andrey Mityakov and Dr. Mikko Kuisma for the technical support in constructing the test setup.

I express my special thanks to the preliminary examiners, Professor Stig Munk-Nielsen from Aalborg University, Denmark and Professor Teuvo Suntio from Tampere University of Technology, Finland. Special thanks to Professor Roy Nilsen from Norwegian University of Science and Technology for coming to Finland and acting as an opponent in the public examination of my doctoral dissertation.

I am very grateful to the colleagues from Alstom, Barcelona, for the fruitful collaboration and sharing your experience in the wind energy.

I also thank Dr. Hanna Niemelä for improving the English language in my papers and this doctoral dissertation. I am very grateful to Ms. Piipa Virkki and Ms. Tarja Sipiläinen for organizing the working space, conference trips, and the defence ceremony.

I express my gratitude to Professors Ke Ma and Frede Blaabjerg and my colleagues at Aalborg University.

I would like to thank all my friends, who were with me over these years in Lappeenranta. I am also very grateful to the mothers' society in Säkylä for their peer support and having nice time with conversations.

Finally, I am very grateful to my family: my parents, my sister, my husband Aleksandr Buzakov, and my daughter, Ekaterina, for the countenance, patience, and love!

Elvira Baygildina
November 2017
Lappeenranta, Finland

Contents

Nomenclature

Latin symbols

$A_{\mathrm{baseplate}}$	base plate area
Al	aluminium
Al_2O_3	aluminium oxide
AlN	aluminium nitride
AlSiC	aluminium silicon corbide
A_{r}	area swept by the rotor blades
A_{sensor}	area of the heat flux sensor
c	scale parameter
C_{DC}	DC link capacitance
C_{f}	filter capacitance
CL	consumed lifetime
C_{p}	power coefficient
$C_{\mathrm{p\_max}}$	maximum power coefficient
C_{p}^{*}	desired power coefficient
Cu	copper
D	bond wire diameter
E_{a}	activation energy
E_{on}	turn-on loss
E_{on}	turn-off loss
E_{r}	induced electromotive force in the rotor
E_{s}	induced electromotive force in the stator
E_{sw}	switching energy
E_{th}	thermo-electromotive force
f_{s}	synchronous frequency
f_{sw}	switching frequency
F_{c}	centrifugal force
Fr	friction force
I	current
I_{c}	collector current
I_{cf}	capacitor current of the filter
I_{f}	filter current on the inverter side
I_{fw}	diode forward current
I_{g}	filter current on the grid side
I_{r}	rotor current
I_{s}	stator current
J_{t}	total moment of inertia
j	imaginary unit
k	shape parameter
K_{F}	static gain of the von Karman shaping filter

K_s	stator winding factor
k_{sr}	turns ratio between stator and rotor
K_r	rotor winding factor
L_{f1}	inverter-side inductance of the filter
L_{f2}	grid-side inductance of the filter
L_{lr}	rotor leakage inductance
L_{ls}	stator leakage inductance
m	modulation index and the phase angle φ
N	number of elements
N_{gear}	gear ratio
N_f	number of cycles to failure
n_p	number of pole pairs
N_s	number of turns in the stator
N_r	number of turns in the rotor
Pb	lead
P_{cond}	conduction loss
P_{conv}	converter power
P_f	power delivered to the filter
P_{loss}	power loss
P_m	mechanical power
P_r	rotor power
P_s	stator power
P_{sw}	switching loss
P_v	wind power
Q	reactive power
q	heat flux density
r	rotor radius
R	Boltzmann constant
R_{br}	brake resistor
R_{ce}	on-state resistance
R_{f1}	filter resistance on the inverter side
R_{f2}	filter resistance on the grid side
R_{f3}	filter resistance of the RC branch
R_s	stator resistance
R_r	rotor resistance
R_{th}	thermal resistance
s	slip
S	apparent power
S_0	volt-watt HFS sensitivity
Si	silicon
Sn	tin
T_a	aerodynamic torque
T_{amb}	ambient temperature

T_{c}	case temperature
T_{em}	generator electromagnetic torque
T_{F}	integral time scale
T_{g}	generator torque on the low-speed side of the gearbox
T_{g}^{*}	reference generator torque on the low-speed side of the gearbox
$T_{\mathrm{heat\ sink}}$	heat sink temperature
T_{j}	junction temperature
T_{jmax}	maximum junction temperature
T_{m}	mean junction temperature
T_{mech}	mechanical torque on the high speed side of the gearbox
t_{on}	heating time
U	voltage
U_{CE}	collector-emitter voltage
U_{CE0}	collector-emitter threshold voltage
$U_{\mathrm{ce,sat}}$	collector-emitter saturation voltage
U_{cf}	filter voltage of the RC branch
U_{DC}	DC link voltage
U_{f}	filter voltage on the inverter side
U_{g}	filter voltage on the grid side
U_{ge}	gate-emitter voltage
U_{r}	rotor voltage
U_{s}	stator voltage
v	wind speed
$\bar{v}$	mean wind speed
v_i	*i*-element of the wind speed row data
v_{t}	turbulent component of the wind
$Z_{\mathrm{c-h}}$	thermal impedance from the case to the heat sink
$Z_{\mathrm{h-amb}}$	thermal impedance from the heat sink to ambient
$Z_{\mathrm{j-c}}$	thermal impedance from the junction to the case

Latin symbols

β	blade pitch angle
β^{*}	reference blade pitch angle
ΔT_{j}	junction temperature change
λ	tip speed ratio
λ_{opt}	optimal tip speed ratio
λ^{*}	tip speed ratio
ρ	air density
σ	standard deviation
ϕ_{m}	magnetizing flux
φ	power factor angle
Ψ_{r}	rotor flux

Ψ_s	stator flux
ω_c	cut-off frequency
ω_m	mechanical rotational speed
ω_{g_min}	minimum generator rotational speed
ω_{g_max}	maximum generator rotational speed
ω_r	rotor angular frequency
ω_s	synchronous angular frequency
ω_{slip}	slip frequency

Superscripts

s	stator reference frame

Subscripts

est	estimated
d	d-axis
q	q-axis
r	rotor
s	stator

Abbreviations

3D	three-dimensional
AEP	annual energy production
BTB	back-to-back
CF	Coriolis force
CM	condition monitoring
CTE	coefficient of thermal expansion
DC	direct current
DCB	direct copper bonded
DF	doubly-fed
DFIG	doubly-fed induction generator
DS	Danish standard
EESG	electrically excited synchronous generator
FEM	finite-element method
GHFS	gradient heat flux sensor
HFS	heat flux sensor
GL	Germanischer Lloyd
GSC	grid-side converter
IGBT	insulated-gate bipolar transistor
IEC	international electrotechnical commission
LIDAR	light detection and ranging
LWK	Landwirtschaftskammer Schleswig-Holstein
PDE	partial differential equations

PDF	probability density function
PGF	pressure gradient force
PMSG	permanent magnet synchronous generator
rms	root mean square
RSC	rotor-side converter
SG	synchronous generator
TI	turbulence intensity
TSEP	temperature sensitive electrical parameter
WT	wind turbine
WMEP	Wissenschaftliches Mess- und Evaluierungsprogramm

1 Introduction

1.1 Background

Remarkable growth has been achieved in the global wind power capacity over the last few decades. With the aim of reducing greenhouse gas emissions, wind power systems actively penetrate into distribution networks in order to replace or sustain a balance with fossil-based power generation systems. However, the decade-long low prices of fossil fuels, issues with the market integration, and the lack of political and public acceptance constitute the main barriers to the wind energy integration. Until now, the global installed wind power capacity has reached a level of 487 GW with 55 GW installed in 2016 (GWEC, 2016).

Recent advances in the wind power technology contribute to an increasing efficiency and allow implementation of wind power on sites in low wind areas. Economic and technical feasibility makes the wind power cost competitive among the other sources of energy. Here, the state policies play a leading role in the wind power integration and provide long-term planning and financial support.

In order to reduce the price per kWh of the produced energy, the power capacity of a single wind turbine (WT) is being increased. At present, the most common WT size is 1.5–3 MW. However, larger-scale WTs have been developed over the last years. In 2016, the Danish manufacturer Vestas installed the first offshore V164–8.0 MW (VestasOffshore, 2016) wind turbine. Meanwhile, Siemens is working on a 10 MW prototype and planning to complete the development in 2020 (Torsten, 2015).

The present large-scale WTs are based on variable-speed operation. The advantage of variable speed over fixed speed WTs is an increased energy capture, and thus, the gain in energy production can reach 28 % (Mutschler & Hoffinann, 2002). Moreover, fixed-speed operation is considered unfeasible for large-scale application (Ackermann & Söder, 2002). Variable-speed operation reduces mechanical loads and ensures better compliance with grid codes owing to the ability of power control by power electronics.

It is reasonable to classify the current variable-speed WT technologies based on power converter ratings, in other words, into partial- and full-scale power converters. Partial-scale converters are used in doubly-fed induction generator (DFIG) systems. This configuration was first adopted in variable-speed WTs by Vestas in the early 2000s, and it remains the dominating topology in the market. The stator of the DFIG is connected to the grid. The wound rotor of the DFIG is connected to the grid by a back-to-back (BTB) power converter. The reduced-scale power electronics typically accounts for one-third of the total power. Depending on the generator slip, the BTB power electronics delivers power to the grid or feeds the rotor. Therefore, the rotational speed range is limited by the slip. In order to produce the high-speed revolutions of the rotor, a gearbox is required. The wound rotor uses slip rings to be connected to the frequency converter.

Full-scale power converters are mostly used in WT systems equipped with a synchronous generator (SG) either as an electrically excited (EESG) or based on permanent magnets (PMSG). The operating speed range is higher than in the DFIG topology and limited only by the nominal speed. The power converter provides the decoupling interface between the generator and the grid. The full control of the active and reactive power offers an opportunity to meet the grid requirements.

For multi-MW range WTs, the PMSG technology is an attractive solution because of the better ability to meet the stringent grid requirements, elimination of the gearbox and slip rings, and the wider operating speed range.

However, the major players in the wind energy market, such as Vestas and GE Energy, are still supplying DFIG-based WTs (Blaabjerg & Ma, 2013). The partial-scale power electronics makes this solution cost effective. In 2010, 55 % of the total installed wind power capacity was based on doubly-fed drives (Van Hulle & Fichaux, 2010). Table 1.1 lists manufacturers that produce WTs based on the DFIG technology. Obviously, most of the DFIG-based WTs of leading the manufactures are in the range of 1–3 MW.

Table 1.1: Examples of DFIG-based wind turbines produced in 2016.

Manufacturer	Turbine model	Nominal Power, MW	Wind class
DeWind	DeWind D6.0	1.25	IIA/IIIA
	DeWind D8.0	2.0	IIA/IIIA
GE Wind Energy	GE 1.7-100/103	1.7	III
	GE 1.85-82.5/87	1.85	II
	GE 2.75-120*	2.75	III
	GE 2.0-2.4	2.0-2.4	IIS/IIIS
	GE 3.2-103/130	3.2	II/IIIA
	GE 3.4-130/137	3.4	IIB/IIIB
	ECO 100	3.0	IA
	ECO 110	3.0	IIA, IS
	ECO 120	2.7/3.0	IIIA, IIB
Nordex	N117/2400	2.4	III
	N90/2500	2.5	I
	N100/2500	2.5	II
	N117/3000	3.0	II
	N131/3000	3.0	III
	N100/3300	3.3	I
Vestas	V90-1.8/2.0 MW	1.8/2.0	IIA/IIIA
	V100-1.8/2.0 MW	1.8/2.0	IIIA/IIB
	V110-2.0 MW	2.0	IIIA
	V90-3.0 MW	3	IA/IIA

1.2 Motivation

1.2.1 Power electronics reliability

The tendency of increasing WT capacity incorporates reliability problems arising from the significant growth of the power density of electrical components. Numerous research groups and projects, such as Landwirtschaftskammer Schleswig-Holstein (LWK), Wissenschaftliches Mess- und Evaluierungsprogramm (WMEP), and VTT Technical Research Centre collect failure databases, analyse WT reliability in terms of failure rates, downtimes, failure reasons, and availability over the WT lifetime (Sheng, 2013). According to the failure statistics collected based on data from European inland wind farms over 13 years (1993–2006), presented by LWK and WMEP, the electrical system has the highest failure rate (Figure 1.1) (Tavner, 2011). Here, the electrical system includes for instance the converter, fuses, and the electronic control unit. According to a WMEP report, the distribution of failure rates among electrical system components is uniform (Faulstich et al., 2010). Among other WT subsystems, the gearbox requires the longest downtime after failure.

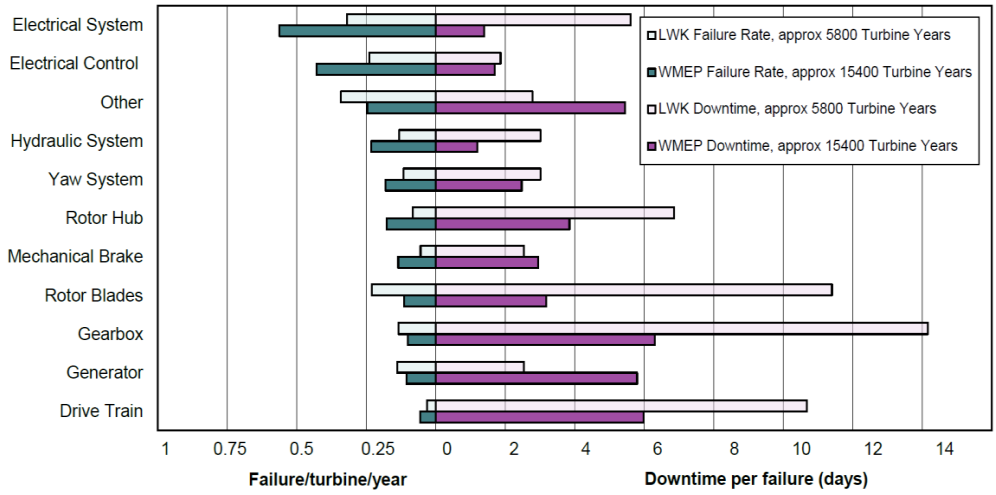

Figure 1.1: Failure rate and downtime of WT subsystems calculated based on data collected over 13 years from European inland wind farms (Tavner, 2011).

When studying reliability problems of the power electronics semiconductors, it is worth paying attention to common failure mechanisms that cause failures. In (Yang et al., 2010), the power electronics failure mechanisms are classified into chip-related and package-related failures.

The chip-related failure mechanism may occur during electrical overstress, when the operation exceeds the limits of safe operating area, for instance, overvoltage, overcurrent,

and fast transients during switching (Yang et al., 2010). This may result in critical thermal stress and lead to failure.

A variety of chip-related failure mechanisms are also associated with anomalies in the charge conductive channels of the device (Patil et al., 2008). Breakdown of the gate oxide occurs due to a puncture of drain charges during electrostatic discharge or hot electron injection in high-temperature operation (Duvvury et al., 1994). In the multilayer structure of the metal-oxide-semiconductor field-effect transistors (MOSFETs), the parasitic bipolar-junction transistor may trigger if high-density current or a large value of dv/dt is applied. In the same manner, latch-up of the parasitic thyristor in the insulated-gate bipolar transistor (IGBT) structure may occur (Valentine et al., 2015). As a result, an uncontrollable operating condition of the device may cause damage.

In (Yang et al., 2010), other failure mechanisms, rarely observed in power electronics, are described. These are electromigration of the conducting material as a result of the moving electrons and a strike of cosmic radiation, especially in high-voltage power modules.

Package-related failures have been intensively studied by (Yang et al., 2010) and (Ciappa, 2002). Two basic failure mechanisms are distinguished in power modules; bond wire lift-off or breakage and solder degradation. Both failure mechanisms are caused by a thermo-mechanical wear-out process, where the contacting materials with different coefficients of thermal expansion (CTE) experience periodical expansions and contractions. As a result, crack propagation and subsequent delamination of two contacting materials can be observed in the solder joints and the bond wire connections. This leads to bond wire lift-off or bond wire heal cracking. Details of the thermomechanical-stress-related failure mechanisms are discussed in Section 1.2.2.

Besides bond wire breakage and solder fatigue, which most frequently occur in power modules, degradation of the thermal grease, formation of tin whiskers, and fretting corrosion are considered package-related failure mechanisms (Fischer et al., 2012). Thermal grease is used as an interface between the base plate and the heat sink. The grease tends to pump out and dry out, thereby decreasing thermal conductivity. Tin whiskers are usually formed at the lead-free solder interface as microscale metal hairs, which may cause a short-circuit. An alloy with lead can significantly prevent the formation of whiskers. Fretting corrosion takes place in the contact of two metal surfaces. Corrosion is initiated by oxide particles trapped in the contact interface, causing an open circuit.

In (Fischer et al., 2014), an overview of failure factors of power electronics for independent application is given (Figure 1.2). According to (Fischer et al., 2014), in order to investigate prevailing failures, the following multi-track approach can be applied. It covers an analysis of failure rates (correlation with turbine types, seasons, ambient temperature, relative humidity, wind speed, and lighting strikes), an analysis of the operating conditions inside cabinets (temperature and relative humidity), and a post-operational analysis (forensic analysis or measurement of electrical parameters).

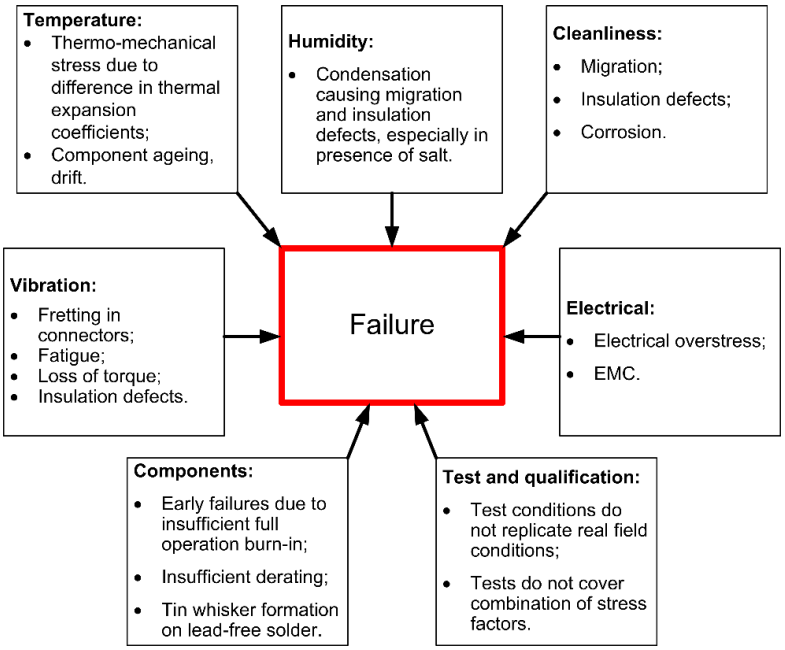

Figure 1.2: Failure factors of power electronics (Fischer et al., 2014).

External factors of WT power electronics failures, such as wind speed, ambient temperature, and operating conditions inside converter cabinets (humidity, temperature, and dew point), have been considered in (Fischer et al., 2012). The correlation of the failure rate with external factors has been found to be stronger in IG-type WTs than in DFIG WTs. Additionally, condensation inside power cabinets after a long standstill period and lightning strikes increases the risk of failure.

However, thermal stress has been found to be the main factor of reliability reduction in power electronics (Blaabjerg et al., 2012). According to (Birk & Andresen, 2008), the failures of power electronics in WTs, unlike in most of the power electronics applications, are strongly dependent on thermal loads. Increased current ratings per chip and the reduced size of the power semiconductors require advanced thermal management, that is, a higher maximum allowed junction temperature and an improved cooling system solution (Chamund et al., 2009). In Section 1.2.2, the package-related failures of the IGBT module caused by thermal stress are discussed.

1.2.2 IGBT module failure mechanisms caused by thermal loading

In principle, thermal loading is affected by two main factors (Ma et al., 2015). First, the power device operates at a specific load current, switching frequency, modulation index, power factor, and DC link voltage. Thus, dynamic electrical loading induces power loss dissipation in the module and causes junction temperature fluctuations. Another factor

affecting thermal loading is the device rating. High current and voltage ratings of the semiconductor significantly increase the power loss (Roshanfekr et al., 2012), (Ma et al., 2015). Hence, in (Roshanfekr et al., 2012) it was reported that a power loss increase in the converter reached 67 % with IGBT modules of a rated voltage of 6.5 kV instead of 1.7 kV.

It is pointed out that the power loss generation and the reliability performance are highly dependent on the IGBT technology. In a low-voltage system with a high switching frequency, as in this research, an IGBT module and the IGBT press-pack topology are preferred (Senturk, 2011). The press-pack technology has a more rigid structure, achieved by the individual spring-contacted chips (Figure 1.3) and by avoiding the bond wires and solder joints, as in the IGBT module. In Figure 1.3, the silicon (Si) chips are enclosed between the conductive top and base plates. The contact piston presses the top plate and the chip against the base plate. The structure is held together between the module housing power connections and the electrically isolated housing element (Gunturi & Schneider, 2009). The CTE of the top and bottom base plates is close to or matches that of the silicon chips.

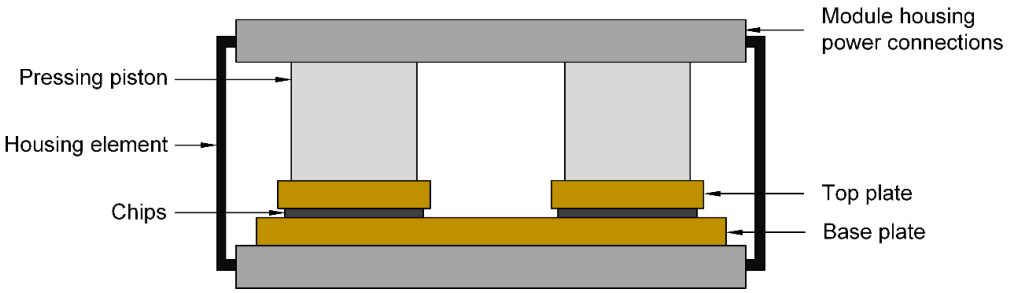

Figure 1.3: Press-pack IGBT submodule structure (Gunturi & Schneider, 2009)

However, the IGBT module topology has less mounting arrangement and is cheaper than the press-pack IGBT. The IGBT module also has a longer track record of application and is still dominant in high-power applications (Ma & Blaabjerg, 2012). Thus, in the present research, the IGBT module is considered. The package-related failures, associated with different thermal properties of the materials used in the module, are discussed.

In Figure 1.4, the cross-sectional structure of the IGBT module is presented. The Si chips are connected with aluminium (Al) bond wires through an Al metallization layer (not shown in the figure). The chips are soldered on a copper (Cu) layer, which forms the IGBT circuitry pattern. A ceramic substrate, made of aluminium oxide (Al_2O_3) or aluminium nitride (AlN), with bonded copper on the both sides forms the direct copper-bonded (DCB) substrate. The ceramic substrate provides an electrical isolation, and the copper layers decrease the thermal resistance of the device (Ikonen, 2012). The copper base plate is soldered to the DCB substrate. Local temperature fluctuations between the layers cause thermo-mechanical fatigue stress as a result of the continuing expansion and

contraction of the material. In Table 1.2, the CTEs of the materials typically used in the IGBT module are presented (Khanna, 2003).

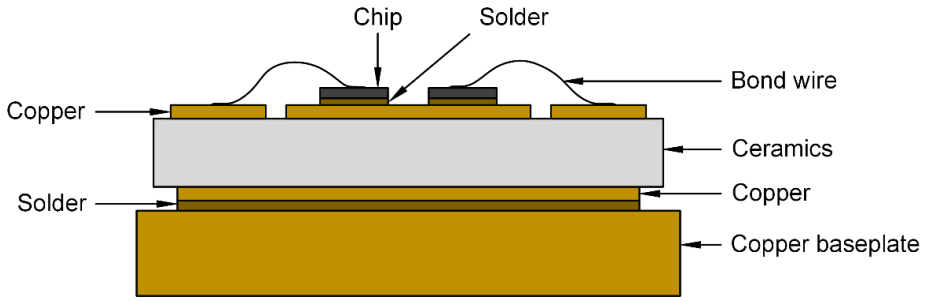

Figure 1.4: Structure of the IGBT module.

Table 1.2: Coefficients of thermal expansion (CTE) of the materials typically used in the IGBT module (Khanna, 2003).

Material	Symbol	CTE (ppm/K)	Function
Silicon	Si	2.6	Material for IGBT chip fabrication
Aluminium	Al	23	Bond wires and metallization
Aluminium oxide	Al_2O_3	10.7	Substrate material
Aluminium nitride	AlN	3.1	Substrate material
Copper	Cu	16	Base plate
Aluminium silicon carbide	AlSiC	7	Base plate
Lead-tin solder	63 % Pb, 37 % Sn	13	Die mounting
Thermal grease	–	0.4-1	Thermal contact between base plate and heat sink

The greatest mismatch in the CTEs of the two stack materials is between the Al bond wires and metallization and the silicon chips. The CTE of aluminium (23 ppm/K) is about nine times that of silicon (2.6 ppm/K), in other words, aluminium expands more than silicon. Thus, the bonded interface between the layers is exposed to the propagation of fractures. Moreover, high temperature fluctuations result in reconstruction of the Al metallization layer. Finally, the resultant degradation of the contacting areas caused by crack propagation leads to bond wire lift-off (Ciappa, 2002) (Figure 1.5).

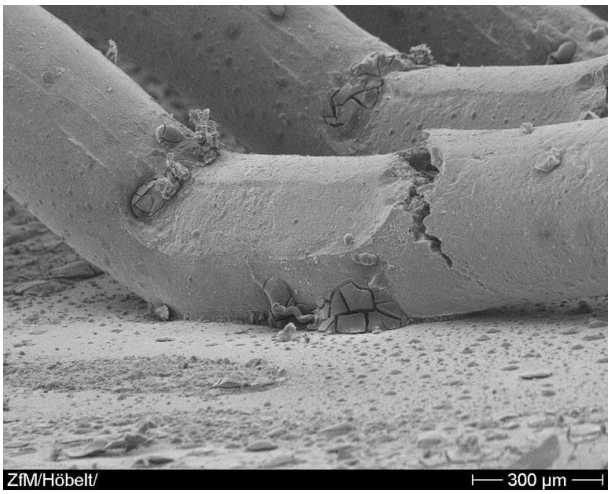

Figure 1.5: Heal cracking and trace of a lifted bond wire of a diode (Amro & Lutz, 2004).

Usually, multiple bond wires are positioned in parallel on the chip in order to relieve the current load and prevent excessive ohmic heating. Under normal operating conditions, the maximum current capability of a single Al wire is 10 A (Ciappa, 2002). The bond wire, which has lost connection with the chip, induces additional current load in the normally operating wires. Thus, the current will be uniformly distributed among the other bond wires. However, after the bond wire lift-off, the temperature distribution over the chip will not be uniform. The non-uniform temperature distribution induces further bond wire breakage. According to (Chen et al., 2012), the bond wires continue to fail from the centre of the chip to the edges.

Methods to improve the bond wire connection are discussed in (Ciappa, 2002). These are application of a molybdenum-aluminium (Mo-Al) layer between the Si chip and the bond wire in order to improve distribution of the mismatch in the CTEs, and covering the bond wire with polymeric coating to eliminate physical separation of the bond wire feet from the chip.

The difference in the CTEs of the silicon chip and the copper substrate also leads to deformation of the bonding interface (CTEs 2.6 and 16 ppm/K). Here, formation of voids and cracks occurs in the solder interface between the silicon chip and the copper base plate. The same degradation mechanism takes place in the solder layer between the ceramic substrate and the copper base plate (CTEs 5.5 (Al_2O_3) and 16 ppm/K). In particular, crack formation occurs from the periphery to the central region of the solder layer (Figure 1.6) as a result of a higher shear stress on the edges of the solder interface (Ciappa, 2002). After the solder delamination has started, the ageing process accelerates as a result of the increase in the thermal resistance and the temperature difference in the module.

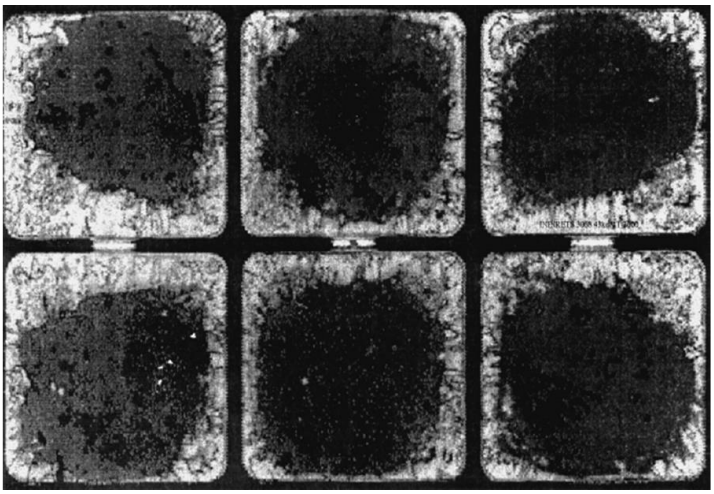

Figure 1.6: Solder degradation (bright areas), delamination of the layer starting from the corners towards the centres (Perpiñà et al., 2012).

The most critical solder connection is found between the ceramic substrate (Al_2O_3) and the Cu base plate because of its large lateral size. The reliability of the solder joints can be improved by reducing the areas of attachments, and therefore, the DCB is often divided into several parts. Thus, the connection of the copper base plate and the DCB could be improved by reducing the average difference in thermal expansions (Wintrich et al., 2015). Additionally, it is possible to increase the thickness of the solder, thereby reducing the material stress on the edges (Ciappa, 2002). Combination of the AlN substrate and the AlSiC base plate would give better matching between CTEs. Moreover, the AlN substrate is the best combination with silicon chips (Wintrich et al., 2015).

1.2.3 **IGBT lifetime prediction**

In order to meet the reliability requirements for the semiconductor power devices, lifetime prediction has become an essential step in the power device development.

A well-known method to estimate the lifetime is to carry out accelerated tests, during which the loading conditions are more critical than in a real-life application. In (Cova & Fantini, 1998) and (Held et al., 1997), the lifetime of the IGBT power module is defined by accelerated tests, where short power cycles are applied with controlled junction temperature changes ΔT_j, and maximum junction temperatures T_jmax. In the test setup, a square-wave collector current is applied, and the junction temperature is defined by using a temperature-sensitive electrical parameter (TSEP), more specifically, the collector-emitter voltage. In the tests, an increase in the thermal resistance has been observed, and the final observation has shown both bond wire lift-off, in other words, bond wire vertical

displacement, which indicates an early stage of degradation, and reconstruction of the chip metallization.

A more sophisticated approach is to use an analytical model based on the thermomechanical characteristics of the device. The analytical model uses a stress-strain relationship. The widely known Coffin-Manson law relates the number of cycles to the failure N_f

$$N_\mathrm{f} = A \cdot \Delta T_\mathrm{j}^{-\mathrm{n}} \cdot e^{\frac{E_\mathrm{a}}{RT_\mathrm{m}}}, \tag{1.1}$$

as a function of the junction temperature changes ΔT_j and the mean value T_m, and it also takes into account the material specific parameters. A and n are constants depending on the mechanical properties of the material, E_a is the activation energy, and R is the Boltzmann constant. Activation energy is the minimum energy required to start fatigue deformation. The Arrhenius term $e^{\frac{E_\mathrm{a}}{RT_\mathrm{m}}}$ describes the strong lifetime dependence on the mean junction temperature (Kovačević et al., 2010).

However, as stated in (Ciappa, 2000), the degradation mechanisms in bond wires and solder joints depend on the thermal cycle duration, because relaxation of the thermomechanical stress in bond wires and solder joints is characterized by the distinct time constants (in the order of seconds in bond wires and a minute in solder joints). Thus, the period of a thermal cycle is also an essential term in the lifetime model. In (Bayerer et al., 2008), the lifetime model includes more operating conditions, such as the heating time t_on, the applied current I, the blocking voltage U, and the bond wire diameter D. Such a comprehensive approach requires additional effort to control the set of parameters in the tests, and the number of cycles to failure is expressed as

$$N_\mathrm{f} = K \cdot \Delta T_\mathrm{j}^{\beta_1} \cdot e^{\frac{\beta_2}{T\mathrm{max}}} \cdot t_\mathrm{on}^{\beta_3} \cdot I^{\beta_4} \cdot U^{\beta_5} \cdot D^{\beta_6}, \tag{1.2}$$

where T_max is the maximum junction temperature, and $\beta_1 \ldots \beta_5$ and K are the curve fitting parameters.

When considering whether the aforementioned lifetime model is reasonable to apply, the Coffin-Manson model is preferred owing to the relatively low number of parameters. For this reason, this lifetime model will be used in the present research.

The power device in the wind power application experiences an arbitrary mission profile. Therefore, the actual distribution of temperature changes is non-uniform. The temperature cycles in the time domain have to be transformed to a sequence of temperature cycles, where each counted cycle causes an individual damage to the power device. For lifetime prediction, Miner's rule is applied (Hashin & Rotem, 1977). It is used to describe damage

accumulation, where the total damage is the additive of each individual damage, produced by each thermal cycle.

The power electronics reliability study, oriented to the WT mission profile, has been of special interest of the recent research (Ma et al., 2015), (Ikonen, 2012). Thermal cycles, experienced by the IGBT, contain fluctuations of different derivations and time constants. Particularly, the junction temperature can be expanded to the long-term, medium-term, and short-term variations. Long-term variations are caused by annual ambient temperature and seasonal wind speed changes. Medium-term variations depend on the behaviour of the WT mechanical system. Here, the rotational speed, the converter fundamental frequency, and the corresponding effect on the junction temperature should be addressed. Thus, the WT abilities to track the wind speed changes, which depend on the WT moment of inertia, should be taken into account. Finally, short-term variations are driven by the IGBT switching. Hence, the load profile can be generated for three different cases, and the resultant lifetime can be defined by calculating the number of cycles (Ma et al., 2015). In this research, the medium WT dynamics is considered in order to estimate the IGBT module lifetime. The lifetime model used is based on the numerical look-up tables provided by the IGBT module manufacturer. The look-up tables are built based on the Coffin-Manson law and the degradation of the joint caused by plastic deformation (ABB, 2014a).

1.2.4 IGBT thermal stress in a doubly-fed wind power converter

As shown in Table 1.1, most of the DFIG-based WTs are designed for the IEC II or III wind class conditions. This means that assumptions are made on the specific conditions of the mean wind speed and the turbulence level (IEC, 2005). Thus, the class II wind site assumes an average wind speed of 8.5 m/s, and turbulence intensities of 18 % and 16 % for the IIA and IIB wind classes, respectively. The WTs of the wind class III are designed for high energy capture on less windy sites, with an average wind speed of 7.5 m/s, and turbulence intensities of 18 % and 16 % for the IIIA and IIIB wind classes, respectively.

The WTs with the DF drives, which are installed on a site with low wind speed conditions, are subjected to severe thermal cycling at the RSC. More specifically, the RSC operates in a low fundamental frequency range, usually within ±30 % of the line frequency. Therefore, the converter experiences a load current within a ±15 Hz frequency range. The temperature fluctuations in power semiconductors can be high, because under such low frequencies the sine wave cycle period of the converter current can be higher than the thermal time constant of the semiconductor, and thus, the junction temperature can follow the sine wave of the converter current (Wei et al., 2011). In this case, the junction temperature fluctuations may be even higher than at the rated power operating point (Weiss & Eckel, 2013).

Since the DFIG implies bidirectional current flow in the converter, there is unequal distribution of power loss between the diode and the IGBT. In the super-synchronous mode, the GSC operates as an inverter, and therefore, the IGBT is more loaded than the

diode. The RSC operating in the rectifying mode has a freewheeling diode with more thermal loss than the IGBT (Zhou et al., 2012). Thus, the diode of the RSC can have a higher mean temperature than the IGBT in the super-synchronous area, while at the GSC there is an opposite relation. At the synchronous operating point, the thermal stress of the power devices is highly unbalanced among the phase legs. Taking into consideration the site-specific profiles of the wind classes II and III, the converter may operate most of the lifetime within the maximum thermal stressing zone. Particularly, the average wind speeds of the II and III wind classes are 8.5 and 7.5 m/s, respectively, which can be in the vicinity to the synchronous operating point. In (Bartram et al., 2004), it was shown that the lifetime of a power semiconductor operating in critical conditions can be reduced to 3–7 years.

Therefore, the reliability prediction is an inevitable step in the design process and lifetime estimation of power semiconductors. A complete reliability model of the power semiconductor should include an analysis of the WT loading conditions on a specific site, considering the thermal stress driven by different time constant dynamics. The dominant failure mechanisms of the IGBT should be addressed in the lifetime estimation. The thermal loading should be measured by implementing an appropriate online sensing circuit in order to detect the semiconductor wear-out and avoid a failure.

1.2.5 **Heat flux sensor as a tool to improve the IGBT reliability**

Heat flux measurement has become a sophisticated solution to monitor thermal stress in modern industries and the human environment. Although the temperature measurement is a more usual and conventional way to access the thermal properties of the material, the heat flux is a crucial parameter in systems where the heat dynamics and direction of the heat flow are of importance.

The IGBT lifetime estimation methods, as described previously, are related to the temperature load profile. The heat flux sensors (HFSs) can significantly facilitate the lifetime estimation procedure by direct measurement of the IGBT power dissipation. Thus, with the known thermal model parameters, the junction temperature can be estimated. The power loss dynamics is characterized by the high switching frequency, the rotational-speed-dependent fundamental frequency at the RSC, and the grid frequency at the GSC. Because of the smoothing effect of the thermal impedance, the HFS will reflect the thermal variations with a limited bandwidth. This fact should be taken into account when comparing the power losses and the heat flux measurements.

Moreover, the heat flux measurements can provide a feedback signal for the cooling system to control the thermal energy transfer. In (Wang et al., 2013), an active cooling system is implemented to reduce the junction temperature variations. Alternatively, the heat sink temperature variation can be smoothed by controlling the liquid cooling (Smirnova, 2015). Both the methods result in an increase in the IGBT lifetime.

Two basic categories of the HFSs are distinguished by (Diller, 1999). These are heat flux measurements based on the spatial temperature distribution and temporal temperature transients. Some of the present heat flux sensors are described in brief below.

The operating principle of the first HFS category is based on the measurement of the temperature difference over the thermal barrier layer. Here, series-connected thermocouples (thermopiles) or temperature sensitive resistors are used for the temperature measurements.

The measurement method of the second category of HFSs is based on temperature transients. Here, temperature sensitive resistors (TSR), coaxial thermocouples, or thin film gauges can be used. The heat flux is defined based on the recorded temperature history applying an analytical model with known thermal properties of the material (Olivier, 2003). Compared with HFSs based on thermocouples, these HFSs have a slower time response. In addition, if the temperature measurements are subjected to electromagnetic noise, the latter could produce a large calculation error as the time derivative of the temperature is used to define the heat flux.

In this chapter, a new category of heat flux sensors introduced by (Mityakov et al., 2012), a gradient heat flux sensor (GHFS), is studied. The operating principle of the GHFS is based on the transverse Seebeck effect, where the thermo-electromotive force (thermo-EMF) and the heat flux vectors are perpendicular to each other owing to the anisotropic properties of the sensor material. The HFS is formed by tilted layered plates of bismuth crystal in such a way that the penetrating heat flux induces a transverse thermo-EMF (Figure 1.7).

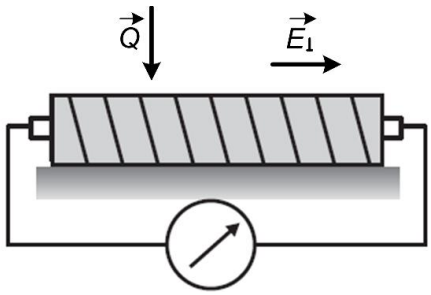

Figure 1.7: Gradient heat flux sensor (Mityakov et al., 2012)

The GHFS has a relatively simple structure compared with the aforementioned HFSs. The operating principle is based on the direct measurement of the heat flux. In this context, the heat flux is generated based on the temperature gradient across the layer; however, the temperature evaluation step is eliminated.

The application of the GHFS for the thermal analysis of the IGBT module is discussed in this dissertation. A test setup with an IGBT mounted on an air-cooled heat sink is considered, and the heat flux measurement results are compared with the thermal

modelling performed by the Finite Element Method (FEM) and the expected power losses, modelled in the PLECS simulation circuit.

1.2.6 **Condition monitoring of power electronics**

Implementation of the condition monitoring (CM) scheme provides an opportunity to detect device deterioration and prevent a device failure. However, selection of a proper signature, which is closely related to the device degradation, is the main issue of condition monitoring systems implemented so far (Yang et al., 2010).

The thermal behaviour of the device reflects its ability of heat transfer and its state of deterioration. Thus, measurement of junction temperature would offer an excellent tool for condition monitoring. However, owing to the high density of the modern semiconductor devices, it is difficult to implement a temperature sensor inside a module. Therefore, it is reasonable to measure the device external parameters, which does not require physical contact with the internal structure of the module. Condition monitoring can be implemented by temperature sensitive electrical parameters (TSEPs), such as the IGBT collector-emitter saturation voltage $U_{\mathrm{ce,sat}}$, the gate-emitter voltage U_{ge}, and the collector-emitter resistance R_{ce} (Avenas et al., 2012). In this approach, the initial calibration is carried out to define the dependence of the electrical parameters on the junction temperature. It requires an external heating of the device and a low input current to avoid the device self-heating.

The IGBT collector-emitter saturation voltage $U_{\mathrm{ce,sat}}$ is used to detect the bond wire lift-off. Depending on the IGBT rated current, even a slight increase in $U_{\mathrm{ce,sat}}$ can indicate degradation in wire bonding. In (Held et al., 1997), the failure criterion of a 300 A IGBT module is a 5 % increase in $\mathrm{U_{ce,sat}}$.

In (Coquery et al., 1999), the use of the thermal resistance R_{th} to detect solder cracking has been proposed. However, in order to define R_{th}, the device on-state parameters, such as operating current and voltage, case temperature, and estimated junction temperature, are required. The failure criterion has been found to be a 20 % increase in the thermal resistance (Coquery & Lallemand, 2000).

The main issue of the aforementioned condition monitoring methods is the indirect measurement of the thermal stress. The junction-temperature-related signatures are more or less related to the thermal stress. In this research, a direct heat flux measurement of the IGBT module using a GHFS is proposed as the method for condition monitoring. A condition monitoring system based on the online IGBT heat flux detection in a WT power converter is introduced. However, the non-uniform heat flux distribution over the base plate should be taken into account. In order to apply heat flux measurements as the condition monitoring method and an indicator of device degradation, online estimation of the actual power losses is needed to compare the measured results with the reference value.

1.3 Objectives and scope of the work

The aim of this doctoral dissertation is to perform a thermal load analysis and estimate the lifetime of IGBT modules taking into account site-specific variables, such as average wind speed, turbulence intensity, and wind speed distribution (i.e., the number of occurrences of wind speed within a specific interval). A reliability model of the IGBT is developed with respect to the power performance of the DFIG wind turbine model with the wind speed profile in the input. The dominant failure mechanisms of the IGBT, bond wire lift-off and solder fatigue, are included in the lifetime prediction method. The core of the doctoral dissertation consists of the following themes:

- Investigation of the WT power profile in site-specific low wind conditions in the south-eastern region of Finland;
- The DFIG operating modes and the corresponding converter loading;
- Distribution of the power device thermal stress over the wind speed range and indication of the most stressing thermal zone according to the local wind speed conditions;
- Lifetime estimation of the power devices with respect to the site-specific wind speed distribution;
- A possible solution for the condition monitoring (CM) using a gradient heat flux sensor (GHFS).

1.4 Outline of the doctoral dissertation

This doctoral dissertation comprises the following chapters:

Chapter 1 provides the background, motivation, and objectives of the doctoral dissertation, and introduces the most commonly adopted WT technology, the DFIG. Reliability issues of the wind power converter are elaborated on. The relevance of the power semiconductor reliability problem in DF drives is demonstrated.

Chapter 2 focuses on the important features of low wind speed conditions. The aerodynamic and mechanical performances of a wind turbine are delineated. Four operational modes of the DFIG are distinguished. The rotational speed and the blade pitch angle control systems are addressed.

Chapter 3 defines the basic concepts of the DFIG operation. The operating regimes of the WT are described. The generator electrical parameter and the slip frequency behaviour depending on the wind speed are studied. The thermal load of the converter is analysed.

Chapter 4 introduces an IGBT module lifetime estimation method. Power semiconductor thermal cycles are considered with respect to the DFIG dynamic performance in low wind

speed conditions. Wear-out failure mechanisms of the power device are included in the lifetime model description.

Chapter 5 identifies opportunities to use the GHFS to measure the dissipated IGBT power loss. The heat flux sensor technology is investigated. The test setup for the IGBT heat flux measurement is presented, and the results are compared with the finite-element method (FEM) model. The CM system to observe the IGBT thermal loading by using the heat flux sensor is proposed.

1.5 Scientific contribution and publications

The main contributions of the doctoral dissertation are:

1. Analysis of the IGBT module thermal stress in DFIG wind power converters on low wind speed sites.
2. IGBT module lifetime estimation taking into consideration the low wind speed profile and the physics of failure.
3. Analysis of the GHFS in the wind power application.

The results related to the research topic of this doctoral dissertation are published in the following papers:

1. Hynynen, K., Baygildina, E., and Pyrhönen, O. (2012). ”Wind Resource Assessment in Southeast Finland.” In *IEEE Power Electronics and Machines in Wind Applications (PEMWA)*, Denver, CO, USA.
2. Baygildina, E., Peltoniemi, P., Pyrhönen, O., Ma, K., and Blaabjerg, F. (2013). ”Thermal loading of wind power converter considering dynamics of wind speed.” In *IEEE Industrial Electron Society (IECON)*, Vienna, Austria.
3. Baygildina, E., Hynynen, K., Koivuniemi, A., and Pyrhönen, O. (2014). ”Inland Wind Resource Assessment in Southeast Finland.” *Wind Engineering*, vol. 38, issue 2, pp. 9–18.
4. Baygildina, E., Smirnova, L., Peltoniemi, P., Ma, K., and Pyrhönen, O. (2014). ”Power semiconductor lifetime estimation considering dynamics of wind turbine.” In *IEEE Symposium on Power Electronics & Machines for Wind and Water Applications (PEMWA)*, Milwaukee, WI, USA.
5. Baygildina, E., Smirnova, L., Murashko, K., Juntunen, R., Mityakov, A., Kuisma, M., Pyrhönen, O., Peltoniemi, P., Hynynen, K., Mityakov, V., Sapozhnikov, S. (2016). ”Application of a heat flux sensor in wind power electronics.” *Energies*, vol. 9, issue 6.
6. Baygildina, E., Smirnova, L., Murashko, K., Juntunen, R., Mityakov, A., Kuisma, M., Pyrhönen, O., Peltoniemi, P., Hynynen, K., Mityakov, V.,

Sapozhnikov, S. (2016). ”Condition Monitoring of Wind Power Converters Using Heat Flux Sensor”. *IREE*, vol. 11, issue 3, pp. 239–246.

2 Wind energy conversion

In this chapter, a brief introduction into the nature of wind as a complex airflow phenomenon is given. Wind statistics tools, such as wind speed distribution and turbulence intensity, are applied to describe the wind speed dynamics. The WT aerodynamic and mechanical performance as a function of wind speed, the turbine parameters, and the control system are presented.

2.1 Characteristics of wind

2.1.1 Atmospheric forces

Wind is an airflow, which is highly variable in space and time. Four forces cause the spatial large-scale airflow: the pressure difference, the Coriolis force, the frictional force, and the centrifugal (or inertial) force (Fovell, 2010). The sun unevenly heats the earth's surface and the atmosphere. It causes the atmospheric circulation from the most heated equator to the poles, which absorb less solar radiation. The uneven heating produces pressure differences across the surface, which push the air from a high to a low pressure. The pressure gradient force (pressure difference divided by distance) defines the speed of the moving air mass. The air moves predominantly in the horizontal direction, since the gravitation force eliminates the vertical airflow.

The Coriolis force, caused by the earth's rotation, deflects the wind vector to the right in the northern hemisphere and to the left in the southern hemisphere. The magnitude of the Coriolis force depends on the wind speed and the latitude. When the pressure force and the Coriolis force are both active and in opposition, the resultant wind is driven by these forces along the isobars, and it is called 'geostrophic wind' (Manwell et al., 2009).

The friction force decelerates the airflow close to the earth's surface. The friction force always acts to retard the air flow and drives the wind to the low-pressure area (Figure 2.1). The effect of the force weakens at higher heights; however, the friction force acts only within the earth's boundary layer. Thus, above the boundary layer the wind is blowing along the isobars.

If the isobars are curved and the air moves in circular paths, the centrifugal (inertial) force acts on the airflow. An inertial force is always directed outward from the centre of the spin. As presented in Figure 2.2, the pressure gradient force acts towards the centre of the isobar circles, the Coriolis force is directed to the right of the wind vector, and the centrifugal force is directed outward from the centre.

Because of the earth's terrain features, the large-scale air circulation is distributed into small-scale patterns, which define site-specific climatic features. Mountains and hills create vertical paths for air masses, forcing cold air to sink and warm air to rise. Moreover, owing to higher altitudes of local regions, the wind speed is generally high. Coastal

regions also experience local wind speed variations. Sea and land breezes develop because the land surface heats up more rapidly than the sea (Burton et al., 2001).

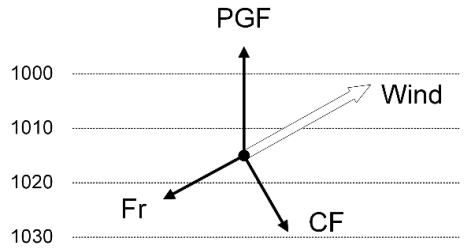

Figure 2.1: Atmospheric forces in the case of straight isobars: pressure gradient force (PGF), friction force (Fr), and Coriolis force (CF).

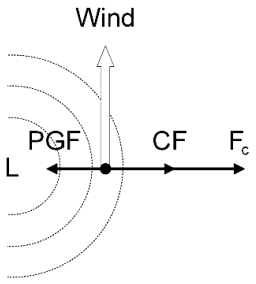

Figure 2.2: Atmospheric forces in the case of curved isobars: pressure gradient force (PGF), Coriolis force (CF), and centrifugal force (F_c).

The temporal wind variations in a specific location can be classified into long-term (inter-annual), medium-term (from hours to one year), and short-term ones (from minutes to seconds) (Figure 2.3) (Manwell et al., 2009).

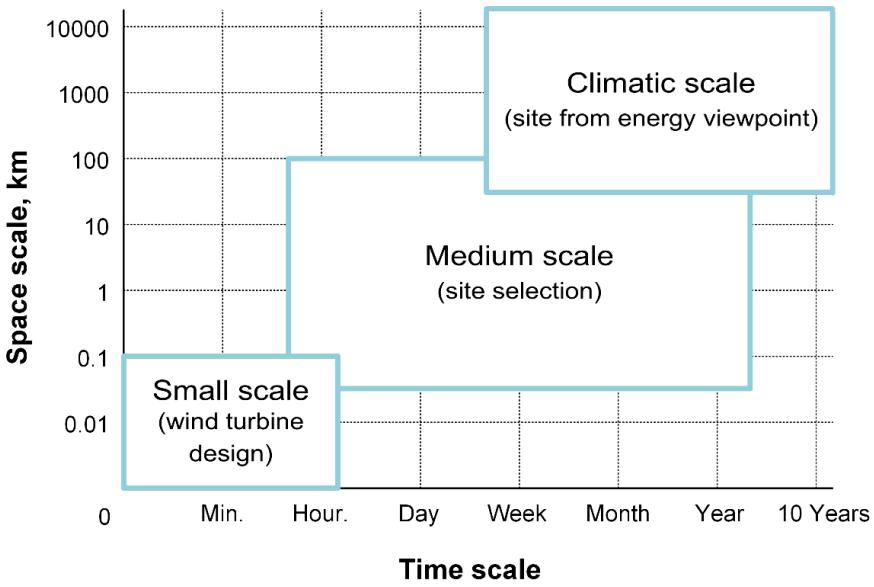

Figure 2.3: Temporal and spatial wind variations (Manwell et al., 2009).

Estimation of the long-term wind variations is a difficult task, because it is hard to predict the constantly changing global climate. Wind data for 30 years are needed in order to define long-term energy production tendencies and perform a reliable prediction (Manwell et al., 2009). Medium-term wind variations are more predictable than long-term variations. They reflect seasonal climatic changes and are used to perform site assessment for wind farm projects.

The small-scale wind dynamics assumes short-term turbulent wind variations. The short-term wind fluctuations must be considered at the WT design stage to estimate the potential structural fatigue and select the control system strategy. Moreover, turbulent wind data are applied to analyse the WT power performance and energy conversion efficiency (Belu & Koracin, 2012).

2.1.2 **Wind speed distribution**

The medium-term variations can be characterized by a probability distribution function. The Weibull distribution usually fits the wind condition on many sites (Burton et al., 2001). The distribution is given by

$$p(v) = \frac{k}{c}\left(\frac{v}{c}\right)^{k-1} \exp\left(-\left(\frac{v}{c}\right)^{k}\right), \tag{2.1}$$

where *p(v)* is the probability density function (PDF) of the wind speed *v*, c is a scale parameter, and *k* is a shape parameter. Both the shape and scale parameters are functions of mean wind speed and standard deviation.

The Rayleigh distribution is a special case of the Weibull distribution with the shape parameter equalling two (Manwell et al., 2009). It is the simplest distribution function, which uses only the mean wind speed value. The Rayleigh probability function can be given by

$$p(v) = \frac{\pi}{2}\left(\frac{v}{\bar{v}^2}\right) \exp\left(-\frac{\pi}{4}\left(\frac{v}{\bar{v}}\right)^{2}\right), \tag{2.2}$$

where $\bar{v}$ is the mean wind speed.

In Figure 2.4, the wind speed distribution in the south-eastern region of Finland is shown. The measurements were performed by a Light Detection And Ranging (LIDAR) sensor at the height of 91 m from 1 June 2014 to 1 June 2015. The Weibull and Rayleigh PDFs are calculated. Obviously, the Rayleigh function does not represent the data accurately. The Weibull function perfectly fits the histogram with the scale parameter 6.70 and the shape parameter 2.77. The average wind speed in the region is 6 m/s.

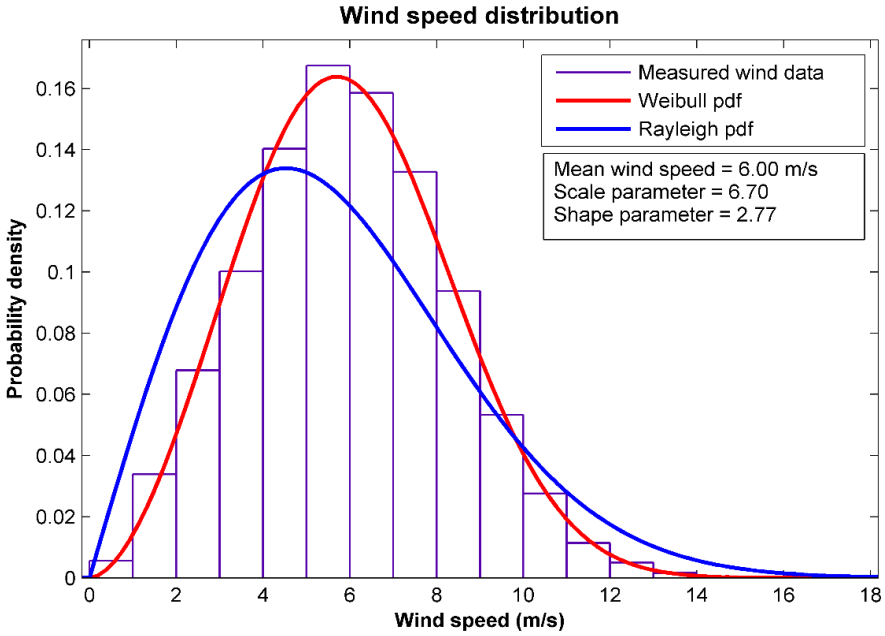

Figure 2.4: Wind speed distribution in the south-eastern region of Finland and the Weibull and Rayleigh probability distribution functions.

Wind speed distribution is usually applied to estimate the annual energy production (AEP) of the WT, which is an important issue in the economic feasibility analysis of the WT.

2.1.3 **Turbulent wind**

Turbulence is the wind speed fluctuation over short periods of time, usually less than a minute. For time periods of an hour or more, there is a turbulent component of wind around a constant mean value. The turbulence phenomenon can be explained by terrain features and a thermal effect. In mountain and hill areas, an increase in altitude causes a decrease in temperature and pressure, resulting in upward and downward air motions and making the wind flow less stable (Fovell, 2010).

The turbulent wind flows in longitudinal, lateral, and vertical directions. However, the longitudinal direction is prevailing (Manwell et al., 2009). The chaotic motion of the turbulent air is challenging to formulate by equations. In order to synthesize an actual site-specific turbulent wind, the impacts of temperature, pressure, humidity, and air density, as well as topographic features have to be considered. To this end, a statistical approach is applied in terms of turbulence intensity (TI) (Burton et al., 2001), which can be defined as

$$TI = \frac{\sigma}{\bar{v}}, \tag{2.3}$$

where $\bar{v}$ is the mean wind speed over a 10 min or 1 h period and σ is the standard deviation of the wind speed around the mean value. The standard deviation is given by

$$\sigma = \sqrt{\frac{1}{N-1}\sum_{i=1}^{N}(v_i - \bar{v})^2}, \tag{2.4}$$

where N is the number of elements in the sample, and v_i is the i-element of the wind speed row data.

Usually, TI varies within the range from 0.1 to 0.4 (Manwell et al., 2009). In complex terrain conditions, such as cities and forests, where the friction effect is significant, TI is higher than over a flat area, such as sea and desert. Furthermore, high turbulence occurs generally at low wind speeds. In Figure 2.5, TI as a function of wind speed is presented. The measurements are used in the form of 10-min averages of the wind speed and the standard deviation. The measurements were carried out in South-Eastern Finland, where the surface features and the highly forested area can be regarded as a complex terrain.

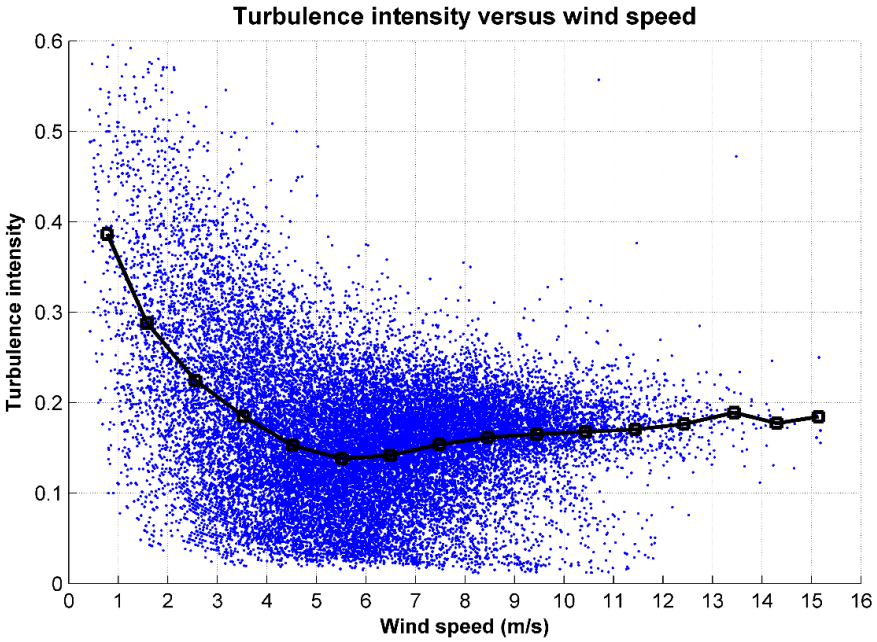

Figure 2.5: Turbulence intensity versus wind speed based on wind speed measurements in the south-eastern region of Finland from 1 June 2014 to 1 June 2015.

According to (Burton et al., 2001), the various standards for TI, such as the IEC, Danish standards (DS 472), and Germanisher Lloyd (GL), are specified.

The impact of the turbulent wind on the WT is important for the control system solution and the stress analysis of mechanical structures. In addition, the turbulent wind speed dynamics has an impact on the thermal loading of the power electronics. Thus, simulation of the turbulence dynamics is an inherent part of the WT design process.

2.2 Wind turbine power performance

2.2.1 Wind turbine subsystems

The horizontal-axis variable-speed wind turbine performance can be characterized by the operation of the main subsystems shown in Figure 2.6. The subsystems are determined as follows:

- **Wind turbine aerodynamic subsystem** represents the kinetic energy conversion of wind into mechanical energy.
- **Mechanical subsystem** describes power transmission in the inertial mass mechanical model following Newton's second law for the rotational motion.
- **Electrical subsystem:** the electrical drive, comprising the electrical machine and the converter. This unit transforms the generator torque and the rotor rotations into electrical energy.
- **Control system** regulates the blade pitch angle, the yaw angle, the WT rotational speed, the generator torque, and the active and reactive power. The control system of the grid operator is not included in the scheme.

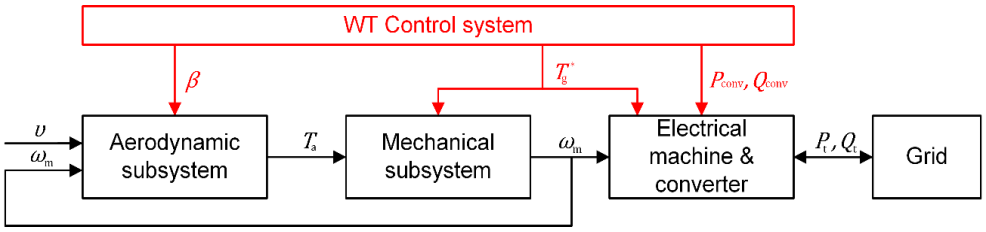

Figure 2.6: Wind turbine subsystems.

In the present chapter, the aerodynamic and mechanical subsystems, the rotational speed, and the blade pitch angle control systems are described. The aerodynamic and mechanical parameters applied here are related to the WT considered as a case study in Chapter 3.

The electrical subsystem and the WT generator control system are also addressed in Chapter 3.

2.2.2 **Aerodynamic performance**

The WT aerodynamic performance indicates how the WT rotor captures the kinetic energy of the wind. The efficiency of the wind capturing mainly depends on the WT blade geometry. Thus, a part of the wind power is converted into mechanical power of the rotating shaft. Usually, in order to study the wind interaction with the WT, the rotor is presented as an actuator disk with an area A_r (Manwell et al., 2009). The wind power P_v over the area A_r can be given by

$$P_\mathrm{v} = \frac{1}{2}\rho A_\mathrm{r}\, v^3, \tag{2.12}$$

where ρ is the air density and v is the wind speed.

The mechanical power of the WT is

$$P_\mathrm{m} = \frac{1}{2}\rho A_\mathrm{r} C_\mathrm{p}(\lambda,\beta)\, v^3, \tag{2.13}$$

where $C_\mathrm{p}(\lambda,\beta)$ is the power coefficient, λ is the tip speed ratio, and β is the blade pitch angle. The maximum theoretical value of the power coefficient is 0.59 (Betz limit). In practice, the maximum claimed wind energy conversion efficiency $C_{\mathrm{p\_max}}(\lambda,\beta)$ is 0.52 (Meshram, 2013).

The tip speed ratio is the ratio of the linear speed of the rotor and the wind speed

$$\lambda = \frac{\omega_\mathrm{m} r}{v}, \tag{2.14}$$

where ω_m is the rotational speed of the turbine and r is the rotor radius.

Below the rated wind power, the WT control system regulates the rotor rotational speed in order to obtain the optimal tip speed ratio λ_opt, while the blade pitch angle β is kept at the minimum value. In Figure 2.7, the power coefficient C_p as a function of tip speed ratio and blade pitch angle is presented. Here, the applied C_p function is given by the following equation (Heier, 2014)

$$C_\mathrm{p}(\lambda,\beta) = k_1\left(\frac{k_2}{\lambda_i} - k_3\,\beta - k_4\right)e^{-\frac{k_5}{\lambda_i}} + k_6\lambda, \tag{2.15}$$

where

$$\frac{1}{\lambda_i} = \frac{1}{\lambda + 0.08\beta} - \frac{0.035}{\beta^3 + 1}. \tag{2.16}$$

The maximum of the power coefficient is 0.48 reached at λ = 8.1 and at a blade pitch angle β = 0°.

The coefficients k_i in Equation 2.15 are k_1 = 0.5176, k_2 = 116, k_3 = 0.4, k_4 = 5, k_5 = 21, and k_6 = 0.0068 (Heier, 2014).

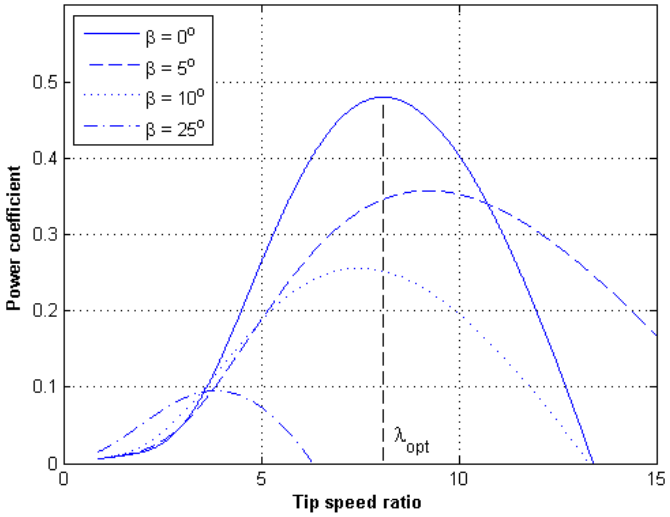

Figure 2.7: Power coefficient of the wind speed as a function of tip speed ratio and blade pitch angle.

2.2.3 **Mechanical subsystem**

The WT operation represents an interaction of the numerous mechanical components. However, the underlying concept of the WT dynamics can be defined by the operation of the inertial mass driven by the torque and following Newton's second law in the form

$$T_{\mathrm{a}} - T_{\mathrm{g}} = J_{\mathrm{t}}\dot{\omega}_{\mathrm{m}}, \tag{2.17}$$

where T_{a} is the aerodynamic torque, T_{g} is the generator torque, and J_{t} is the moment of total turbine inertia. For a precise description of the drive train dynamics, the WT can be represented as a two-mass mechanical model, where the turbine inertia is split into masses

on the low- and high-speed shaft sides. A two-mass mechanical model may concern the flexible shaft and friction of the rotating mass (Abad et al., 2011). However, in the present research, in order to introduce the WT dynamics from the viewpoint of the wind energy conversion efficiency, that is, the ability of the turbine to follow the turbulent wind, the mechanical subsystem is considered as a one-mass model. Thus, the turbine moment of inertia J_{t} in Equation (2.17) represents the blades, the hub, the rotating shaft, the gearbox, and the electrical machine taken together as one mass.

In order to represent graphically the relationship between the generator and aerodynamic torques, the latter is introduced as a function of wind speed and rotational speed (Manwell et al., 2009).

$$T_{\mathrm{a}} = \frac{1}{2\omega_{\mathrm{m}}}\rho A_{\mathrm{r}} C_{\mathrm{p}}(\lambda, \beta) v^3. \tag{2.18}$$

Following the optimal operating point of the WT means keeping the balance of the torques in Equation (2.17). Figure 2.8 illustrates the WT optimal power curve and the characteristics of the generator torque and the aerodynamic torque as functions of rotational speed and wind speed. The point of the maximum power production is placed on the downward slope of the aerodynamic torque at the intersection of the generator load torque.

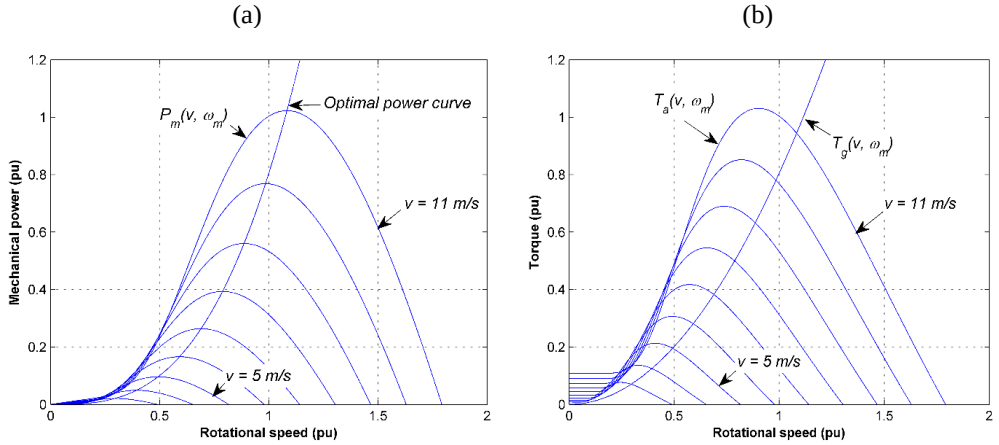

Figure 2.8: Wind turbine load characteristics. (a) Mechanical power. (b) Torque.

The power curves have unsymmetrical slopes on the left and right sides of the optimal power curve. One can see that the operating point does not follow the maximum aerodynamic torque, and thus, the generator electromagnetic torque curve is shifted to the right. Considering an operating point on the negative slope of the aerodynamic torque

curve for a specific wind speed, the positive or negative error in rotational speed would produce a smaller absolute error in the power than on the positive slope.

2.2.4 **Wind turbine speed and pitch angle control**

The operation of the WT is based on four operating modes. In modes 1 and 3 (Figure 2.9), the generator rotational speed is limited and kept constant at ω_{g_min} and ω_{g_max} by the limited generator slip range. The tip speed ratio λ is maintained above and below the optimal value in regions 1 and 3, respectively. The power coefficient C_p is always below the maximum value. In (Abad et al., 2011) and (Munteanu et al., 2008), it is mentioned that the constant rotational speed can be maintained by the blade pitch angle control. However, in the present research, the control strategy for these modes is implemented by the electromagnetic torque control. The basic concept of both methods is to follow the desired tip speed ratio and the power coefficient.

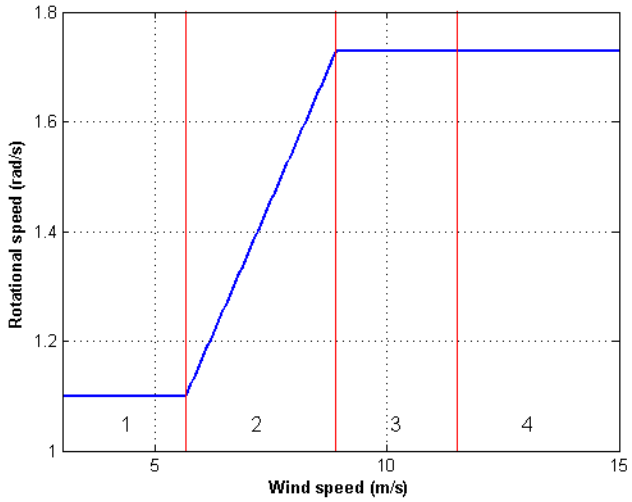

Figure 2.9: Four operating modes of a doubly-fed induction generator-based wind turbine.

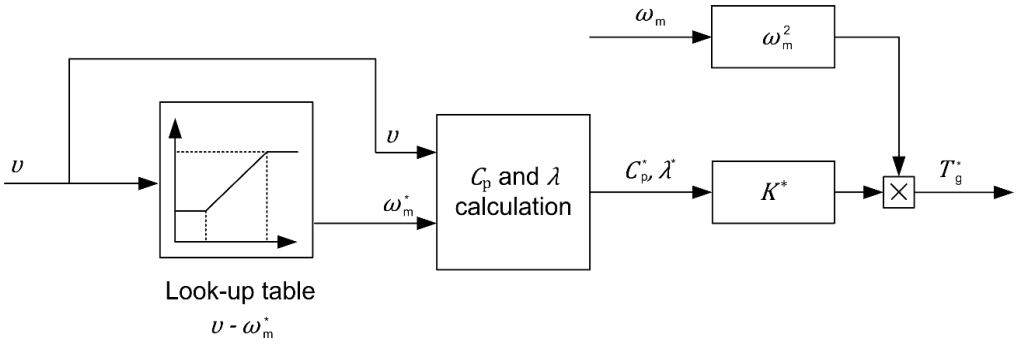

Figure 2.10: Block diagram of the reference generator torque calculation in modes 1–3.

In Figure 2.10, the reference generator torque T_g^* is calculated by estimation of the parameter K^* based on the desired power coefficient C_p^* and the tip speed ratio λ^*

$$\lambda^* = \frac{\omega_m^* R}{v}, \tag{2.19}$$

$$C_p(\lambda^*) = c_1 \left(\frac{c_2}{\lambda^*} - 0.035c_2 - c_3\right) e^{c_4\left(0.035 - \frac{1}{\lambda^*}\right)} + c_5\lambda^*, \tag{2.20}$$

where c_1 = 0.5176, c_2 = 116, c_3 = 5, c_4 = 21, and c_5 = 0.0068. The reference rotational speed ω_m^* is obtained based on a look-up table, where the wind speed is used as an input signal (Heier, 2014).

Equations (2.19) and (2.20) are used to define λ^* and C_p^* , respectively. Equation (2.20) is derived based on Equation (2.15), assuming the blade pitch angle β = 0°.

The estimated generator torque in modes 1–3 follows the proportionality with the square of rotational speed, as shown in Figure 2.10. This strategy is commonly used, especially in medium- and large-scale WTs (Munteanu et al., 2008)

$$T_g^* = \frac{1}{2\lambda^{*3}} \rho\pi C_p^* r^5 \omega_m^2 = K^* \omega_m^2. \tag{2.21}$$

In region 2, the power coefficient C_p^* and the tip speed ratio λ^* are kept at optimal values C_{p_max} and λ_{opt}, respectively. Thus, the generator electromagnetic torque follows the optimal curve, as indicated by mode 2 in Figure 2.11

$$T^*_{\mathrm{g\_opt}} = \frac{1}{2\lambda^3_{\mathrm{opt}}}\rho\pi C_{\mathrm{p\_max}} r^5 \omega^2_{\mathrm{m}} = K_{\mathrm{opt}}\omega^2_{\mathrm{m}}. \quad (2.22)$$

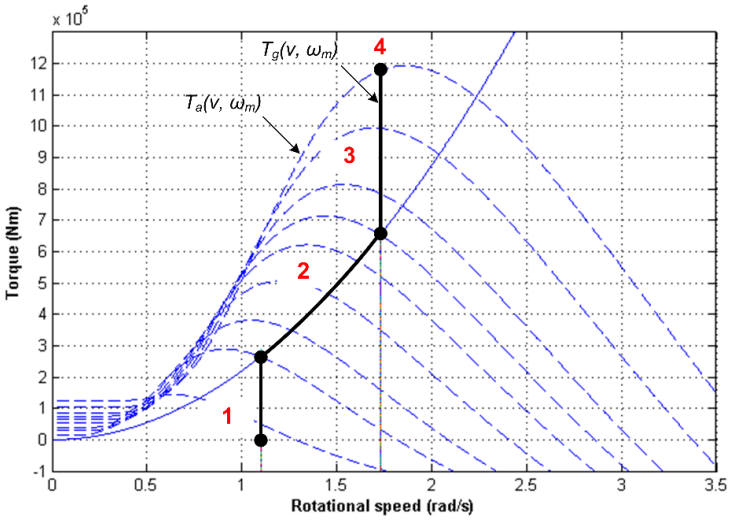

Figure 2.11: Generator torque behaviour in a doubly-fed induction generator-based wind turbine.

In Figure 2.12, the operating modes of the generator torque and mechanical power versus wind speed are shown.

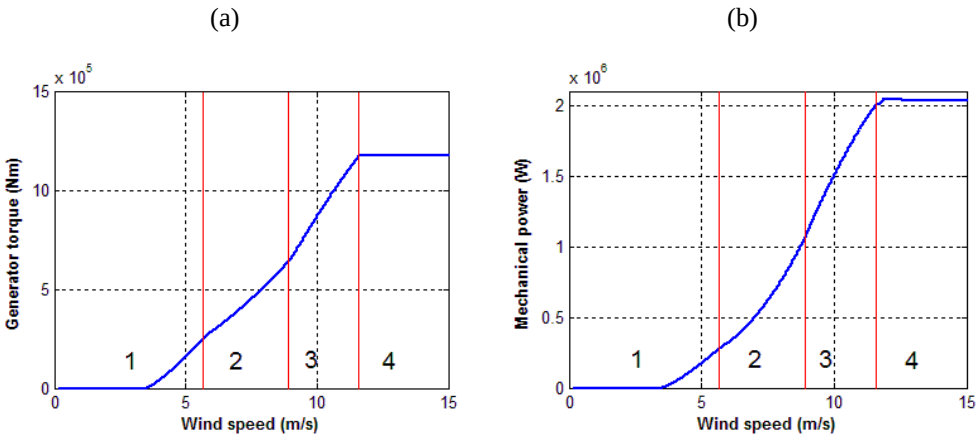

Figure 2.12: Wind turbine operating modes. (a) Generator torque and (b) mechanical power versus wind speed.

In mode 4, the blade pitch angle control is applied to limit the mechanical power at wind speeds above the nominal value (Figure 2.13). The proportional–integral–derivative

(PID) controller is used to generate the reference pitch angle β^* (Poore & Lettenmaier, 2003). The anti-windup component cancels the integral component of the PID controller if the pitch limit is reached. The limitation of the pitch angle rate is applied to perform the dynamics of the actuator.

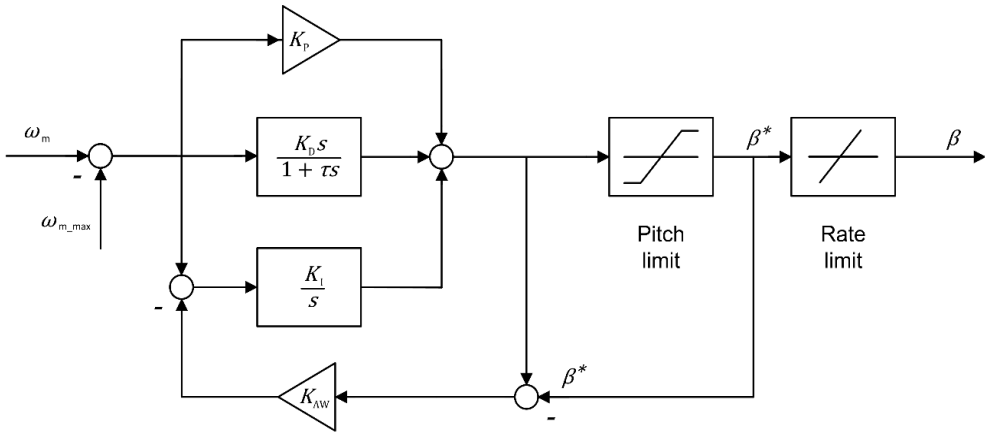

Figure 2.13: Blade pitch control block diagram (Poore & Lettenmaier, 2003).

2.3 Summary

The nature of the wind and atmospheric forces acting on the local characteristics of the air flow were discussed in Chapter 2. The forces are the pressure difference, the Coriolis force, the frictional force, and the centrifugal force. The Rayleigh and Weibull probability density functions, which describe the local wind speed distribution, were presented. The origins of the turbulence and its characteristics were delineated. It was shown that the Weibull distribution with the scale and shape parameters $k = 2.77$ and $c = 6.7$ fits well the measured data collected in the south-eastern region of Finland from 1 June 2014 to 1 June 2015. The averaged wind speed was 6 m/s. The TI varied from 0.1 to 0.4. The general tendency of the TI curve shows that at low wind speeds the TI is higher, and it decreases as the wind speed increases. However, the TI minimum is found at the average wind speed.

The WT aerodynamic, mechanical performance in terms of the wind power conversion efficiency and the aerodynamic and mechanical torque behaviour were described. Four operation modes were presented. The corresponding rotational speed and blade pitch control systems were considered.

3 Modelling of the DFIG and analysis of the thermal loading of the power converter

Before considering the model of the DFIG-based WT and the thermal performance of the power converter, the main components of the system are described in brief in the introductory part of this chapter. In Section 3.2, a definition of the generator slip and concepts of the bidirectional power flow in the frequency converter are introduced in order to comprehend the specific features of the IGBT thermal loading in different operating modes.

This chapter addresses steady-state electrical equivalent circuits of the DFIG, and thus, the transient dynamics is not examined. The operation of the DFIG is analysed in several steady states, that is, a set of steady wind speeds are introduced as an input. In Sections 3.3–3.5, the model of the DC link, the LCL filter, and the control system are described to establish consistency and entirety of the model.

The basic principles of the power loss calculation performed by the PLECS software and the IGBT thermal model are outlined in Section 3.6. Calculation of the power losses in several steady states is an inherent part of the lifetime estimation model. The DFIG electrical parameters, such as operating voltage, load current, slip, and modulation index, have an essential impact on the thermal stress and an effect on the characteristics of the power loss distribution over the wind speed range.

The PLECS model of the 2 MW WT is presented as a case study in Section 3.7. The IGBT junction temperature behaviour in terms of mean values and changes is presented. Further, in Chapter 4, the junction temperature fluctuations are used to count the number of cycles to failure and estimate the IGBT lifetime.

3.1 Introduction

As mentioned in Chapter 1, **the stator** of the DFIG is directly connected to the grid (Figure 3.1). The voltage of the stator, which is applied from the grid, is constant with a constant frequency. Typically, in 36–48 slot, three-phase stator windings there are 2–4 pole pairs (Abad et al., 2011).

The wound rotor of the DFIG is connected to the BTB two-level converter through slip rings. The rotor also has a three-phase winding with the same number of pole pairs as the stator.

The DFIG turbine transformer has two secondary low-voltage windings, one for the stator and one for the rotor, which typically have different voltage ratings. The primary winding connects the turbine to the wind farm medium-voltage grid (Figure 3.1).

The gearbox usually has a large gear ratio in the range of 1:100. The most common gearbox configuration has a combination of two-stage planetary and one-stage helical gears (Ragheb & Ragheb, 2011).

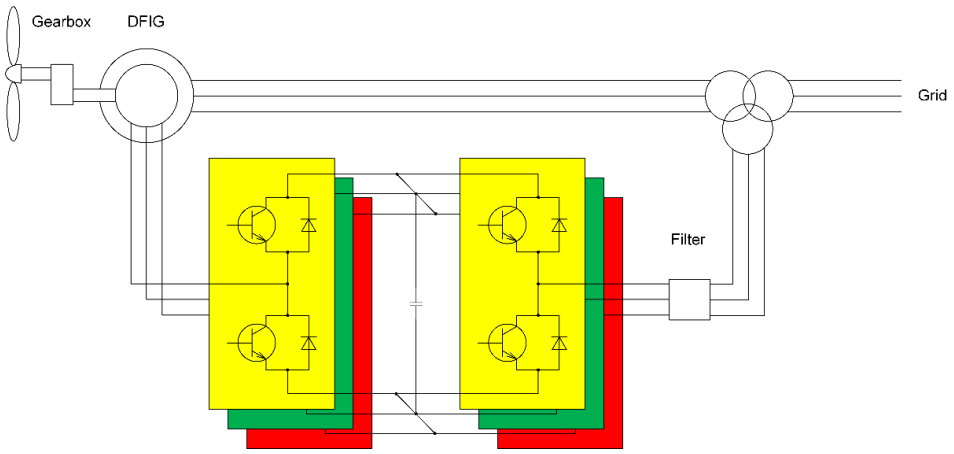

Figure 3.1: General configuration of the wind turbine based on a double-fed induction generator.

The BTB two-level power converter is a conventional solution for the DFIG and the prevalent choice for 1.5–3 MW wind turbines (Abad et al., 2011). The rotor-side converter (RSC) delivers excitation current for the rotor with the slip frequency. Depending on the rotor rotational speed, the slip frequency is controlled to maintain a constant frequency of the magnetic field in the air gap. The RSC also controls the power factor of the stator terminals and provides the reactive power exchange between the generator and the grid, while the grid-side converter (GSC) remains reactive neutral. Optionally, the reactive power control can ensure the desired level of voltage at the grid terminals in the case of grid faults. In this case, the rotor- and grid-side control systems require a cooperative operation (Akhmatov, 2003).

The operating range of the slip frequency is typically ±30 % of the synchronous frequency (Blaabjerg et al., 2011). The sign of the slip frequency defines the machine sub-synchronous or super-synchronous operating modes. In the sub-synchronous mode, the RSC operates as an inverter, and at the super-synchronous mode as a rectifier. Therefore, the bidirectional operation of the BTB allows the rotor to receive power from the grid or deliver power to the grid.

For multi-MW WTs, in order to handle high converter currents and avoid high switching losses, a multi-cell topology with several paralleled BTB power converters can be used. Wind turbine manufacturers, such as Gamesa and Siemens, have introduced this topology in large-scale WTs (Andresen & Birk, 2007), (Jones & Waite, 2011).

The DC link between the RSC and the GSC serves to maintain a constant DC link voltage. Because of high voltage surges coming from the generator and transformer windings, the LCL filters are used between the grid and the GSC (Ma, 2013).

Utility-scale WT power converters for the DFIG are usually designed for a low-voltage level of 690 V, and a power range from 500 to 6000 kW. Typical technical characteristics of low-voltage converters are presented in Table 3.1 (Abad et al., 2011).

Table 3.1 Typical characteristics of a utility-scale BTB wind power converter (Abad et al., 2011).

Characteristics	**Data for BTB power converter**
Nominal power	500-6000 kW
Nominal voltage	690 V
Nominal frequency	50/60 Hz
Switching frequency	2.5–5 kHz
Efficiency at rated point	≥97 %
DC bus voltage	1000 V
Total harmonic distortion	<5 %
Semiconductor type	IGBT
Control type	Field-oriented/DTC
Cooling	Air/liquid cooled

An example of ABB and Ingeteam low-voltage converters for 0.5–6 MW range DFIG-based WTs are shown in Figure 3.2 (ABB, 2016), (Ingeteam, 2016).

(a) (b)

Figure 3.2: Low-voltage BTB converter for DFIG-based wind turbines. (a) ABB ACS800. (b) DFM Ingecon.

The most important component of the converter circuit is the power semiconductor. The preferable choice for the low- and medium-voltage class converters is the insulated gate bipolar transistor (IGBT). A freewheeling diode connected in parallel with the transistor provides bidirectional current flow, and thus, the converter operates both in the inverting and rectifying modes. The transistor and the freewheeling diode are enclosed in one module. The IGBT module is manufactured as several parallel-connected chips connected by bond wires. In the medium voltage converters, the IGBT press-pack packaging technology is more suitable for large-scale WTs. Advantages of the press-pack over the module technology are the increased power density and the improved reliability resulting from the elimination of the bond wires. However, the IGBT module is preferable because of its low cost and easier mounting (Abu-Rub et al., 2014).

The IGBT modules are selected according to the application with the properly selected maximum collector-emitter voltage and the DC collector current. The maximum allowed voltage cannot be exceeded, and because of the switching overvoltage, the demand is more difficult with the parasitic inductances. In this case, the clamp circuitry is used to limit the switching overvoltages. For the 690 V AC line-to-line terminal voltage of the power converter, the 1.7 kV module is the most suitable one (Bywaters et al., 2004). The rated collector current should be selected in order to keep the junction temperature below the maximum.

3.2 DFIM operating modes

The doubly-fed induction machine (DFIM) is a wound-rotor induction machine supplied with an alternating current on both the stator and rotor sides. The underlying principle of

the DFIM operation is based on an interaction between the angular frequency of the rotor ω_r and the angular frequency of the stator magnetic field ω_s. The frequency of the stator magnetic field remains constant as the stator windings are connected to the grid with the frequency f_s. The angular frequency of the rotor ω_r varies with the wind speed. Thus, in order to maintain a constant stator frequency, the rotor is supplied with currents and voltages of variable frequency. The relation of the angular frequencies of the rotor and the stator is given as (Fletcher, 2010)

$$\omega_{\mathrm{s}} = \omega_{\mathrm{r}} + \omega_{\mathrm{slip}}. \tag{3.1}$$

The angular frequency of the rotor is the mechanical speed of the WT on the low-speed side of the shaft ω_m multiplied by the gear ratio N_{gear} and the number of pole pairs n_p,

$$\omega_{\mathrm{r}} = N_{\mathrm{gear}} \cdot n_{\mathrm{p}} \cdot \omega_{\mathrm{m}}. \tag{3.2}$$

The visual representation of Equation 3.1 is shown in Figure 3.3.

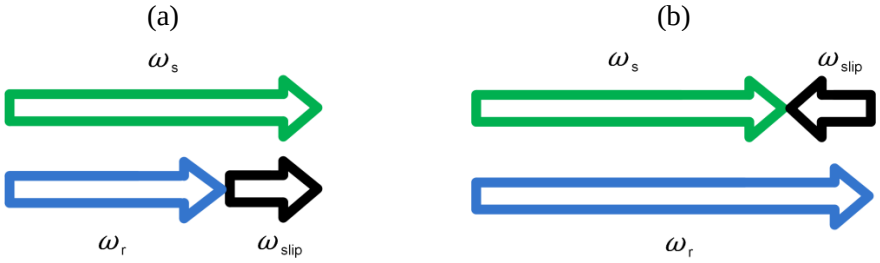

Figure 3.3: Visual representation of the interaction between the angular speeds of the stator and the rotor magnetic fields, ω_{s} and ω_{r}, respectively, and the mechanical speed of the generator ω_{m}. (a) Sub-synchronous mode. (b) Super-synchronous mode.

If the rotor angular frequency ω_{r} is below the synchronous frequency of the stator ω_{s}, the rotations of the rotor magnetic field and the rotor itself are in the same direction (Figure 3.3(a)), and thus, the resultant speed is equal to the stator synchronous speed ω_{s}. When the rotor angular frequency ω_{r} is above ω_{s}, the rotor magnetic field rotates in the opposite direction with the rotor (Figure 3.3(b)). The rotor currents are of zero frequency if the rotor angular frequency ω_{r} and the stator synchronous speed ω_{s} are equal. Hence, the polarity of the rotor currents defines the sub- and super-synchronous operating modes of the generator.

The slip of the DFIG is calculated based on the synchronous and rotor angular frequencies of the generator,

$$s = \frac{\omega_s - \omega_r}{\omega_s}. \tag{3.3}$$

Based on Equations (3.1) and (3.3), the angular frequency of rotor voltage and current, or the slip frequency ω_{slip} (Abad et al., 2011), can be expressed as

$$\omega_{slip} = s\omega_s. \tag{3.4}$$

The balance between the mechanical power P_m, the active power delivered to the rotor through the converter P_r, and the stator active power P_s is derived as

$$P_m = P_s + P_r . \tag{3.5}$$

In order to present the mechanical power P_m in terms of the generator slip, the WT steady-state operation at a fixed speed can be considered, and the balance between the mechanical and the generator electromagnetic torque is achieved

$$T_{mech} = T_{em} , \tag{3.6}$$

where T_{mech} is the mechanical torque on the high-speed side of the gearbox and T_{em} is the generator electromagnetic torque.

Taking into account the following equations for the mechanical and electromagnetic torques

$$P_m = T_{mech}\omega_r, \tag{3.7}$$

$$P_s = T_{em}\omega_s, \tag{3.8}$$

and according to Equations 3.4 and 3.5,

$$\begin{aligned} P_r &= P_m - P_s = T_{mech}\omega_r - T_{em}\omega_s = T_{mech}(\omega_r - \omega_s) = \\ &= -sT_{mech}\,\omega_s = -sP_s . \end{aligned} \tag{3.9}$$

Based on Equation 3.9, the rotor active power is

$$P_r = -sP_s . \tag{3.10}$$

Therefore, the mechanical power is

$$P_{\mathrm{m}} = P_{\mathrm{s}}(1 - s). \tag{3.11}$$

Thus, it is reasonable to assume that the negative rotor power indicates power delivered from the grid, and the positive rotor power represents power flow from the rotor to the grid.

Thus, we obtain the following rules:

$P_{\mathrm{r}} < 0$, if $s > 0$, $\omega_{\mathrm{r}} < \omega_{\mathrm{s}}$ sub-synchronous speed operation, the rotor absorbing power;

$P_{\mathrm{r}} > 0$, if $s < 0$, $\omega_{\mathrm{r}} > \omega_{\mathrm{s}}$ super-synchronous speed operation, the rotor generating power.

3.3 **DFIG equivalent circuit**

Before addressing the equivalent circuit of the DFIM, the following notes and assumptions are made:

- Despite the stator and rotor three-phase windings, the equivalent circuit represents one phase of the stator and rotor windings;
- The stator voltage, applied from the network, with a constant amplitude and frequency;
- The rotor is connected to a grid via a frequency converter;
- For simplification purposes, the higher harmonics and iron losses are neglected.

According to the concept described in Section 3.2, the stator and rotor circuits operate at different frequencies. Thus, for the modelling purposes, it is reasonable to derive the electrical parameters of the circuits operating at the same frequency. In addition, the stator and rotor turns ratio must be taken into account.

Let us consider the voltage equations in the stator reference frame rotating at a synchronous angular speed ω_{s}. Here, the superscript ‘s’ is used to denote the stator flux oriented reference frame.

$$U_{\mathrm{s}}^{\mathrm{s}} = R_{\mathrm{s}} I_{\mathrm{s}}^{\mathrm{s}} + \frac{d\Psi_{\mathrm{s}}^{\mathrm{s}}}{dt}, \tag{3.12}$$

$$U_{\mathrm{r}}^{\mathrm{s}} = R_{\mathrm{r}}^{\mathrm{s}} I_{\mathrm{r}}^{\mathrm{s}} + \frac{d\Psi_{\mathrm{r}}^{\mathrm{s}}}{dt} - j\omega_{\mathrm{r}} \Psi_{\mathrm{r}}^{s}, \tag{3.13}$$

where U_s^s is the stator voltage, R_s is the stator resistance, I_s^s is the stator current, Ψ_s^s is the stator flux linkage, U_r^s is the rotor voltage, R_r^s is the rotor resistance, I_r^s is the rotor current, Ψ_r^s is the rotor flux linkage, and ω_r is the rotor electrical angular speed.

The stator and rotor flux linkages are

$$\Psi_s^s = I_s^s L_{ls} + \Psi_m^s, \tag{3.14}$$

$$\Psi_r^s = I_r^s L_{lr} + \Psi_m^s, \tag{3.15}$$

$$\Psi_m^s = L_m (I_s^s + I_r^s), \tag{3.16}$$

where Ψ_m^s is the air gap flux, L_m is the magnetizing inductance, L_{ls} is the stator leakage inductance, and L_{lr} is the rotor leakage inductance.

Taking into account Equations (3.14) and (3.15), the stator and rotor voltage equations can be rewritten in the form

$$U_s^s = R_s I_s^s + j\omega_s L_{ls} I_s^s + j\omega_s L_m (I_s^s + I_r^s), \tag{3.17}$$

$$U_r^s = R_r^s I_r^s + j\omega_{slip} I_r^s L_{lr}^s - j\omega_r \Psi_r^s + j\omega_{slip} L_m (I_s^s + I_r^s). \tag{3.18}$$

In (Abad et al., 2011), the following method to derive the rotor electrical parameters in the stator reference frame is proposed.

The induced EMF on the stator can be written as

$$E_s = \sqrt{2}\pi N_s K_s f_s \phi_m, \tag{3.19}$$

where N_s is the number of turns in the stator, K_s is the stator winding factor, and ϕ_m is the magnetizing flux.

The induced EMF on the rotor is

$$E_r = \sqrt{2}\pi N_r K_r f_{slip} \phi_m, \tag{3.20}$$

where N_r is the number of turns in the rotor, and K_r is the rotor winding factor.

By deriving the ratio of Equation (3.20) to (3.19), and taking into account Equation (3.4), the following expression can be written

$$\frac{E_{\mathrm{r}}}{E_{\mathrm{s}}} = \frac{sN_{\mathrm{r}}K_{\mathrm{r}}}{N_{\mathrm{s}}K_{\mathrm{s}}}, \tag{3.21}$$

where, in general and particularly in wind power applications, doubly-fed induction machines are specially designed with the ratio of the stator and rotor winding factor approximately equal to 1 (Abad et al., 2011)

$$\frac{K_{\mathrm{r}}}{K_{\mathrm{s}}} \cong 1\,. \tag{3.22}$$

Denoting the turns ratio $\frac{N_s}{N_r}$ in Equation (3.21) by k_{sr}, the relation between the stator and the rotor EMF is obtained

$$\frac{E_{\mathrm{r}}}{E_{\mathrm{s}}} = \frac{s}{k_{\mathrm{sr}}}\,. \tag{3.23}$$

Thus, the rotor EMF referred to the stator windings number of turns is

$$E_{\mathrm{r}}^{\mathrm{s}} = k_{\mathrm{sr}}E_{\mathrm{r}}. \tag{3.24}$$

By referring the rotor parameters to the stator winding number of turns, the following expressions are obtained (Muljadi et al., 2012):

$$R_{\mathrm{r}}^{\mathrm{s}} = R_{\mathrm{r}}k_{\mathrm{sr}}^2, \tag{3.25}$$

$$L_{\mathrm{lr}}^{\mathrm{s}} = L_{\mathrm{lr}}k_{\mathrm{sr}}^2, \tag{3.26}$$

$$I_{\mathrm{r}}^{\mathrm{s}} = \frac{I_{\mathrm{r}}}{k_{\mathrm{sr}}}, \tag{3.27}$$

$$U_{\mathrm{r}}^{\mathrm{s}} = k_{\mathrm{sr}}U_{\mathrm{r}}. \tag{3.28}$$

Therefore, the DFIG equivalent circuit in the stator reference frame can be derived (Figure 3.4).

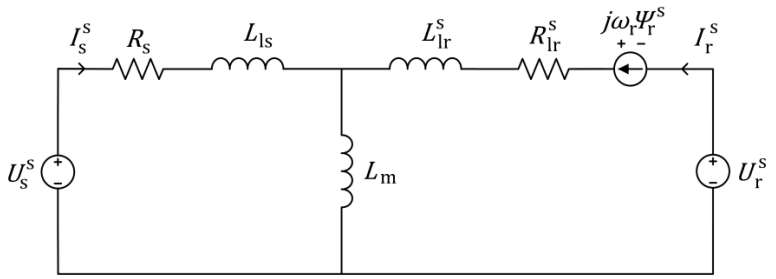

Figure 3.4: DFIG equivalent circuit in the stator reference frame.

3.4 DC link and LCL filter

The DC link capacitor model can be presented in terms of the stored energy, W_{DC} ,

$$W_{DC} = \frac{1}{2} C_{DC} U_{DC}^2 , \tag{3.29}$$

where C_{DC} is the DC link capacitance and U_{DC} is the DC link voltage.

Here, it can be assumed that the positive rotor power P_r is delivered to the rotor, and the positive filter power P_f to the LCL filter (Figure 3.5).

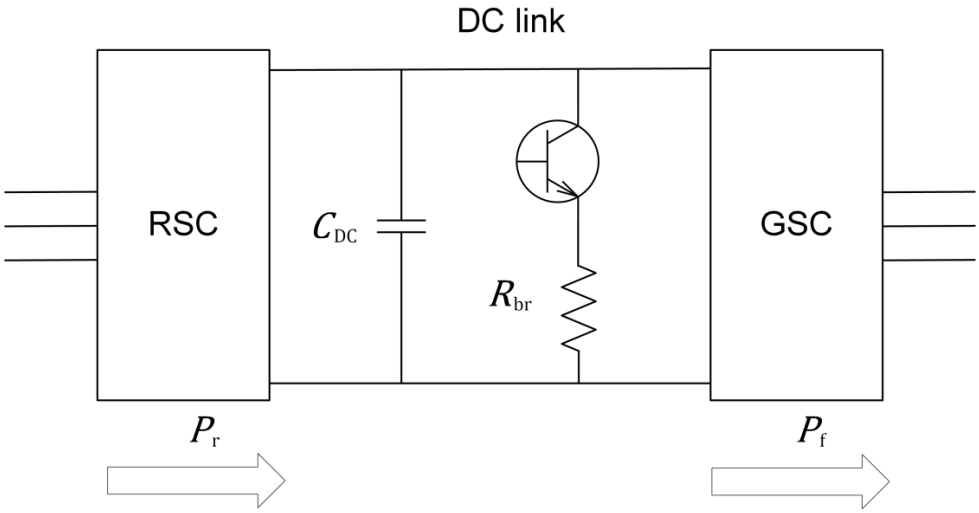

Figure 3.5: DC link capacitor in the back-to-back converter. The arrows define positive directions to the power supplied to the rotor P_r and to the grid filter P_f.

Thus, the DC link voltage remains constant, if

$$\frac{1}{2} C_{DC} \frac{d(U_{DC}^2)}{dt} = P_\mathrm{r} - P_\mathrm{f} = 0. \tag{3.30}$$

The brake resistor R_{br} should be used to dissipate power from the WT, if grid voltage dips occur. In this context, the WT power cannot decrease instantaneously during a grid fault, and the excess energy starts to overcharge the DC link capacitor, thereby leading to an overvoltage. Thus, the brake chopper is switched on and the brake resistor starts to consume energy and convert it into heat (Chaudhary et al., 2009).

An LCL filter is used to attenuate the PWM harmonics caused by the GSC. The parameters of the filter are selected based on the converter rated values, switching and resonant frequencies, and the maximum peak-to-peak current. Additionally, the desired attenuation rate of the expected current ripple is used to calculate the LCL filter parameters. The equivalent electrical circuit is shown in Figure 3.6 (Reznik et al., 2013).

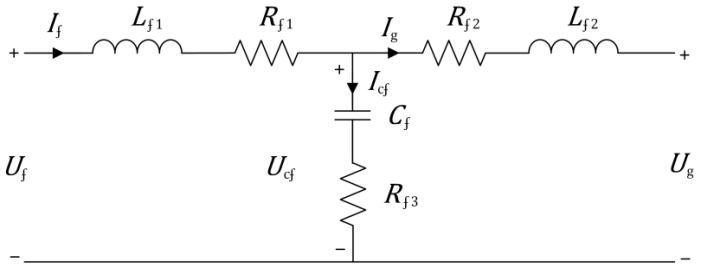

Figure 3.6: Equivalent electrical circuit of the LCL filter.

In Figure 3.6, I_f and I_g are filter currents on the inverter and the grid side, respectively, I_cf is the capacitor current, U_f and U_g are filter voltages on the inverter side and the grid side, respectively, and U_cf is the filter voltage of the RC branch. The parameters of the filter are the inverter-side inductor $L_{\mathrm{f}1}$, the grid-side inductor $L_{\mathrm{f}2}$, the corresponding inductor resistances $R_{\mathrm{f}1}$ and $R_{\mathrm{f}2}$, and the capacitor C_f. The resistor $R_{\mathrm{f}3}$, is connected in series with the capacitor C_f, which is used to avoid resonance with the grid. However, resistor losses are the drawback of the proposed solution.

3.5 Control system of DFIG

The control system of the DFIG-based WT comprises the generator torque and stator reactive power control at the RSC and the DC link voltage control at the GSC (Figure 3.7). The control system used in the PLECS model of the DFIG is derived based on (Petersson, 2005) and described in detail in Appendix A.

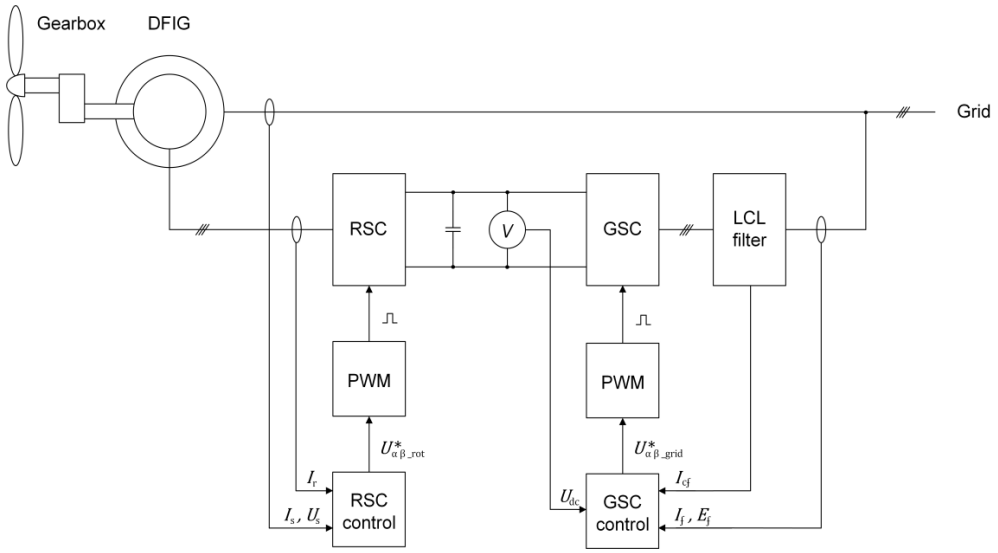

Figure 3.7: General scheme of the DFIG control system.

The control system of the RSC consists of outer loops for the reactive power and generator torque control and inner loops for current control. The stator-flux-oriented frame is applied in the current control system so that the stator flux vector Ψ_s is aligned with the d-axis. Thus, the d-axis current component is used to control the reactive power, and the q-axis current component relates to the generator torque. However, in this study, the q-axis reference current is derived from a static relationship with the reference generator torque, in other words, there is no rotational speed feedback signal and $T_g = T_g^{ref}$. In the inner loops for the current control, the term 'active resistance' R_a is introduced in order to damp the disturbances from the compensating terms. The PI controller parameters are derived based on the internal model control (IMC) method, where the controller transfer function is defined based on the reciprocate transfer function of the plant in order to perfectly track the reference signal with a desired bandwidth, assuming that the plant parameters are known and the plant model is stable (Harnefors & Nee, 1998).

The RSC control diagrams for the d- and q-axes are shown in Figure 3.8 and Figure 3.9.

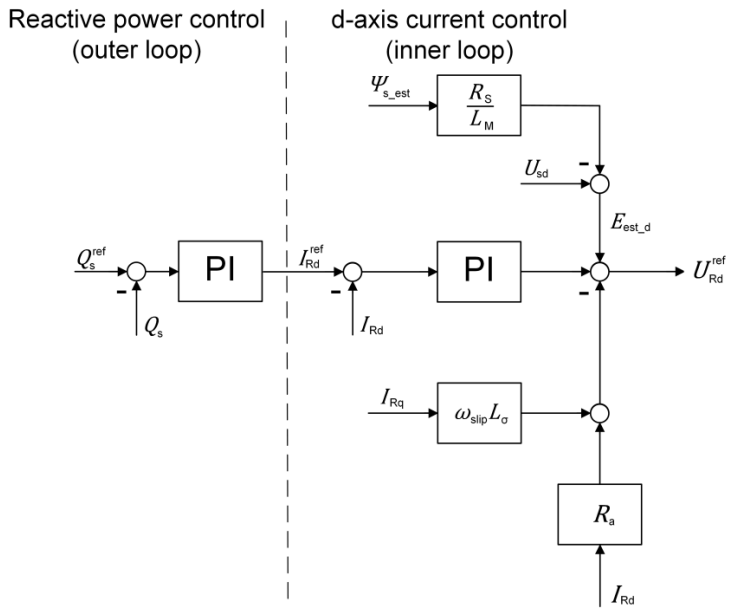

Figure 3.8: Reactive power and d-axis current control scheme for the RSC.

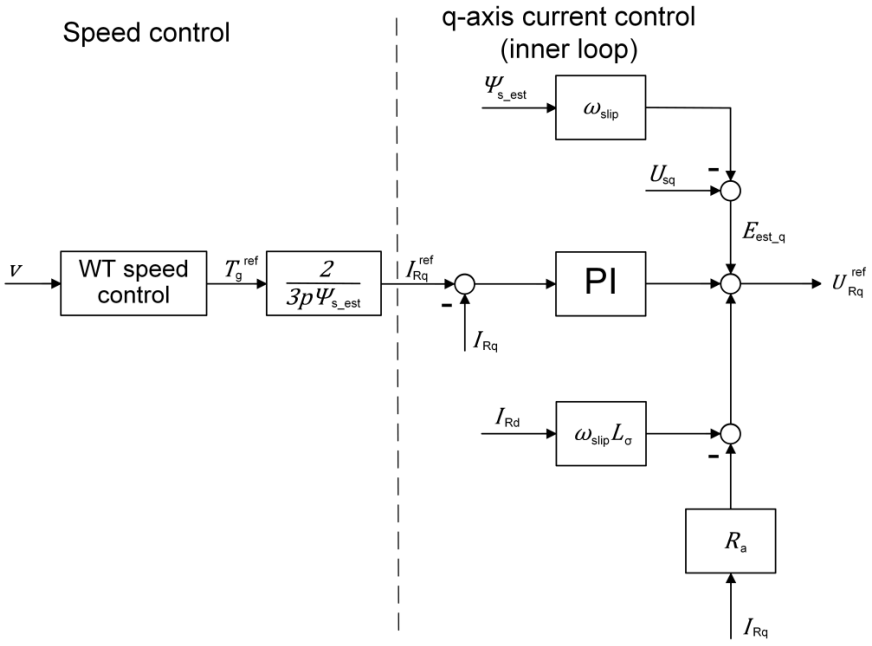

Figure 3.9: Speed control and q-axis current control scheme for the RSC.

The control system for the GSC consists of an outer loop for the DC link voltage and the inner loops for the current control (Figure 3.10). The outer loop for the DC link voltage control is intended to produce the reference d-axis current $I_{\mathrm{d}}^{\mathrm{ref}}$ from the DC link voltage error in terms of U_{DC}^2. The latter term is related to the energy stored in the DC link. Additionally, the active damping gain G_{a} is added to the outer loop. The reactive current reference is set to zero, thereby eliminating the outer control loop of the q-axis. However, as mentioned above, the reactive power control in the GSC is an "optional feature for exchanging the reactive power between the DFIG and the grid" (Akhmatov, 2003).

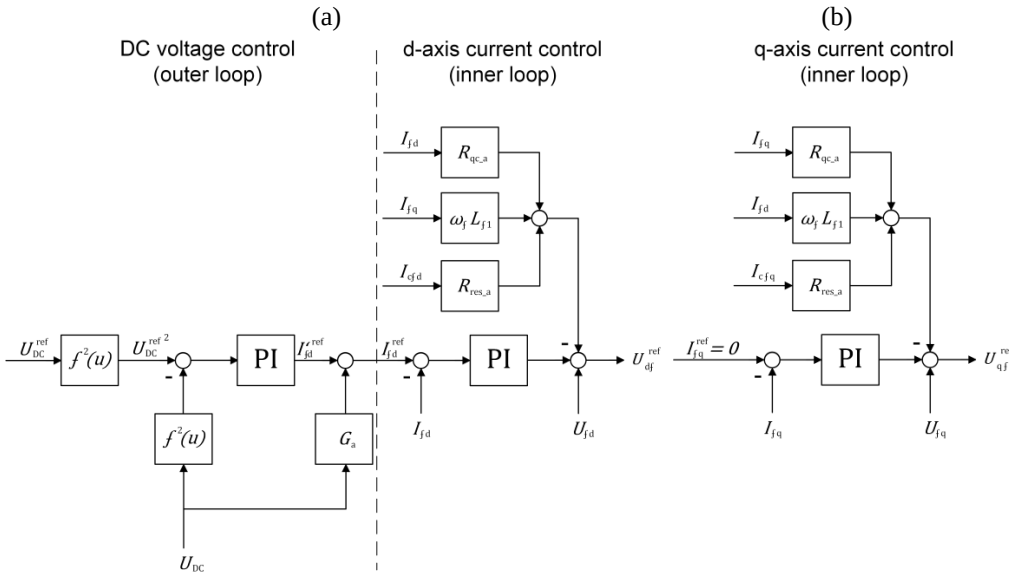

Figure 3.10: GSC control scheme. (a) d-axis current control. (b) q-axis current control.

3.6 IGBT power loss calculation

The IGBT and diode power losses P_{loss} include the conduction loss P_{cond} and the switching loss P_{sw}, whereas the diode switching loss is given by the reverse recovery loss

$$P_{\mathrm{loss}} = P_{\mathrm{cond}} + P_{\mathrm{sw}} . \tag{3.31}$$

The conduction loss occurs when the power device is in on-state, conducting the steady-state collector current I_{c}, and the steady-state collector-emitter voltage U_{CE} is applied. The conduction loss depends on the load current, the junction temperature, and the duty cycle.

The IGBT on-state voltage-current characteristics, provided by the manufacturer, are used for the instantaneous conduction loss calculation. Thus, the conduction loss as a function of the collector current I_c, the collector-emitter threshold voltage U_{CE0}, and the on-state resistance R_{ce}, can be given as follows (Srajber, 1992), (Schnell, 2004)

$$P_{cond}(t) = U_{CE}(t) \cdot I_c(t) = (U_{CE0} + R_{ce} I_c(t)) \cdot I_c(t). \tag{3.32}$$

The collector-emitter voltage U_{CE} and the collector current I_c are dependent on the junction temperature. Typically, in the output characteristics of the device provided by the manufacturer, the curves for $I_c(U_{CE})$ are presented at several junction temperatures.

Because the IGBT conducts one-half period, the average conduction loss is calculated by integrating one-half sine wave over the $T_0/2$ time interval, where T_0 is a period of the sine wave with a fundamental frequency f_0

$$P_{cond\_IGBT} = \frac{1}{T_0} \int_0^{\frac{T_0}{2}} ((U_{CE0} I_c + R_{ce} I_c^2) \cdot \tau(t)\, dt, \tag{3.33}$$

where $\tau(t)$ reflects the switching pattern of the IGBT, and thus $\tau(t) = 1$ or $\tau(t) = 0$, in accordance with the modulation index m and the phase angle φ

$$\tau_{IGBT}(t) = \frac{1}{2}(1 + m \sin(\omega t + \varphi)). \tag{3.34}$$

Taking into consideration the collector current $I_c = \widehat{I_c} \sin(\omega t)$ and Equations (3.33)–(3.34), the IGBT conduction losses are calculated as follows (Schnell, 2004)

$$P_{cond\_IGBT} = \frac{1}{2} \left(U_{CE0} \cdot \frac{\widehat{I_c}}{\pi} + R_{ce} \cdot \frac{\hat{I}_c^2}{\pi} \right) + m \cdot \cos\varphi \left(U_{CE0} \cdot \frac{\widehat{I_c}}{8} + \frac{1}{3\pi} \cdot R_{ce} \cdot \hat{I}_c^2 \right). \tag{3.35}$$

The IGBT switching loss occurs during transients, whereas the collector current increases I_c and the collector-emitter voltage U_{CE} drops to saturation during turn-on and, vice versa, during turn-off. The switching loss depends on the DC link voltage level, the load current, the junction temperature, and the switching frequency.

The IGBT switching losses are calculated based on the turn-on and turn-off switching energies, which are both a function of the collector current I_c. The switching energy can be approximated by the polynomial function

$$E_{sw\_IGBT} = E_{on} + E_{off} = A \cdot I_c^2 + B \cdot I_c + C. \tag{3.36}$$

Because the switching transients are highly dependent on the IGBT blocking voltage, Equation 3.36 is approximated as

$$E_{\mathrm{sw\_IGBT}} = \left(A \cdot \hat{I}_{\mathrm{c}}^2 + B \cdot \widehat{I_{\mathrm{c}}} + C \right) \cdot \frac{U_{\mathrm{DC}}}{U_{\mathrm{base}}}, \tag{3.37}$$

where U_{DC} is the DC link voltage and U_{base} is the base value of the DC link voltage.

In the thermal description of the module, the switching energy data are added as a 3D map, which shows the dependence of the switching energy on the blocking voltage and the junction temperature.

Taking into account the switching frequency f_{sw}, the switching loss can be calculated as

$$P_{\mathrm{sw\_IGBT}} = f_{\mathrm{sw}} \sum_{n} E_{\mathrm{sw\_IGBT}}(\widehat{I_{\mathrm{c}}}), \tag{3.38}$$

where n is the positive integer indicating the number of switchings.

Because the diode operates when the IGBT is turned off, the switching pattern of the diode is

$$\tau_{IGBT}(t)(t) = \frac{1}{2}(1 - m\sin(\omega t + \varphi)). \tag{3.39}$$

Thus, the conduction loss of the diode can be written as

$$P_{\mathrm{cond\_diode}} = \frac{1}{2}\left(U_{\mathrm{CE0}} \cdot \frac{\widehat{I_{\mathrm{c}}}}{\pi} + R_{\mathrm{ce}} \cdot \frac{\hat{I}_{\mathrm{c}}^2}{\pi}\right) - m \cdot \cos\varphi \left(U_{CE0} \cdot \frac{\widehat{I_{\mathrm{c}}}}{8} + \frac{1}{3\pi} \cdot R_{\mathrm{ce}} \cdot \hat{I}_{\mathrm{c}}^2\right). \tag{3.40}$$

The diode switching loss is induced by the turn-off reverse-recovery current. Here, the reverse-recovery energy is given as a polynomial function of the diode forward current I_{fw}

$$E_{\mathrm{sw\_diode}} = \left(A \cdot I_{\mathrm{fw}}^2 + B \cdot I_{\mathrm{fw}} + C \right) \cdot \frac{U_{\mathrm{DC}}}{U_{\mathrm{base}}}. \tag{3.41}$$

The diode switching loss as a function of switching frequency can be expressed as

$$P_{\mathrm{sw\_diode}} = f_{\mathrm{sw}} \sum_{n} E_{\mathrm{sw\_diode}}(I_{\mathrm{f}}). \tag{3.42}$$

In this research, the power loss estimation is carried out in the PLECS interface. In the PLECS model, ideal switches are assumed, however, containing the detailed power loss data. Thus, the model accepts a high simulation speed and provides accurate calculation results (PLECS, 2016). At each switching event, the model records the IGBT operating parameters, such as collector current, junction temperature, and blocking voltage. Based on the recorded data and predefined look-up tables with the switching energy and on-state characteristics, the switching losses and the conduction loss are defined correspondingly. An example of a look-up table used in the PLECS model is shown in Figure 3.11 (a, b) (PLECS, 2016).

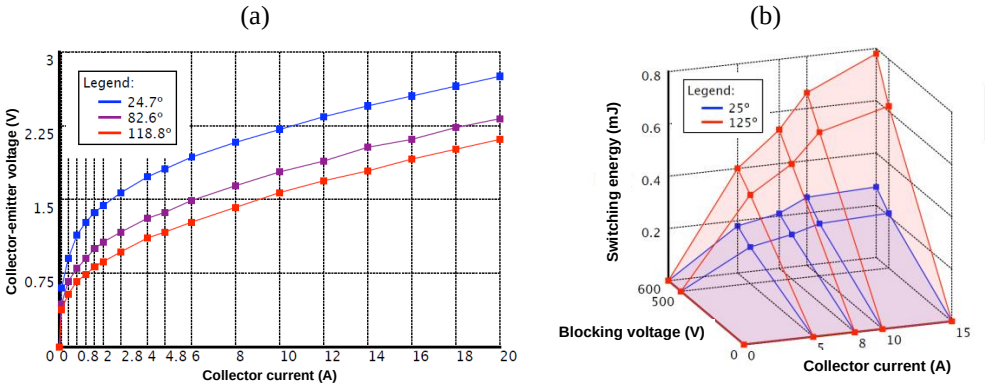

Figure 3.11: Example of look-up tables used in the PLECS model for power loss calculation (PLECS, 2016). (a) On-state voltage characteristics as a function of collector current and junction temperature. (b) Switching energy as a function of collector current and junction temperature.

3.7 Dynamic estimation of junction temperature

The junction temperature is modelled by implementing a thermal model of the power device. The IGBT thermal impedance is identical with the electrical RC circuit, where the electrical resistance and capacitance correspond to the thermal resistance and capacitance. Similarly, the electrical current corresponds to the heat flux, and the voltage of the RC element corresponds to the temperature difference between the IGBT layers. Thus, by implementing the thermal impedance, the modelled junction temperature reflects the transient response to the power input.

The Cauer thermal network assumes individual RC elements for each individual physical layer of the module (Figure 3.12). The thermal layers can be assigned to the chip, chip solder, DCB substrate, substrate solder, base plate, thermal grease, and the heat sink. Thus, the Cauer model can be used to estimate the temperature of each physical layer

(Yun et al., 2001). However, the Cauer topology assumes that the thermal impedances of the physical layers are known.

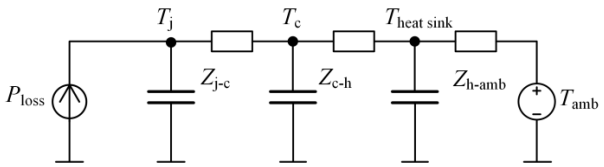

Figure 3.12: Cauer-type thermal network of IGBT module.

In Figure 3.12, the term Z_{j-c} denotes the thermal impedance from the junction to the case, Z_{c-h} from the case to the heat sink, and Z_{h-amb} from the heat sink to the ambient. The temperatures T_j, T_c, $T_{heat\ sink}$, and T_{amb} are the junction, case, heat sink, and ambient temperatures, respectively.

For the sake of convenience, a Foster-type thermal network can be used (Figure 3.13(a)). It also assumes a multilayer structure with the use of thermal resistance and time constant, however, with no physical meaning of each individual layer. The thermal resistances and time constants of the four-layer network from the IGBT junction to the case can be found in the manufacturers' documentations (ABB, 2014b). The thermal resistance of the thermal grease interface and the heat sink can also be added to the model.

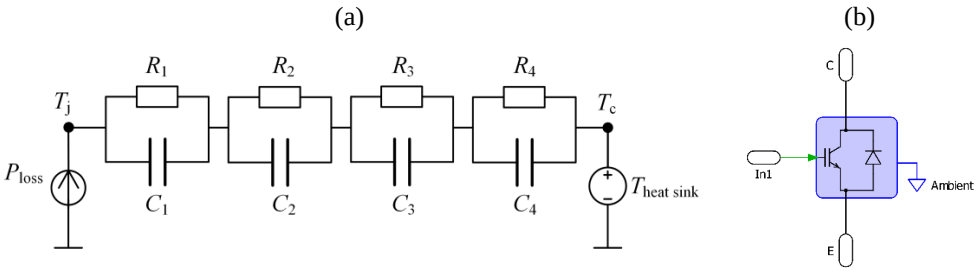

Figure 3.13: IGBT module in the PLECS model. (a) Foster thermal network. (b) IGBT placed on the heat sink.

In the PLECS model used in this research, a Foster-type thermal model is used. As shown in the look-up tables in Figure 3.11, the temperature estimation is carried out by an interpolation procedure during the model operation.

The thermal description of the IGBT module in the PLECS environment includes $I_c(U_{CE})$ maps, where the temperature dependence is reached by interpolation. The PLECS model assumes that the IGBT module is placed on a heat sink (Figure 3.13(b)). In the model, heat is transferred to the ambient through the thermal resistance. The constant ambient

temperature of 40°C is assumed as an average converter cabinet temperature, and thus, long-term ambient temperature variations are not included in the model

3.8 Case study of a 2 MW DFIG

The DFIG wind turbine is modelled using the PLECS blockset in the MATLAB Simulink environment. The PLECS is a rapid and robust simulation tool, where the model components can be modelled in multi-physical domains (Luo, 2014). The DFIG demo model from the PLECS includes the blades, the shaft, and the hub modelled in the mechanical domain, and assuming elastically connected components. The power electronics is modelled in the thermal domain, where the conduction and switching losses and the cooling system are taken into account. The three-winding transformer, modelled in the magnetic domain, includes the non-linear magnetizing current characteristics.

However, in the present research, the DFIG demo is used for the thermal modelling of the power electronics, and thus, the original PLECS model was modified accordingly. The WT includes only the electrical circuits of the DFIG, the BTB power converter, the transformer, the transmission line, the grid, and the control systems of the RSC and the GSC. The model is run at several steady-state rotational speeds. Thus, two input parameters are applied; the generator electromagnetic torque, and the rotational speed, according to the operating modes as discussed in Section 2.3.4 (Figure 3.14). As four distinct operating modes are distinguished, the corresponding speed and torque relationship should be applied as an input (Table 3.2). The details of the calculation of the input mechanical speed and the generator torque are presented in Appendix B. The average power loss calculation block has been added to the model.

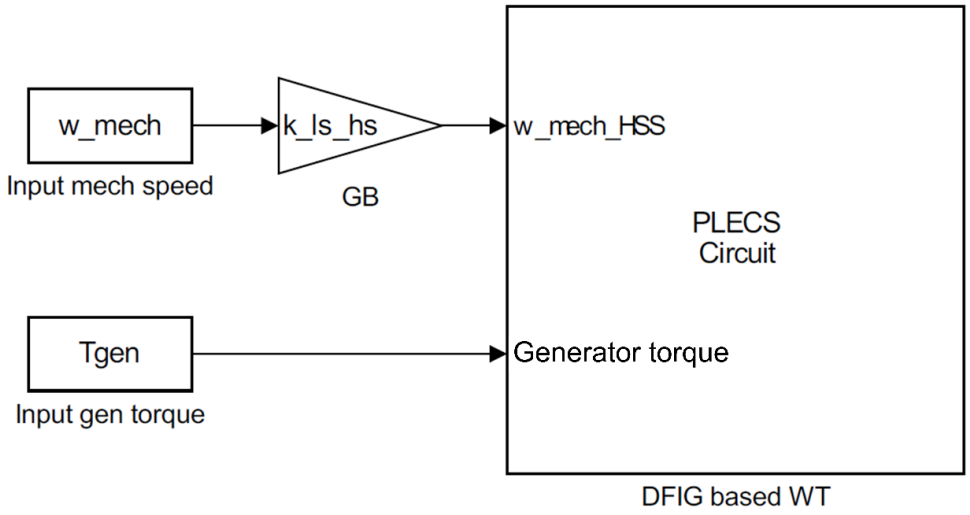

Figure 3.14: Overview of the model in MATLAB Simulink.

Table 3.2: Input rotational speed on the low speed side of the shaft and generator torque.

Operating mode	Rotational speed, lss (rad/s)	Generator torque (Nm)
1	1.1	55.9
	1.1	506
	1.1	1080
	1.1	1730
	1.1	2420
	1.1	2650
2	1.2	3150
	1.3	3700
	1.4	4300
	1.5	4930
	1.6	5610
	1.7	6330
	1.73	6540
3	1.73	6770
	1.73	7860
	1.73	8930
	1.73	9940
	1.73	10900
	1.73	11800
4	1.73	11800

As mentioned above, the DFIG demo model (Figure 3.15) from the PLECS library is used, and the electrical subsystem parameters remain unchanged (Table 3.3).

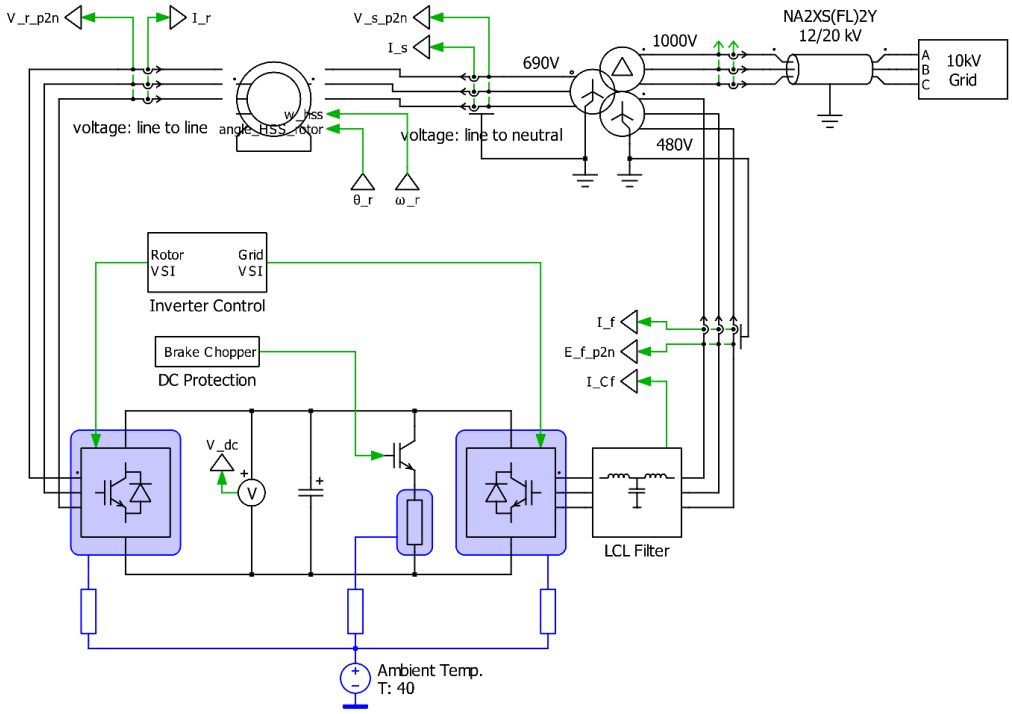

Figure 3.15: DFIG subsystem modelled in PLECS (PLECS library, 2016).

Table 3.3: DFIG parameters (PLECS library, 2016).

Parameter	Value
Rated power	2 MW
Rated voltage, peak, line-to-line	690 V
Synchronous angular speed	314 rad/s
Number of pole pairs	2
Gear ratio	100
Stator resistance	0.022 Ohm
Rotor resistance	0.0018 Ohm
Stator leakage inductance	0.12 mH
Rotor leakage inductance	0.05 mH
Magnetizing inductance	2.9 mH
Stator to rotor turns ratio	1/2.6
DC link capacitor	53 mF
Switching frequency	5kHz
Converter-side inductance of the LCL filter	0.48 mH
Grid-side inductance of the LCL filter	0.044 mH
Capacitance of the LCL filter	57 µF

As mentioned above, the 1.7 kV IGBT module is suitable for the 690 V AC line-to-line terminal voltage of the power converter. The Foster-type thermal model parameters of the ABB 5SNA 1600N170100 IGBT module are presented in Table 3.4 (ABB, 2014b).

Table 3.4: Thermal impedance of the ABB 5SNA 1600N170100 IGBT module.

Thermal impedance	$Z_{(j\text{-}c)}$				$Z_{(c\text{-}h)}$
	Layer 1	Layer 2	Layer 3	Layer 4	
R_{iIGBT}, K/kW	7.59	1.8	0.743	0.369	12
τ_{iIGTB}, ms	202	20.3	2.01	0.52	
R_{iDiode}, K/kW	12.6	2.89	1.3	1.26	24
τ_{iDiode}, ms	210	29.6	7.01	1.49	

3.8.1 **DFIG electrical characteristics**

In Figure 3.16(a), the generator slip and the rotor angular frequency, calculated using Equation (3.3) and (3.4), respectively, are presented. Obviously, in the wind speed zone with the optimal rotational speed control, the slip decreases from 0.3 to -0.1. The slip is zero at the 8.1 m/s wind speed, where the sub-synchronous operating mode changes to the super-synchronous one.

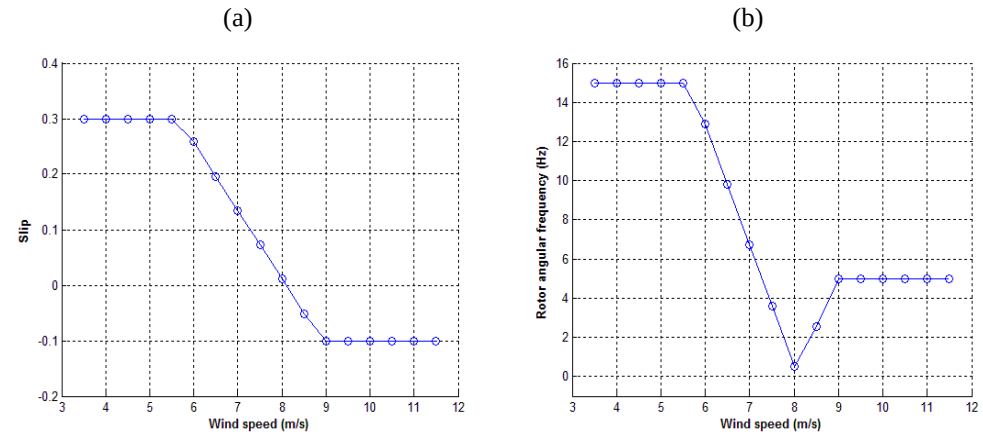

Figure 3.16: DFIG operation in steady states. (a) Generator slip. (b) Absolute value of rotor frequency.

The power factor in Figure 3.17(a) is calculated using the equation

$$\cos\varphi = \cos\angle(U_{\mathrm{r}}, I_{\mathrm{r}}), \tag{3.43}$$

where φ is the angle between the voltage and current vectors U_{r} and I_{r}.

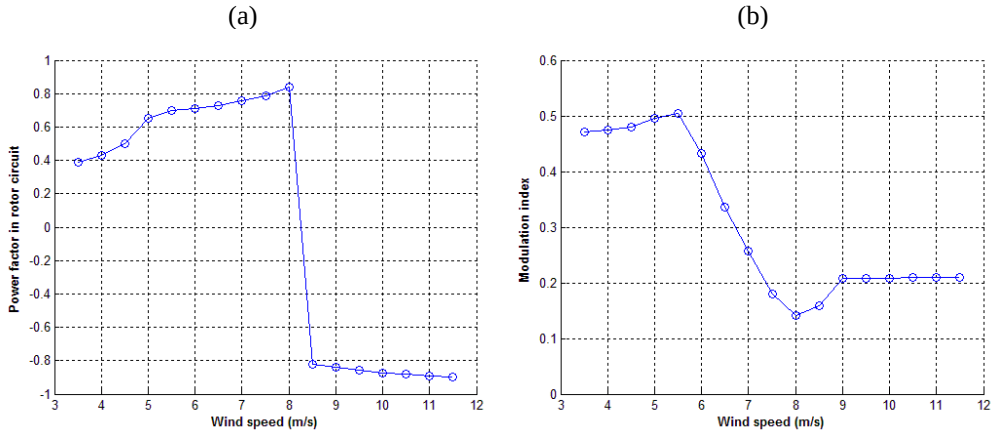

Figure 3.17: DFIG operation in steady states. (a) Power factor of the rotor circuit. (b) Modulation index of the RSC.

In the sub-synchronous mode, the power factor increases because of the decreasing angle between the rotor voltage and current vectors. Here, the angle decreases from 67° to 32º,

and $\varphi < 90^{o}$ with the leading voltage vector. The latter indicates negative rotor power in this mode, which means that the rotor absorbs power from the grid. Then again, in the super-synchronous mode, the power factor decreases. In this case, the angle increases from 145° to 153º, and $\varphi > 90^{o}$. Thus, the rotor generates power to the grid.

Figure 3.17(b), the modulation index m of the RSC voltage amplitudes is shown

$$m = \frac{\hat{U}_{\mathrm{r}}}{U_{\mathrm{DC}}}, \tag{3.44}$$

where $\hat{U}_{\mathrm{r}}$ is the rotor phase voltage amplitude and U_{DC} is the DC link voltage.

The minimum modulation index is obtained at the synchronous operating point, 8.1 m/s, the root mean square (rms) value of the rotor voltage in Figure 3.18(a).

According to the RSC control system, the electromagnetic torque is controlled to be proportional to the current. Thus, the increasing torque (Figure 3.19(a)) induces an increase in the rotor current in Figure 3.18(b).

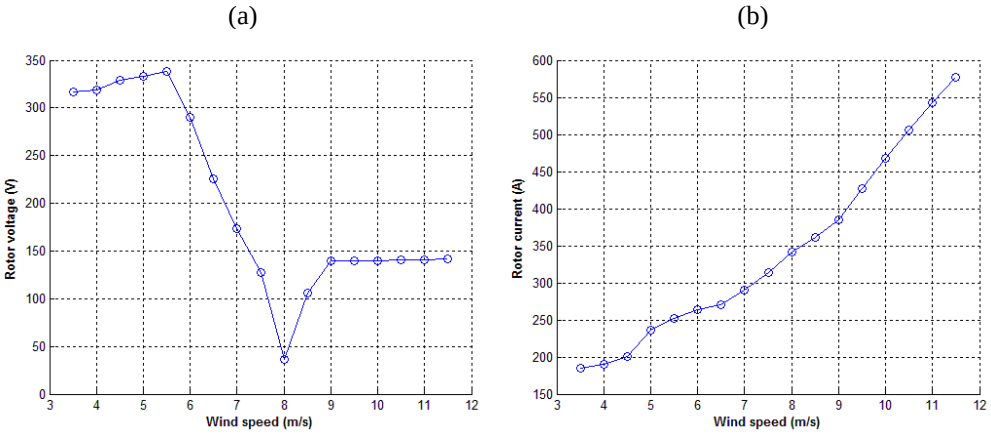

Figure 3.18: DFIG operation in steady states. (a) Rotor voltage. (b) Rotor current.

In Figure 3.19(b), the DFIG power curves are shown. Obviously, the rotor power is negative in the sub-synchronous mode at the wind speed < 8.1 m/s, and positive at > 8.1 m/s.

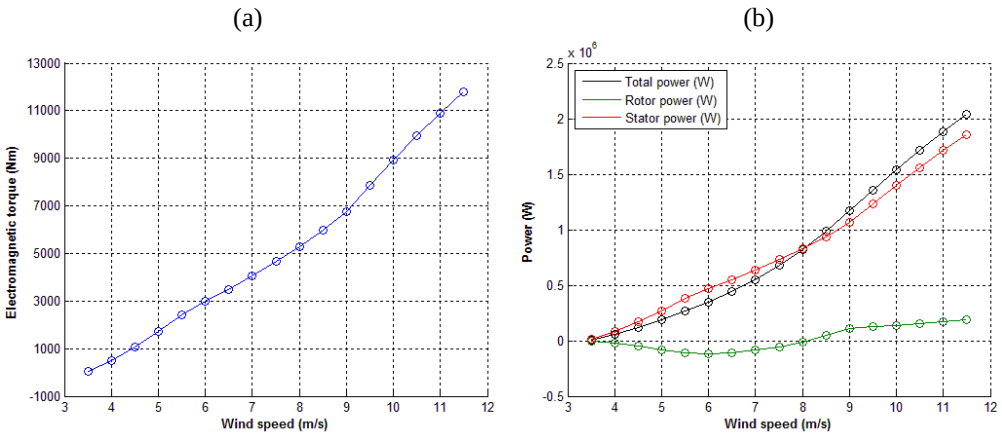

Figure 3.19: DFIG operation at steady states. (a) Electromagnetic torque. (b) WT power.

Because the doubly-fed machine operates as a generator, the stator always delivers active power to the grid and remains positive in Figure 3.19. The rotor, which operates in the sub- or super-synchronous modes, consumes or delivers power to the grid through the power converter. The total power is always positive and increases with the wind speed.

In Table 3.5, the electrical parameters, such as the rotor slip frequency f_{slip}, the slip s, the modulation index m, the phase angle φ, and the power factor $\cos\varphi$ of the RCS, operating at different wind speeds, are presented.

Table 3.5: Electrical parameters of the rotor-side converter at different wind speeds.

v (m/s)	4	5	6	7	8	9	10	11
ω_{m} (rad/s)	1.10	1.10	1.17	1.36	1.55	1.73	1.73	1.73
f_{slip} (Hz)	15	15	12.90	6.71	0.53	5	5	5
s	0.30	0.30	0.26	0.13	0.01	-0.1	-0.1	-0.1
φ (°)	64.60	56.60	48.20	42.75	34.42	-146.25	-150.50	-152.62
$\cos\varphi$	0.43	0.55	0.63	0.63	0.83	-0.83	-0.87	-0.89
m	0.475	0.490	0.433	0.258	0.141	0.208	0.208	0.209

3.8.2 Thermal performance of the power converter

In Figure 3.20, the total power losses for the RSC and the GSC are shown.

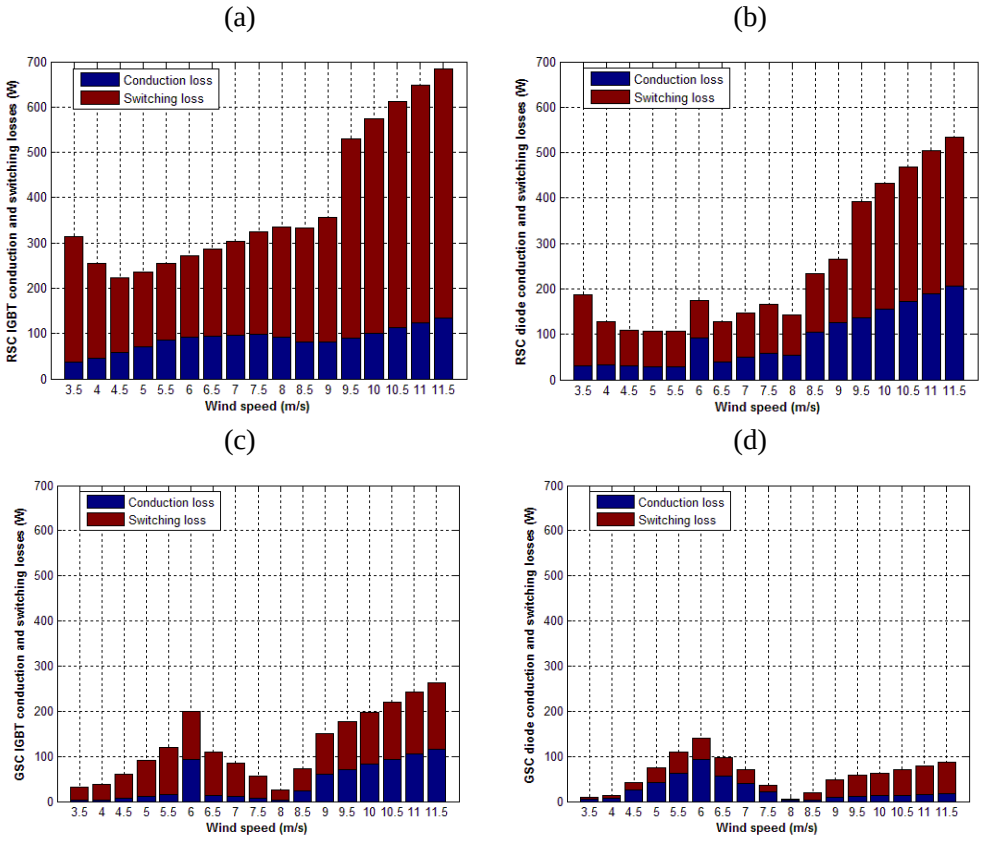

Figure 3.20: Power losses of the RSC and the GSC. (a) IGBT at RSC; (b) Diode at RSC. (c) IGBT at GSC; (d) Diode at GSC.

Obviously, the IGBT of the RSC shares more thermal stress than the diode. Because the RSC operates as an inverter in the sub-synchronous mode, the IGBT is expected to have higher power losses. Moreover, owing to the increasing power factor of the RSC, the power loss distribution between the IGBT and the diode shifts towards the IGBT. The decrease in the modulation index induces more power loading on the diode. In the super-synchronous mode, the modulation index remains at lower values than in the sub-synchronous mode because of the slip limitation. Therefore, the relative difference between the IGBT thermal loading and the diode becomes lower. Additionally, the

negative power factor means longer on-state duration of the diode, thereby inducing more power losses.

In the GSC, the total power losses obtained at the wind speed of 6 m/s are comparable with the losses at higher wind speeds. The tendency of the converter power increase at 6 m/s and decrease at 8 m/s, as shown in Figure 3.20(c, d), is more evident on the GSC than the RSC. In the sub-synchronous mode, the GSC operates as a rectifier. Thus, the diode losses are higher in the sub-synchronous mode than in the super-synchronous mode. The IGBT losses in the super-synchronous mode are higher than in the sub-synchronous mode.

In Figure 3.21, an example of junction temperature fluctuations at the 11 m/s wind speed operating point is shown. Obviously, owing to the higher operating frequency on the grid side, the temperature fluctuations have a lower amplitude.

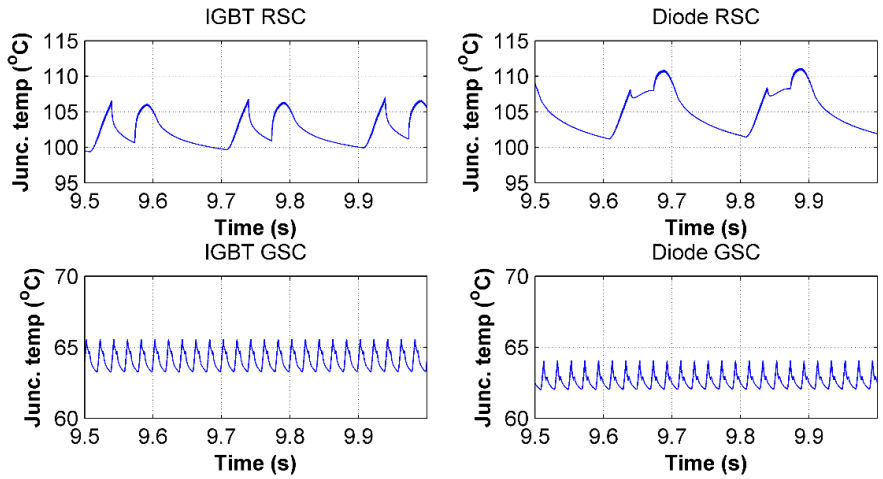

Figure 3.21: Junction temperature fluctuations at 11 m/s at the RSC and the GSC.

In Figure 3.22, the junction temperature mean values and temperature changes are shown.

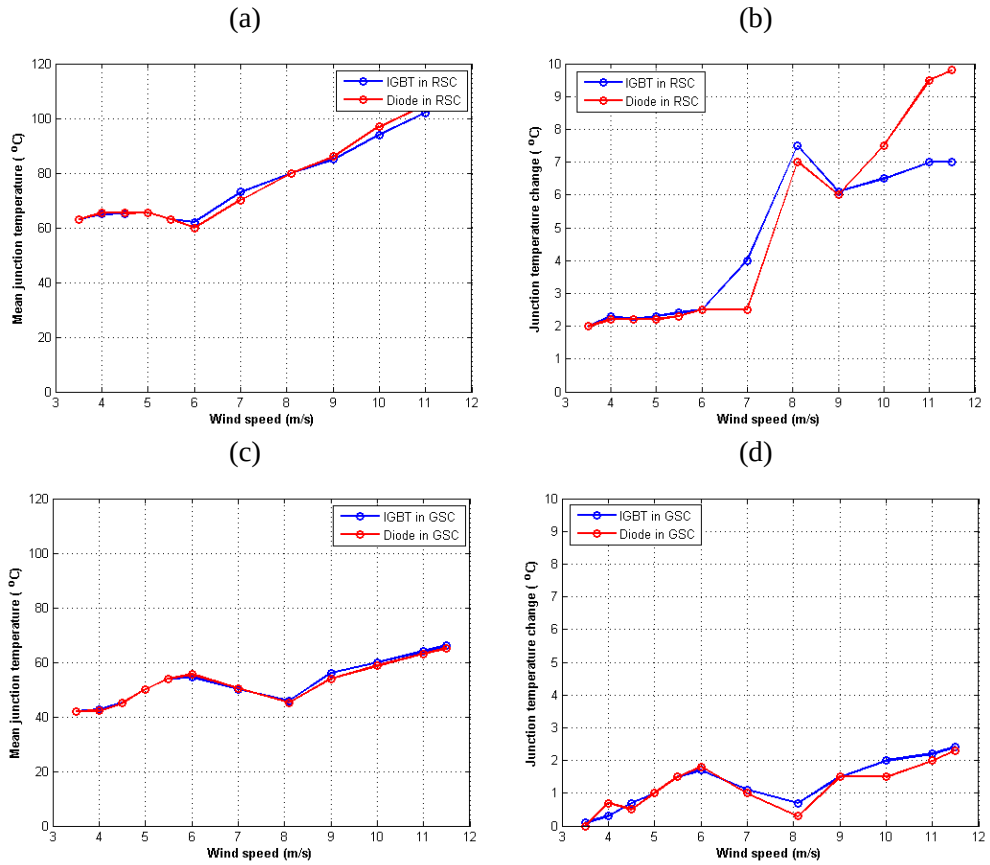

Figure 3.22: Junction temperature over the wind speed range. (a) Mean value, RCS. (b) Temperature changes, RCS. (c) Mean value, GSC. (d) Temperature changes, GSC.

In Figure 3.22 (a, c), the general tendency of the increasing mean value of the junction temperature as a result of the increasing rotor current can be observed. The temperature swings (Figure 3.22(b, d)) also increase with the wind speed; however, the local maximum owing to the minimum operating frequency at 8.1 m/s can be observed at the RSC. In the GSC, the zero slip operating point is characterized by the local minimum. The junction temperature is generally higher in the RCS than in the GSC.

3.9 Summary

The general configuration of the DFIG was presented in this chapter. The principles of operation in the sub- and super-synchronous modes were discussed. The DFIG model was taken from the PLECS blockset library; however, certain modifications were introduced by the author, namely, the mechanical subsystem was modified and a block for the IGBT and diode power loss calculation was added. The operation of the DFIG was provided in four operating zones. Thus, the corresponding rotational speed and the generator torque were applied as inputs. The electrical equivalent circuit and the converter control system were described according the PLECS model.

The PLECS model simulations were performed at a set of steady-state wind speeds. According to the obtained results, the dynamics of the electrical parameters over the wind speed range strongly depend on the slip. Thus, the minimum of the rotor angular speed, modulation index, rotor voltage, and power were observed at 8 m/s, whereas the zero slip was observed at 8.1 m/s.

It was observed that the amplitude of the junction temperature swings depends on the fundamental frequency. More specifically, the local maximum is at 8.1 m/s, where the fundamental frequency of the RSC is zero. At the GSC, the zero slip operating point characterized by the local minimum junction temperature swing.

4 IGBT lifetime estimation

In Chapter 4, the lifetime estimation of the IGBT module for different failure mechanisms is performed. Section 4.1 describes the method to calculate the lifetime step by step. Section 4.2 introduces lifetime estimation models built in MATLAB and their parameters. In Sections 4.3–4.7, mathematic tools used in the method and results are presented.

4.1 IGBT lifetime estimation method

Lifetime estimation of the IGBT module is based on a thermal stress profile analysis including failure mechanisms and temperature fluctuations in the IGBT during the WT operation. The method includes transformation steps from the input wind speed dynamics to the consumed lifetime of the IGBT (Figure 4.1). The lifetime consumption is derived as a number of cycles during which 10 % of the module population fails (also known as B10 lifetime) (ABB, 2014a).

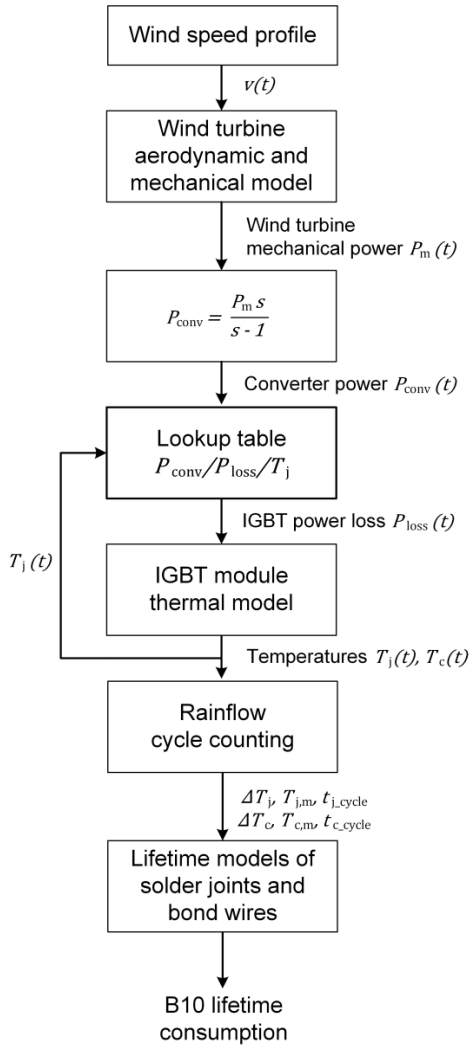

Figure 4.1: Lifetime estimation algorithm of the IGBT module.

The wind speed profile is synthesized using von Karman's turbulence model, which includes the site-specific TI (Nichita et al., 2002). The developed wind speed generation model can reflect both high and low frequency variations. However, in this study, the long-term component is modelled as a constant wind speed. Thus, the generated profile consists of turbulent wind speed variations around a specific average value. In this manner, several wind speed profiles are generated over a period of three hours at different mean wind speeds with the corresponding levels of the TI.

The generated turbulent wind speed is applied as an input to the WT aerodynamic and mechanical model. The aerodynamic block represents the power coefficient function,

which reflects the WT aerodynamic efficiency. The mechanical model represents operation of the one-mass system, driven by Newton's second law. The rotational speed and the blade pitch angle control strategy are implemented in order to regulate the WT performance in different operating modes.

The WT mechanical power and rotational speed are derived from the aerodynamic and mechanical model and used to calculate the generator slip and the converter power. A look-up table is used to define the IGBT power losses at the RSC and the GSC based on the converter power losses and the junction temperature. In the look-up table, the first dimension breakpoints are formed by a one-dimensional array of converter power data at different wind speeds. The second dimension breakpoints are the junction temperatures of 25 and 125°C. The output signal of the table is found correspondingly from the two-dimensional matrix of power losses by linear interpolation and extrapolation of the data. In this way, the data for the IGBT and diode power losses at the RSC and the GSC are defined in the look-up table.

The converter power losses, specified in the look-up table, are calculated a priori in the DFIG model (Figure 4.2). The model is discussed in detail in Chapter 3, and it includes the electrical circuit of the generator, the back-to-back power converter, the current control system, and the grid. As the DFIG model is simulated at several steady wind speeds, the power losses are averaged by fundamental frequencies.

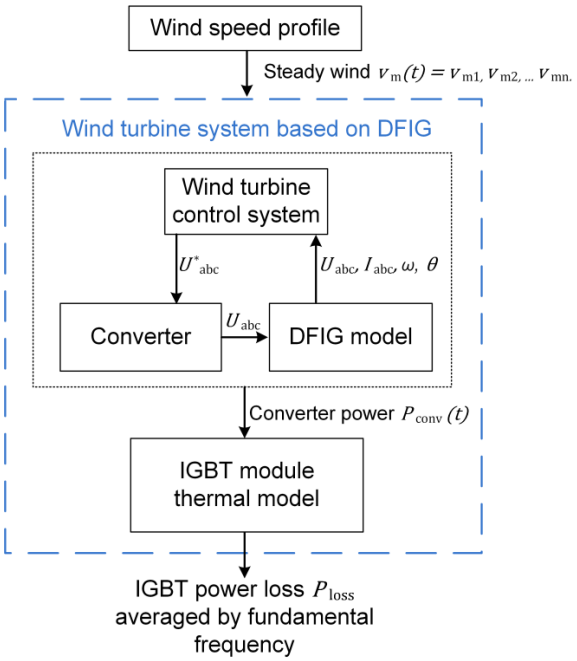

Figure 4.2: Representation of the DFIG-based WT used to compose the look-up table of the IGBT power losses.

A Cauer thermal network of the IGBT module is used to define the junction and case temperature after the power losses have been derived from the look-up table. The junction temperature is used as a feedback signal for the look-up table. Because the input of the thermal model is the power loss dynamics averaged by the fundamental frequency, the junction and case temperature dynamics will contain only the variations associated with the turbulent wind speed. Next, the cycle counting of the obtained junction and case temperature profiles is performed using a rainflow counting algorithm. This method is widely used in the stress and fatigue analysis. It determines the number of cycles of any arbitrary stress signal, cycle period, mean value, and amplitude of each counted cycle (Nieslony, 2009). Thus, the cycle counting results of the junction and case temperatures are obtained in different wind speed conditions.

The lifetime curves, developed by an IGBT module manufacturer (ABB, 2014a), are used to define the B10 number of cycles. The lifetime of the HiPak IGBT model in (ABB, 2014a) is estimated by applying a repetitive current and inducing the temperature cycles. The failure of the module is detected by a 5 % increase in the collector-emitter voltage U_{ce} or a 20 % increase in the thermal resistance R_{th}. The lifetime model also requires material fatigue data, where the cycles to failure are determined from the viewpoint of material properties. The lifetime models are given for the fatigue mechanisms in the solder joints (chips, conductor leads and base plate) and bond wires. Thus, each counted cycle is related to the corresponding consumed lifetime (CL). According to Miner's rule for cumulative damage, the obtained set of CLs at the specific mean wind speed can be aggregated. Hence, taking into account the one year wind distribution, the total consumed one-year B10 lifetime can be defined.

4.2 Case study of a 2 MW DFIG-based WT

4.2.1 WT mechanics, aerodynamic block, and its initial parameters

The model of the horizontal-axis variable-speed WT of 2 MW nominal power and its parameters are introduced in this section. The modelling is performed in Matlab Simulink. The model contains the turbulent wind generation block, the aerodynamic and mechanics block, and the generator torque and blade pitch angle control blocks, as shown in Figure 4.3.

In the turbulent wind generation block, a set of constant wind speeds from 3.5 to 15 m/s are used as an input. The output turbulent wind is generated taking into account the site-specific TI levels, as shown in Figure 2.5.

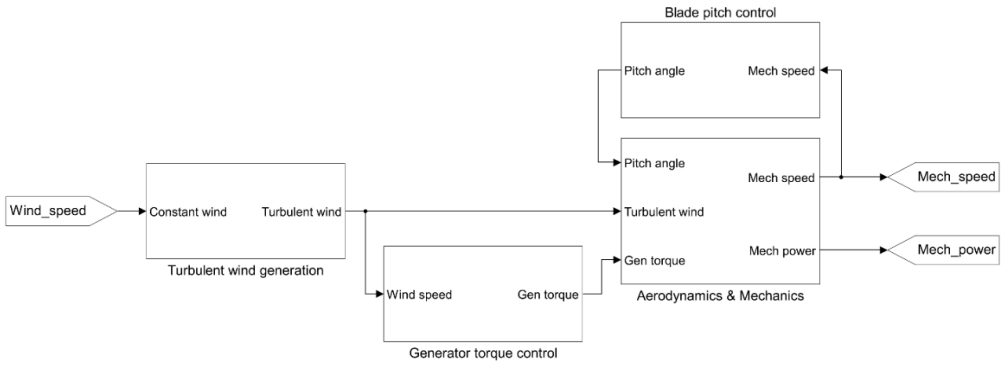

Figure 4.3: Block diagram of the wind turbine system for mechanical and rotor power generation at turbulent wind speeds

The content of the aerodynamics and mechanics block is presented in Figure 4.4. The aerodynamic block calculates the aerodynamic torque based on the input wind speed, and the mechanical speed and blade pitch angle based on Equation (2.18). The block is taken from the Matlab Renewable Energy/Wind Generation Library (MathWorks, 2016). Next, the difference in the aerodynamic and generator torques is divided by the system inertia and integrated in order to obtain the mechanical speed (Equation 2.17).

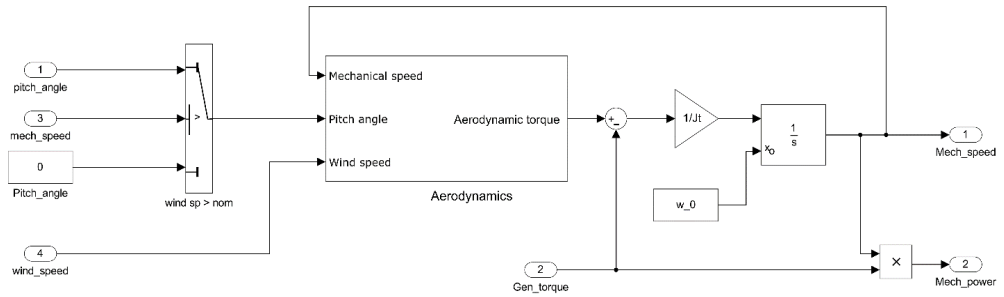

Figure 4.4: Aerodynamic and mechanics subsystem of the WT model.

The generator torque and blade pitch angle control signals are applied as inputs to regulate the rotational speed in four operating modes, as discussed in Section 2.2.4. In Table 4.1, the parameters of the WT aerodynamic and mechanical subsystems are given. The calculation of the model parameters is presented in detail in Appendices B and C.

Table 4.1: Parameters for the wind turbine aerodynamic and mechanical subsystems.

Parameter	Value
Nominal power	2.04 MW

Radius of the rotor wheel	41.7 m
Turbine moment of inertia	4.6e6 kg·m^2
Nominal wind speed	11.5 m/s
Cut-in wind speed	3.5 m/s
Cut-out wind speed	25 m/s
Maximum power coefficient	0.48
Optimal tip speed ratio	8.1
Minimum rotational speed	1.1 rad/s
Maximum rotational speed	1.73 rad/s
Synchronous frequency	50 Hz
Gear box ratio	100
Number of pole pairs of the generator	2

According to the parameters of the Matlab aerodynamic block, the maximum power coefficient $C_{\mathrm{p\_max}} = 0.48$ is reached at the optimal tip speed ratio $\lambda_{\mathrm{opt}} = 8.1$ and the 0° blade pitch angle. The maximum and minimum rotational speeds are defined based on the operating range of the generator slip. As discussed in Chapter 3, the slip is limited from -0.1 to 0.3, which corresponds to 1.73 and 1.1 rad/s. The wind turbine nominal wind speed and the turbine moment of inertia are calculated in Appendices B and C.

The control scheme for the blade pitch angle keeps the rotational speed at the rated value at wind speeds above the nominal wind speed. The PID controller parameters are presented in Table 4.2 (Poore & Lettenmaier, 2003). The blade pitch angle control scheme is shown in Figure 2.13.

Table 4.2: Parameters for blade pitch angle control.

Parameter	Value
Proportional gain	23.2 °/rpm
Integral gain	2.5 °/rpm
Derivative gain	-0.036 °/rpm/s
Time constant	0.02 s
Anti-windup	0.30 rpm/°

4.2.2 **Lifetime estimation model and its initial parameters**

The IGBT lifetime estimation model includes the block diagram to compile the IGBT junction and case temperature profiles, and the block diagram with the lifetime data obtained from the manufacturer's load cycling capability tests. In order to derive the IGBT temperatures, input RSC power and $P_{\mathrm{conv}}/P_{\mathrm{loss}}/T_{\mathrm{j}}$ look-up tables are used (Figure 4.5).

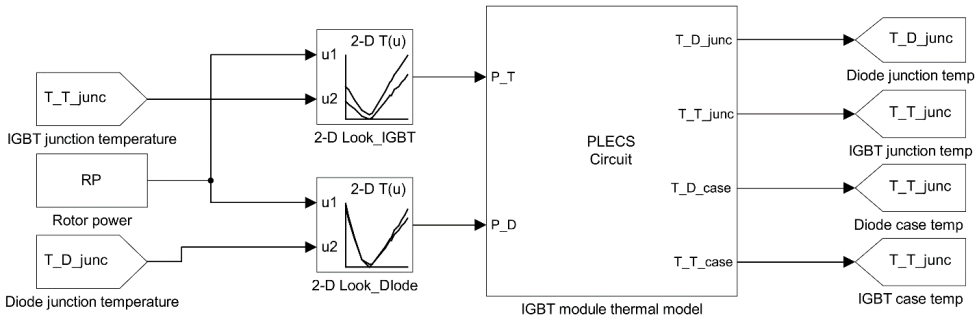

Figure 4.5: IGBT and diode temperatures generation model based on the input rotor power.

The thermal network is modelled in the Matlab PLECS software, where a four-layer Cauer thermal model (Figure 4.6) is implemented (Cauer et al., 2000). The thermal network represents the IGBT module placed on the forced-air cooled heat sink, and the ambient temperature is assumed to be 40 ˚C.

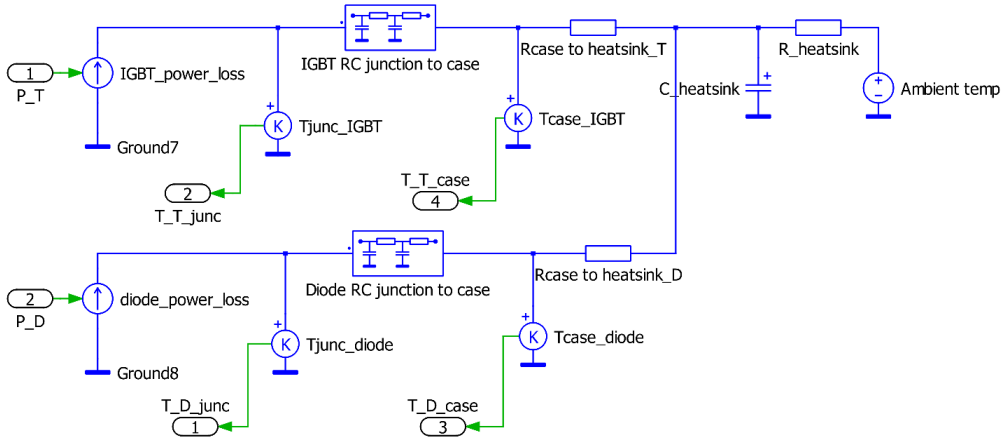

Figure 4.6: IGBT and diode temperature generation model based on the input power losses.

The number of temperature cycles, mean values, and cycle amplitude are calculated by the rainflow counting method using the MATLAB ‘rainflow’ function. The lifetime models provided by the manufacturer (ABB, 2014a) are transferred into the look-up tables (Figure 4.7). As mentioned above, the lifetime data in (ABB, 2014a) in terms of B10 lifetime are given for the chip, conductor lead, and baseplate solder joint fatigues, and the bond wires. The data are presented both numerically and graphically for different cycle periods, temperature amplitudes, minimum and maximum values. The model in Figure

4.7 calculates the three-hour consumed B10 lifetime of the chip solder joints and the bond wires.

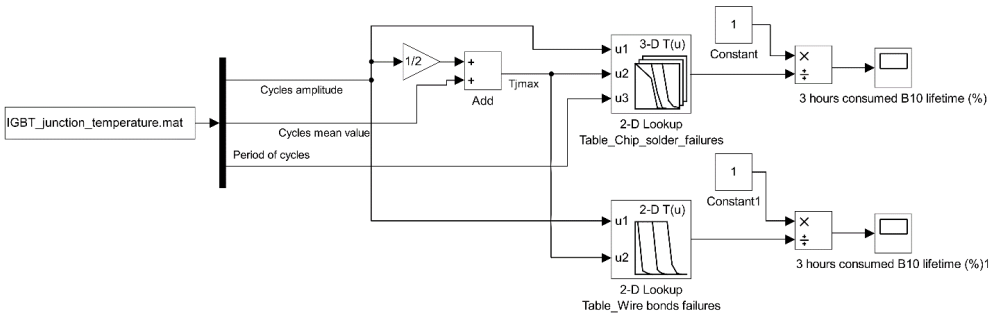

Figure 4.7: Lifetime estimation model based on the rainflow counting method results for the chip solder joints and bond wire fatigue.

4.3 Non-stationary wind speed generation using von Karman's turbulence model

4.3.1 Von Karman's turbulence model

The turbulent wind can be represented as superposition of the sines and cosines of various frequencies and amplitudes. Usually, in order to explicitly represent the signal as a function of frequency and amplitude, the term 'power spectral density' is used (Manwell et al., 2009).

The studies in (Manwell et al., 2009), (Munteanu et al., 2008), and (Nichita et al., 2002) typically focus on three basic power spectral density functions, such as Van der Hoven's, Kaimal's, and von Karman's spectrum models. Van der Hoven's spectrum model covers wind fluctuations in a wide frequency range over a time scale of seconds to days for a period more than decade. Thus, Van der Hoven's model splits the wind speed dynamics into low-frequency fluctuations, associated with synoptic-scale changes and high-frequency fluctuations caused by the turbulence. This statement yields

$$v(t) = v_{\mathrm{m}}(t) + v_{\mathrm{t}}(t), \tag{4.1}$$

where $v_{\mathrm{m}}(t)$ describes the low-frequency dynamics, and $v_{\mathrm{t}}(t)$ is the high-frequency turbulent component.

Kaimal's and von Karman's spectrum models are used to represent only the turbulent wind dynamics. However, Kaimal's and von Karman's power spectral functions apply

the TI dependence on the wind speed, while the amplitude of the turbulence component, synthesized by the Van der Hoven model, remains constant with varying wind speeds.

In the present research, von Karman's spectral density model is used as it is widely applied to synthesize turbulent wind and can be used in real-time WT simulation models. Von Karman's model, discussed in (Nichita et al., 2002), is a turbulent wind simulation model where the white noise is used as an input signal and a 5/6-order shaping filter is applied to characterize the non-stationary turbulent component, which depends on the low-frequency wind speed. The non-rationality in the filter can cause a long computational time. In order to obtain the rationality by eliminating the power of 5/6, the shaping filter H_{F} can be approximated by the following form (Nichita et al., 2002)

$$H_{\mathrm{F}}(s) = K_{\mathrm{F}} \frac{m_1 T_{\mathrm{F}} s + 1}{(m_2 T_{\mathrm{F}} s + 1)(T_{\mathrm{F}} s + 1)}, \tag{4.2}$$

where m_1 and $m_2$are the approximation coefficients for the non-rational filter.

The time constant T_{F} is a function of the low-frequency wind speed v_{m} and the turbulence length *L*

$$T_{\mathrm{F}} = \frac{L}{v_{\mathrm{m}}}. \tag{4.3}$$

The turbulence length *L* can be defined according to the height above the ground *z* (Munteanu et al., 2008)

$$L = \begin{cases} 5 \cdot z \ m, & z < 30\ m \\ 150\ m, & z \geq 30\ m \end{cases}. \tag{4.4}$$

The static gain is

$$K_{\mathrm{F}} = \sqrt{\frac{2\pi}{B(1/2, 1/3)} \cdot \frac{T_{\mathrm{F}}}{T_{\mathrm{s}}}}, \tag{4.5}$$

where *B* is the beta function, and T_{s} is the sampling time of the white noise.

Thus, the wind generating model, which combines the low-frequency wind dynamics and turbulent wind based von Karman's spectral density can be derived (Figure 4.8).

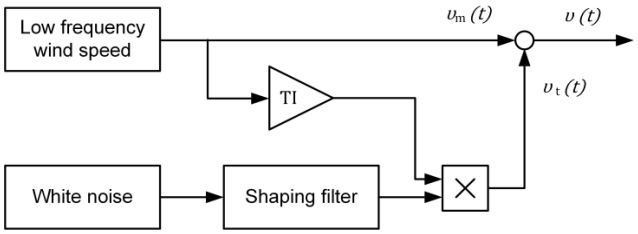

Figure 4.8: Generation of the turbulent wind speed using von Karman's spectral density function.

4.3.2 **Calculation of von Karman's model parameters**

The turbulence component of the model in Figure 4.8 includes the site-specific parameters, such as the TI and the integral time scale T_F. The 10 min and 1 s wind speed data from 1 June 2014 to 31 May 2015, measured in South-Eastern Finland, are used. The wind speed has been measured by the LIDAR sensor.

The TI was defined based on the 10 min wind speed averages and the corresponding standard deviation, as shown by Equation 2.3. Since the TI is a function of wind speed (Figure 2.5), the model assumes a varying TI depending on the value of the low-frequency wind speed (Table 4.3). The sampling time T_s is 1 s, which is a reasonable time scale to present the turbulence component (Nichita et al., 2002).

Table 4.3: Turbulence intensity versus wind speed.

Wind speed (m/s)	Turbulence intensity	Time constant, T_F (s)	Static gain, K_F
1	0.359	150	14.97
2	0.261	75	10.58
3	0.207	50	8.64
4	0.170	37.50	7.48
5	0.146	30	6.69
6	0.140	25	6.11
7	0.148	21.43	5.66
8	0.158	18.75	5.29
9	0.164	16.67	4.99
10	0.167	15	4.73
11	0.169	13.64	4.51
12	0.174	12.50	4.32
13	0.184	11.54	4.15
14	0.181	10.71	4
15	0.183	10	3.86

According to Equation 4.4, the integral length scale L_F is 150 m. The time constant T_F and the transfer function gain K_F vary with the varying mean wind speeds (Equations 4.3, 4.5), as shown in Table 4.3.

The approximation parameters of the shaping filter m_1 and m_2 (Equation 4.2) are selected in order to obtain similar power spectral density characteristics of the measured and modelled wind speeds. The matched parameters $m_1 = 0.4$ and $m_2 = 0.25$ are well fitted, as can be seen in Figure 4.9 and Figure 4.10.

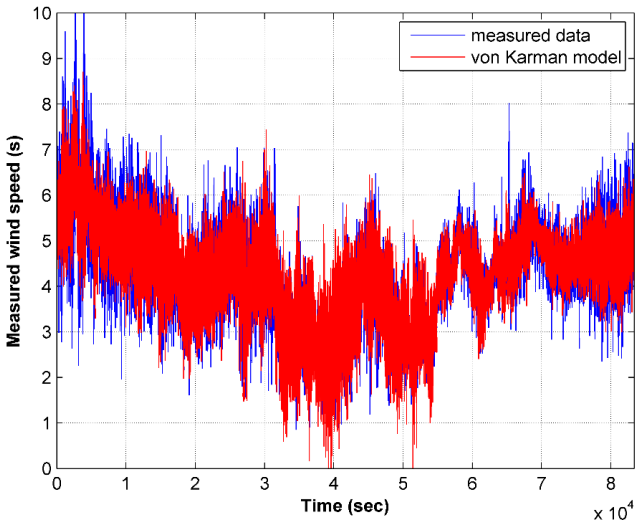

Figure 4.9: Example of the 1 s sampled data: measured (blue) and modelled (red) wind speeds.

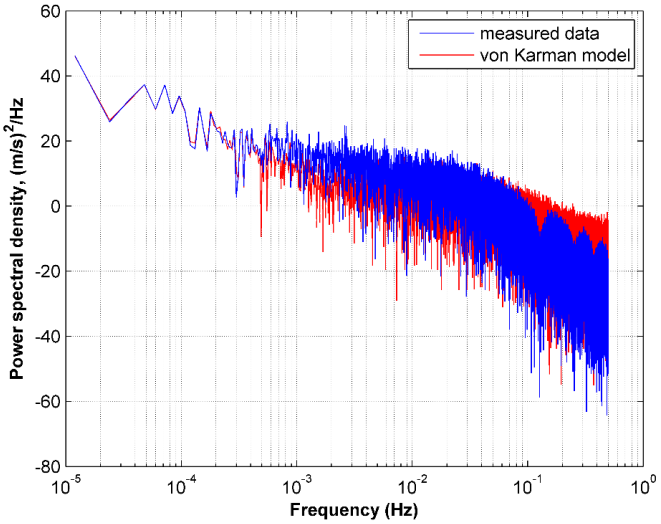

Figure 4.10: Power spectral density of the measured (blue) and modelled (red) wind speeds.

The gain characteristics of the shaping filter H_F at 6 and 11.5 m/s are shown in Figure 4.11.

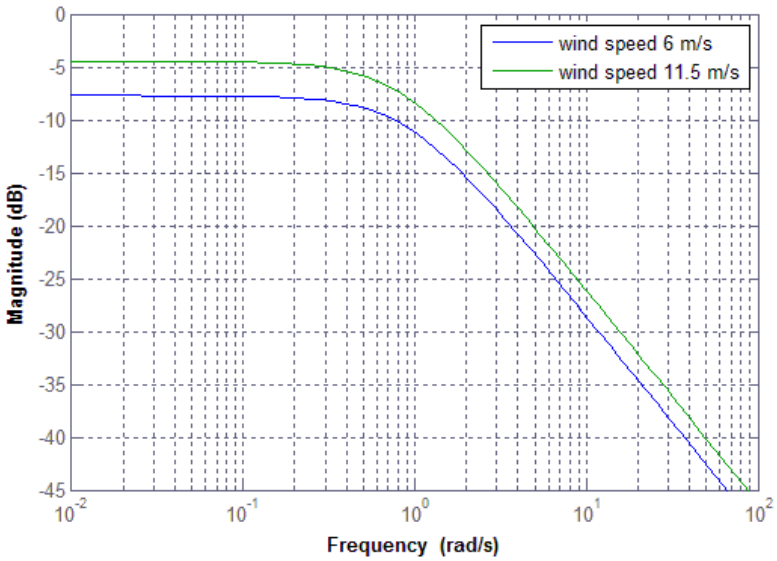

Figure 4.11: Bode plots of the shaping filter H_F at 6 m/s (blue) and 11.5 m/s (green) wind speeds.

As mentioned above, the wind data sample frequency is 1 Hz, and thus, the wind speed variations below 1 Hz are not considered. It is pointed out that the shaping filter reduces the white noise amplitudes over the whole frequency range. Because the filter parameters T_{F} and K_{F} vary with the wind speed, the Bode plots at 6 and 11.5 m/s are shifted (Figure 4.11).

4.4 Wind turbine dynamic response

According to Figure 2.9, the dynamic performance of the WT is divided into four operating modes. In Figure 4.12, basic aerodynamic parameters, the tip-speed ratio and the power coefficient, are presented. Obviously, the parameters have their optimal values in mode 2, where the generator torque is controlled to be proportional to the rotational speed squared. In modes 1, 3, and 4, the power coefficient C_{p} is below its optimal value because of the rotational speed limitations. The tip-speed ratio is higher than the optimal value in mode 1, and lower in modes 3 and 4.

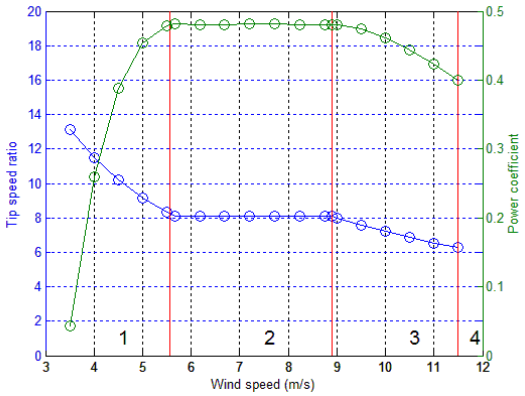

Figure 4.12: Tip speed ratio and power coefficient in four operating modes of the DFIG.

Figure 4.13 illustrates the wind turbine mechanical and rotor-side converter power curves, and the rotation speed and slip are presented. In Table 4.4, the corresponding numerical data are shown. Simulations are performed using the model in Figure 4.3. Both the linearly increasing and different steady-state wind speeds from 3 to 15 m/s are applied as inputs.

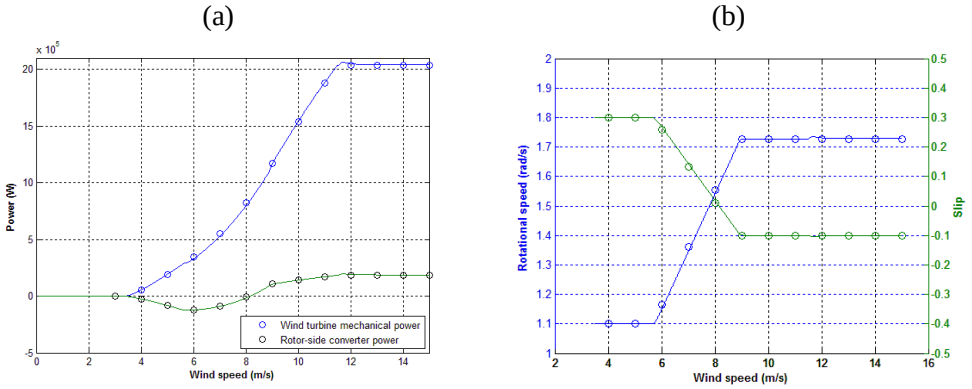

Figure 4.13: Wind turbine operation at linearly changing wind speeds (line) and in steady states (circles). (a) Mechanical and rotor-side converter power. (b) Rotational speed and slip.

Table 4.4: WT model simulation results in steady states.

Wind speed (m/s)	Rotational speed (rad/s)	Slip	Mechanical power (MW)	RSC power (kW)
4	1.10	0.30	0.056	-24.883
5	1.10	0.30	0.190	-81.356
6	1.17	0.26	0.347	-120.517
7	1.36	0.13	0.551	-85.475
8	1.55	0.01	0.822	-8.921
8.1	1.57	0	0.826	0
9	1.73	-0.10	1.170	106.179
10	1.73	-0.10	1.541	139.883
11	1.73	-0.10	1.881	170.638
11.5	1.73	-0.10	2.036	185.483
12	1.73	-0.10	2.036	185.483
13	1.73	-0.10	2.037	185.483
14	1.73	-0.10	2.037	185.483
15	1.73	-0.10	2.037	185.483

At wind speeds 4–8.1 m/s, the rotor-side converter power operates as an inverter. The converter power flow from the WT to the grid is assumed positive, and thus, the converter power in this wind speed range is negative (Table 4.4). Zero slip operation is reached at the rotational speed of 1.57 rad/s and the wind speed of 8.1 m/s.

In Figure 4.14, the turbulent wind and the WT mechanical and converter power are simulated for a period of three hours at mean wind speeds of 6 and 11.5 m/s.

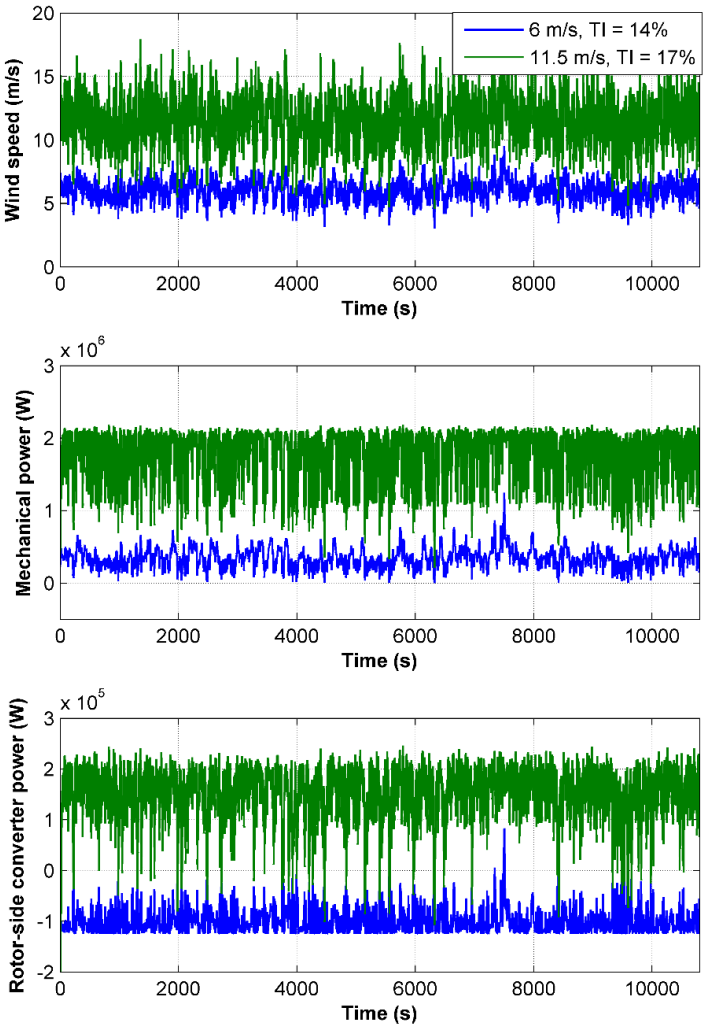

Figure 4.14: Turbulent wind speed fluctuations and the corresponding WT mechanical converter power at 4, 6, 8, and 11.5 m/s mean wind speeds.

4.5 Power loss look-up tables

The look-up tables are calculated to derive the dependence of the IGBT and diode power losses on the converter power and the junction temperature. The IGBT power losses include the switching and conduction losses of the IGBT and the diode. The junction temperature has been set at 25 and 125 °C as an input to the thermal description of the model. Thus, after obtaining the calculated power losses for 25 and 125 °C, the interpolation method can be used to define the losses at varying junction temperatures

(Figure 4.15). It is pointed out that the "double-layer" effect of the power map is due to the fact that the rotor power curve starts to decrease from zero to a negative value at 3 m/s, and then, at 6 m/s it increases back to zero, as can be seen in Figure 4.13. Thereby, the rotor power curve intersects the zero twice.

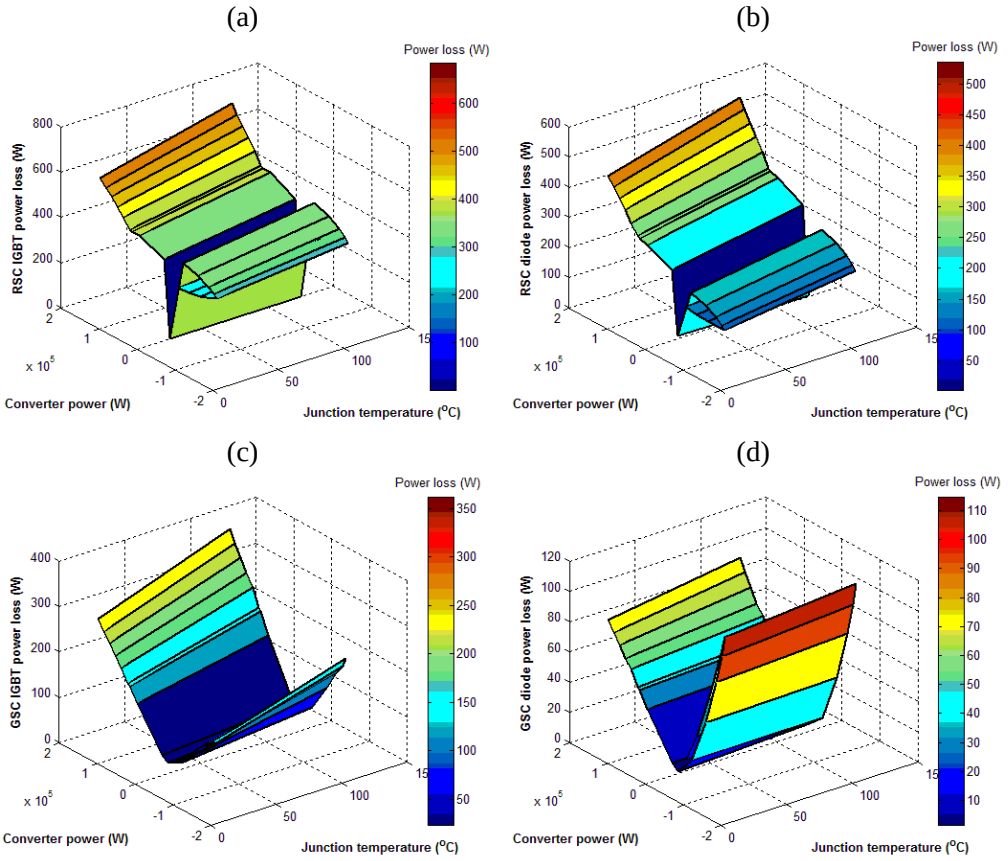

Figure 4.15: Look-up tables for the power losses of the IGBT of the back-to-back power converter in the DFIG.

The negative converter power indicates power flow from the grid to the generator rotor. Converter power variations at turbulent wind speeds are applied as an input to the obtained look-up tables. The resultant power loss variations and the IGBT and diode thermal models are used to derive the junction temperatures, which are further applied for the lifetime estimation.

4.6 Rainflow cycle counting method

The rainflow counting algorithm is a widely used method applied in the material fatigue analysis (Socie & Marquis, 1999), (Nieslony, 2009). The arbitrarily changing junction temperature fluctuations are analysed in terms of mean value, temperature swings, and period of each counted cycle.

The method is explained by the following algorithm applied to the example arbitrary signal (Figure 4.16) (Irvine, 2011) (Wægter, 2009)

1. Rotate the plot 90° clockwise, so that the time axis corresponds to an ordinate axis.
2. The rainflow starts at each peak.
3. Imagine a water drop sliding down from the top of each peak along the slope.
4. The cycle is finished if the drop falls when the opposite peak has a higher amplitude than the peak where the flow has started from, or if the cycle is part of a longer cycle.
5. Calculate the amplitude of each cycle, and combine cycles with the same amplitudes in pairs. Residual cycles can be omitted. Count the number of pairs; each pair is considered as one cycle.

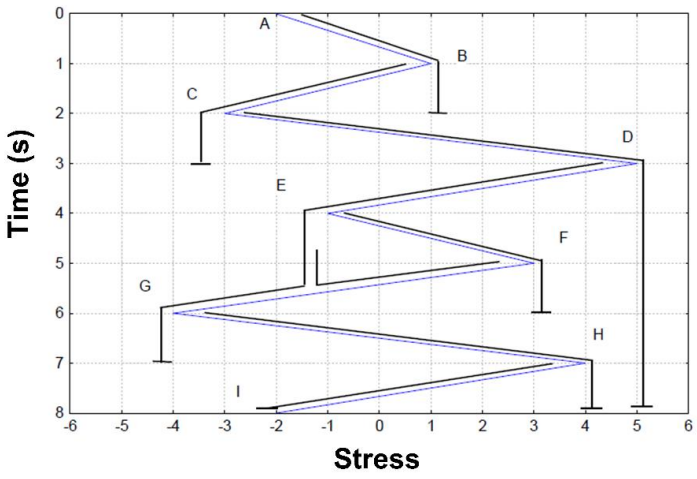

Figure 4.16: Example of the rainflow counting method applied to an arbitrary signal (Irvine, 2011).

The counted cycles from Figure 4.16 with the corresponding path are presented in Table 4.5.

Table 4.5: Example of the counted cycles using the rainflow method (Irvine, 2011).

Path	Cycles	Stress amplitude
A–B	0.5	3
B–C	0.5	4
C–D	0.5	8
D–G	0.5	9
E–F	1	4
G–H	0.5	8
H–I	0.5	6

Obviously, the cycles C–D and G–H have the same amplitude equal to 8. Thereby, these cycles can be paired up and considered as one complete cycle. The cycle E–F is considered as one complete cycle, because it contains some part of F–G.

Thus, as mentioned above, the junction temperature fluctuations are generated by applying the IGBT and diode power losses, varying under turbulent wind speed. In Figure 4.17, the temperature fluctuations, mean values, and periods of cycles, calculated by the rainflow counting method, are shown.

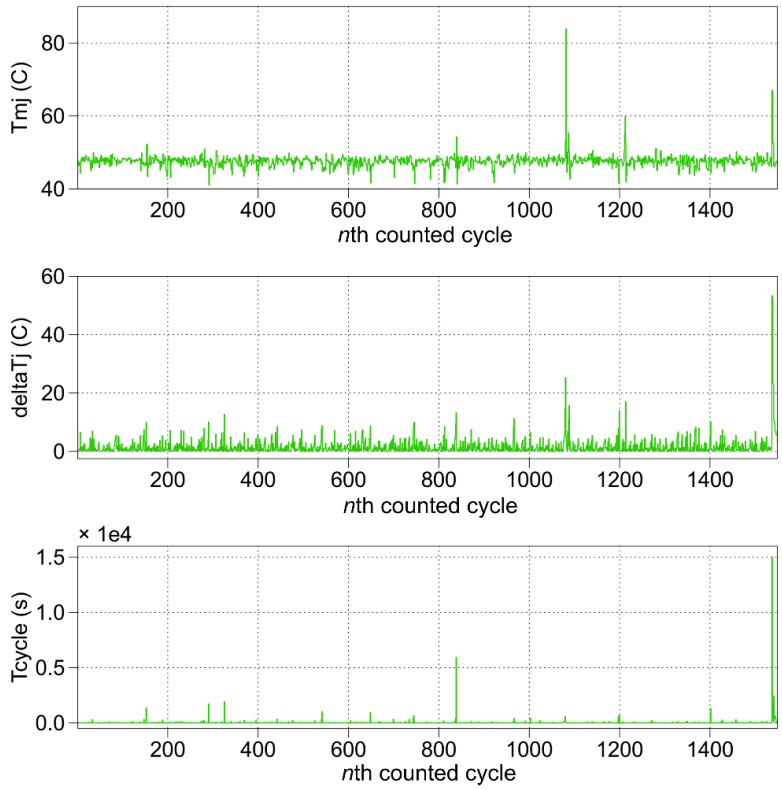

Figure 4.17: Results of the rainflow counting algorithm applied to the junction temperature variations.

4.7 B10 lifetime estimation

The IGBT lifetime model, provided by the manufacturer, identifies the number of thermal cycles N_{B10} that lead to the IGBT B10 failure rate for each *n*th cycle, obtained by the rainflow counting method. As an example, the lifetime data of the bond wires as a function of maximum junction temperature and cycle period are shown in Figure 4.18.

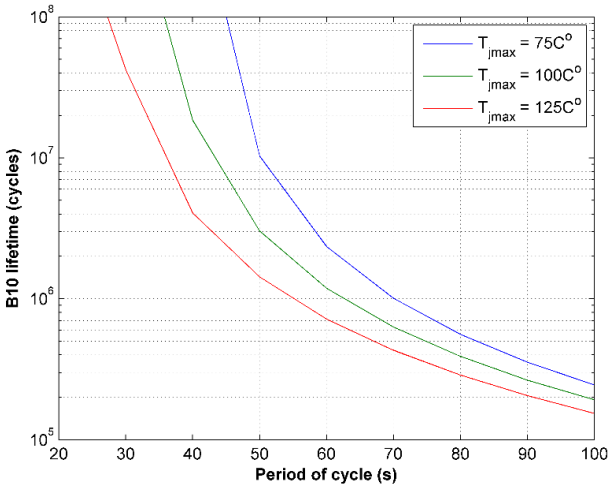

Figure 4.18: Lifetime model provided by the manufacturer (ABB, 2014a) (redrawn in MATLAB based on the numerical data given by the manufacturer).

In other words, each *n*th counted temperature cycle has a corresponding number of cycles N_{B10} with a 10 % failure probability of the IGBT. For instance, as can be seen in Figure 4.18, the *n*th cycle with a period of 55 s and a maximum value of 125°C has $N_{B10,n}$ 10^6 cycles.

Thus, the consumed lifetime CL_n of the IGBT with the 10 % probability can be calculated as

$$CL_n = \frac{1}{N_{B10,n}} \cdot 100\%. \tag{4.21}$$

After running the model in Figure 4.7, the three-hour profile for the consumed lifetime at turbulent wind speed with a specific mean value is obtained. In other words, the result of the simulation is a set of CL_n values. Consequently, the total three-hour consumed lifetime is

$$CL_{3\,h} = \sum_{n=1}^{N} CL_n, \tag{4.22}$$

where *N* is the total number of cycles over three hours.

According to Miner's rule, the total consumed lifetime for a one-year period is a sum of the calculated lifetimes for each specific wind speed,

$$CL_{year} = \frac{365 \cdot 24}{3} \cdot (W_{4\,m/s} \cdot CL_{4\,m/s\,3h} + W_{5m/s} \cdot CL_{5m/s\,3h} + \cdots W_{15m/s} \cdot CL_{15m/s\,3h}), \quad (4.23)$$

where $W_{\_m/s}$ is the wind speed probability at a specific wind speed.

In Figure 4.19 and Figure 4.20, the lifetime consumption of the IGBT modules over the wind speed range, taking into account the site-specific wind speed distribution, is shown.

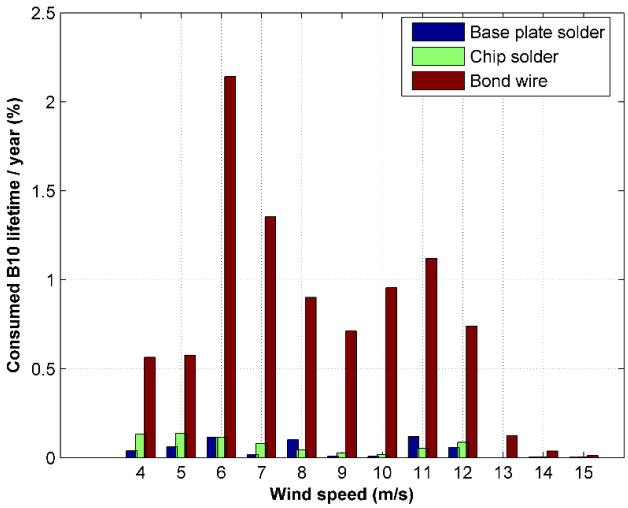

Figure 4.19: Consumed B10 lifetime distribution over the operation wind speed range at the RSC.

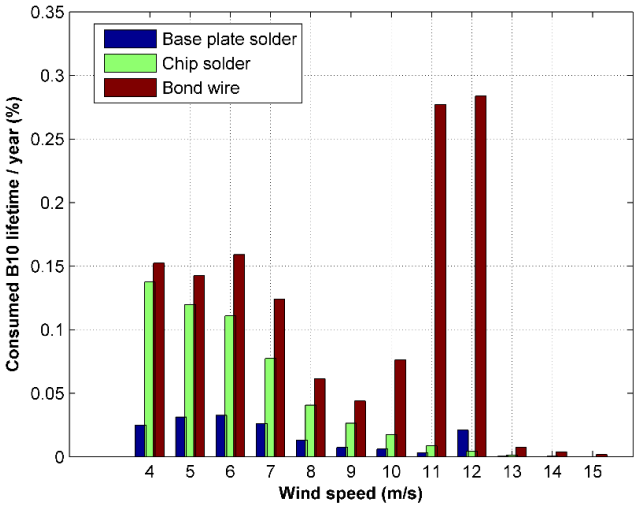

Figure 4.20: Consumed B10 lifetime distribution over the operation wind speed range at the GSC.

Obviously, the lifetime-consuming cycles have a significant effect on the bond wires compared with the solder fatigue. In the case of the base plate solder, the consumed lifetime is calculated based on the chip temperature. Thus, owing to the IGBT module thermal impedance, the thermal cycles have a less significant effect on the degradation.

It can be concluded that the lifetime distribution is affected by the wind distribution characteristics (Figure 2.4), the turbulent wind speed dynamics, the junction temperature mean value, and the amplitude of the temperature changes associated with the DFIG operation, and the corresponding converter power losses. Because the zero slip operating point is characterized by the local maximum in the IGBT junction temperature, it is reasonable to predict the critical lifetime consumption of the RSC at this point. However, the lifetime consumption maximum is at 6 m/s. The reason for this phenomenon is the highest probability of the wind speed to be within this range, as shown in the wind speed probability distribution function in Figure 2.4. The GRC thermal loading is not affected by the rotor fundamental frequency, and the junction temperature swings are more uniformly distributed over the increasing wind speed. Therefore, the lifetime consumption at the GSC is affected by the operating current and the corresponding power losses. However, here a similar effect of the wind speed distribution takes place.

In Figure 4.21, the total one-year consumed lifetime at the RSC and the GSC is shown.

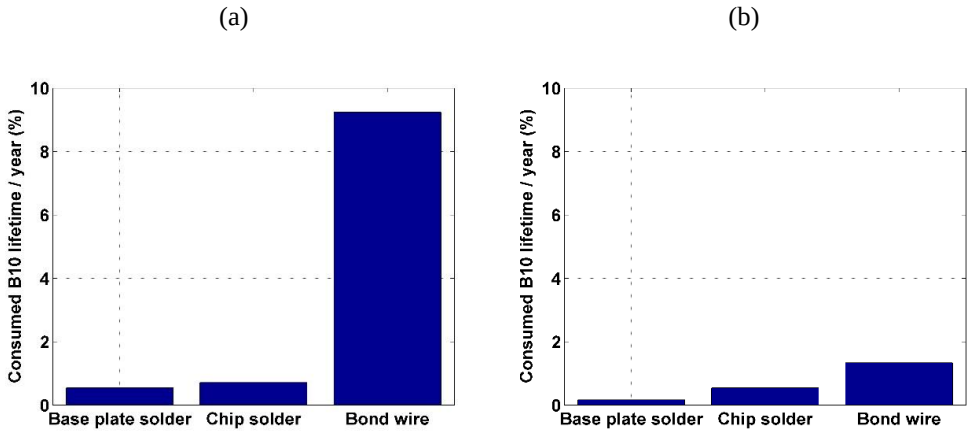

Figure 4.21: One-year consumed lifetime of the IGBT module. (a) In the RSC. (b) In the GSC.

The estimation of the B10 lifetime has shown that the RSC is more probably subjected to failure than the GSC. In both cases, the bond wire fatigue is the dominant failure mechanism, whereas the base plate solder is less subjected to failure.

4.8 Summary

Chapter 4 presented an IGBT lifetime estimation model, which combines the WT dynamics associated with the turbulent wind speed, operation of the DFIG and the most critical failure mechanisms, such as the bond wire lift-off and the base plate and chip solder fatigue.

The developed wind speed generation model and the selected parameters of the shaping filter are considered to be an excellent tool to simulate the site-specific turbulent wind. The simulation results were compared with the wind speed data collected for one year in South-Eastern Finland using a LIDAR sensor. Both wind speed sets have similar PSD characteristics, and thus, the implemented model can be applied to generate the wind speed for another sites, assuming that the site-specific parameters, such as TI, turbulent length scale, and average wind speed are defined in advance.

The generated wind speed was applied to the WT mechanical model to derive the mechanical power and the corresponding power of the rotor, based on the calculated slip. The DFIG-specific operating modes, described in Chapter 3, were taken into account. In order to transfer the rotor power into the thermal loading of the RCS and the GSC, the power loss look-up tables were used. The look-up tables comprise the power losses of the IGBT and the diode of the DFIG power converter at different wind speeds.

The obtained power losses and a Cauer-type thermal model of the IGBT and the diode were used to derive the IGBT junction temperature. Based on the counted number of cycles of the junction temperature and the lifetime models, provided by the manufacturer, the lifetime consumption was defined. It can be concluded that both the RSC and the GSC consumed lifetimes are strongly affected by the wind speed distribution characteristics as the corresponding thermal loading has a similar effect. However, because the thermal cycles in the RCS are strongly affected by the rotor fundamental frequency, the lifetime consumption is higher in the medium wind speed range than at the rated wind speed. In the GSC, the fundamental frequency is constant, and thus, the highest lifetime consumption is at the rated wind speed.

5 Gradient heat flux sensor application in power electronics

In this chapter, the GHFS is applied to measure the thermal stress of the IGBT module. The GHFS with a relatively simple design is a preferable choice to the temperature-sensor-based HFS, where the heat estimation is based on multiple thermocouples or RTDs mounted on the thermal resistance layer. The GHFS operation represents direct heat flux measurement, whereas the aforementioned sensors estimate the heat flux by temperature sensors and additional processing of the temperature data. The GHFS provides an opportunity to detect possible degradation, and it can be used in the CM system. The heat flux measurements are compared with the expected power losses in the normally operating and the degraded IGBT. In the latter case, the IGBT modules with a broken bond wire and degraded thermal grease are considered.

5.1 Gradient heat flux sensor technology

As mentioned above, the thermo-EMF is induced in the direction normal to the heat flow of the sensor. Thus, the thermo-EMF E_{th} does not depend on the sensor thickness, as it is a function of the area A_{sensor}

$$E_{\mathrm{th}} = qA_{\mathrm{sensor}}S_0, \tag{5.1}$$

where q is the heat flux density, and S_0 is the volt-watt HFS sensitivity.

The sensitivity has been tested in the calibration test using the methods described in (Sapozhnikov et al., 2012), where the variation of the sensitivity does not exceed 3 %.

The structure of the GHFS is presented in Figure 5.1. It consists of several bismuth plates with a 0.1–0.2 mm width, isolated from one another by a Mylar spacer. The sensor is soldered onto the mica base for the electrical isolation. The output terminals are attached at the marginal bismuth plates.

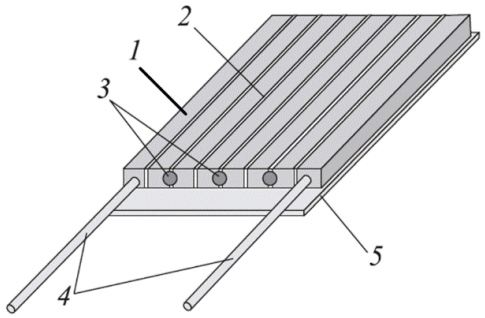

Figure 5.1: Structure of the gradient heat flux sensor; 1: single plate of bismuth, 2:insulation, 3: solder, 4: output terminals, 5: mica base (Mityakov et al., 2012).

The specifications of the GHFS used in the study are presented in Table 5.1.

Table 5.1: Specifications of the GHFS.

Parameter	Value
Volt-watt sensitivity	15.9 mV/W
Thickness	0.1mm
Area	0.85 cm^2
Response time	10^{-9} – 10^{-8} s
Thermal conductivity of bismuth	7.45 W/(m·K)
Operating temperatures	-20…544 K

It should be noted that the GHFS is attached to the IGBT base plate, and thus, the power losses dissipated in the chip and passing through the multi-layered module structure are attenuated by the thermal impedance. Therefore, regardless of the fast time response of the sensor, the bandwidth of the measured heat flux dynamics is limited, and the IGBT high-frequency switching cannot be observed.

5.2 Heat flux modelling of the normally operating IGBT module

Before investigating the real heat flux behaviour in the IGBT module, it is reasonable to model the temperature and heat flux density distribution over the IGBT base plate using a FEM model in the Comsol Multiphysics software. The FEM modelling was performed by the research team member and co-author in (Baygildina et al., 2016a).

The basic principle applied in the FEM model is that the temperature and the heat flux behaviour, described mathematically by partial differential equations (PDEs), is approximated by means of discretization with numerical model equations (COMSOL,

2015). In this context, the temperature and heat, varying in time and space, are presented as a combination of linear functions or elements for the boundary layer mesh. Here, the PDEs are preferred to the ordinary differential equations (ODEs), if the equations include more than one independent variable. The thermal properties and geometrical parameters of the IGBT module are defined in the program in advance.

In the FEM model, presented in this study, the mesh of the FEM model has 920407 tetrahedral elements and the run time is 120 s. A cross-section of the IGBT module designed in Comsol Multiphysics is shown in Figure 5.2 (Baygildina et al., 2016a).

.

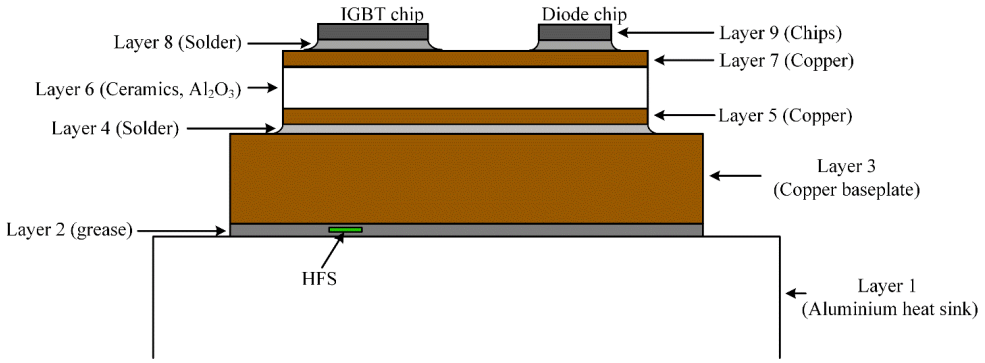

Figure 5.2: Cross-section of the IGBT model used in the Comsol Multiphysics software (Baygildina et al., 2016a).

The thicknesses of the layers and the thermal conductivities in Figure 5.2 are presented in Table 5.2.

Table 5.2: Properties of the materials in the model.

Layer	Material	Thickness, mm	Thermal Conductivity, W/(m·K)
1	aluminium	120	205
2	thermal grease	1	1
3	copper	3	400
4	solder	0.08	50
5	copper	0.15	400
6	Al_2O_3	0.42	27
7	copper	0.15	400
8	solder	0.08	50
9	silicon	0.22	130

The IGBT module is placed in the air-cooled heat sink with a convective coefficient of 5 W/(m^2·K). The ambient temperature is 25 °C. The total power generated in four chips is

13.2 W. It is pointed out that the model assumes a vertical heat flow from the heat sources (chips) to the heat sink, in other words, the heat dissipation through the rim of the base plate is not considered. The forced conduction of heat in the vertical direction and the larger area of the base plate on the bottom side than the edge area make the latter assumption relevant. Moreover, the FEM modelling of the heat flux has shown that only 2 % of the heat dissipates through the sides of the IGBT module. Thus, it is reasonable to place the sensor on the bottom side of the base plate.

As shown in Figure 5.2, the GHFS is placed within the thermal grease (layer 2) at the base plate under the chip. The thickness of the thermal grease layer is 1 mm, which is considered to be quite thick; the thickness is explained by the attachment of the thermocouple to the base plate of the IGBT module in the experimental setup.

The power device used in the FEM modelling and the test setup is an Infineon FZ400R17KE4 IGBT module (Infineon, 2011) with the thermal parameters presented in Table 5.3.

Table 5.3: Thermal impedances of the FZ400R17KE4 IGBT module (Infineon, 2011).

Thermal Impedance	**$Z_{j\text{-}c}$**				**$Z_{c\text{-}h}$**
	Layer 1	**Layer 2**	**Layer 3**	**Layer 4**	
$R_{i\mathrm{IGBT}}$, K/kW	2	9.2	42.6	6.3	18
$\tau_{i\mathrm{IGTB}}$, ms	0.8	13	50	600	–

The Cauer-type thermal model is shown in Figure 5.3. The model includes the thermal impedances of the junction to the case $Z_{\mathrm{j-c}}$, from the case to the heat sink $Z_{\mathrm{c-h}}$, and from the heat sink to the ambient $Z_{\mathrm{h-amb}}$. In Figure 5.3, the location of the heat flux measurements is denoted Q_{meas} and placed between the case and the heat sink.

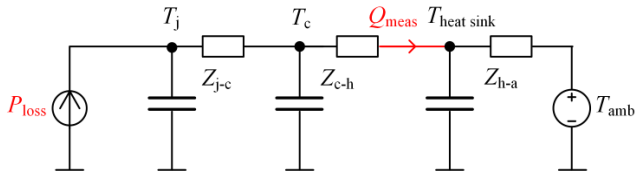

Figure 5.3: Thermal model of IGBT module with heat flux measurements Q_{meas} on the case surface (Baygildina et al., 2016a).

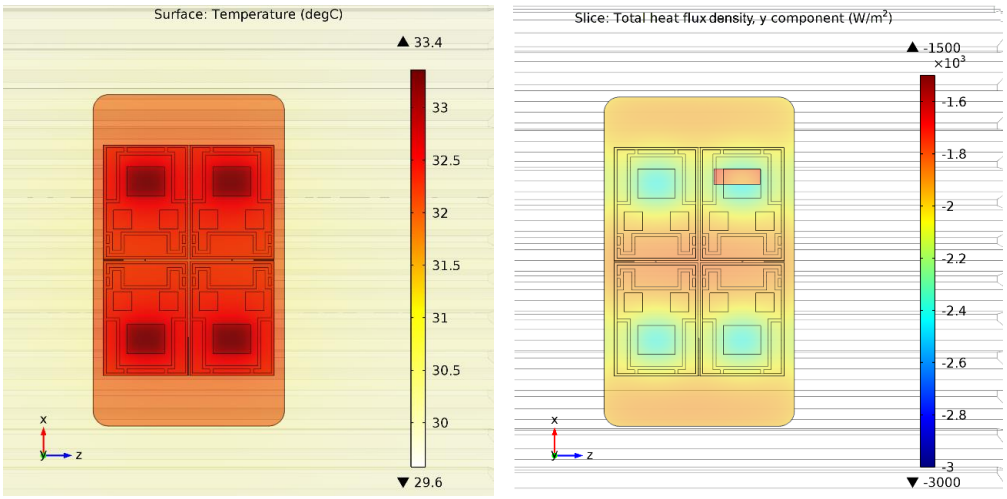

(**a**) (**b**)

Figure 5.4: Top view of the model. (a) Temperature distribution; (b) Heat flux density distribution (Baygildina et al., 2016a).

According to the FEM modelling results, obtained in Figure 5.4, the temperature and heat flux density distribution is non-uniform. The power loss of 13.2 W generated in the chips corresponds to 33.2 °C of the chip temperature and 1870 W/m^2 of the heat flux density dissipated through the GHFS. However, the average heat flux density over the base plate surface is 2025 W/m^2, which is 8 % higher than the heat flux density under the chip. It can be concluded that the GHFS induces heat flux disturbance because of the different thermal conductivities of the sensor and the thermal grease. In order to avoid the heat flux disturbance, the GHFS can be placed between the chips, and the effect of both chips on the heat flux through the sensor can be considered. An alternative way to measure the IGBT heat flux is to implement the GHFS close to the chip, that is, inside the module. However, the low thermal conductivity and the relatively high thickness, compared with the environment, make this solution unacceptable.

5.3 Heat flux in the degraded IGBT module

Four different failure mechanisms, namely solder degradation between the chip and the ceramic substrate, between the base plate and the ceramic substrate, the bond wire lift-off, and the thermal grease degradation are considered in this section, because they are the dominant package-related failures in the IGBT module.

As discussed in Chapter 1, the solder degradation starts from the corners and develops to the centre of the solder layer. Thus, the FEM model assumes 50 % of the solder layer under the chip from the periphery replaced by air with a thermal conductivity of 0.001 W/(m·K) (Figure 5.5). The base plate solder degradation is modelled similarly.

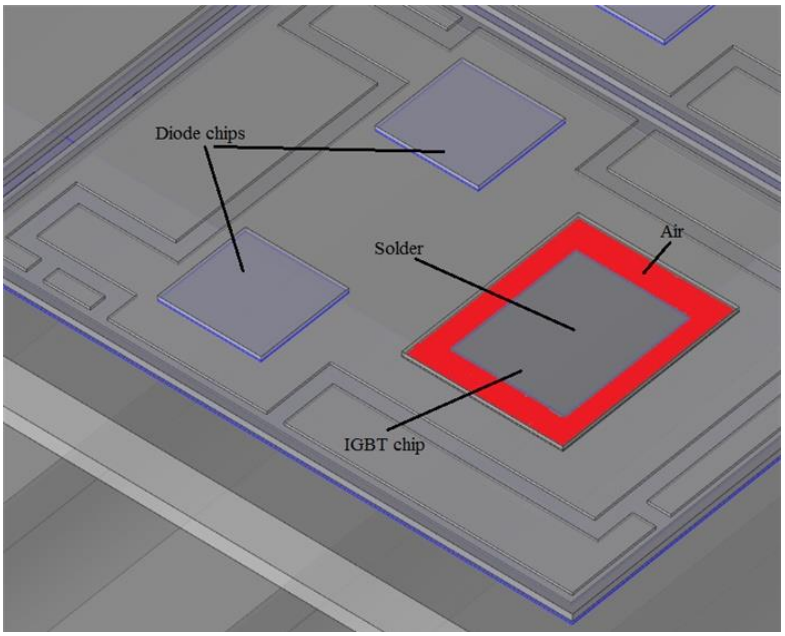

Figure 5.5: Solder layer degradation under the chip modelled in the FEM (Baygildina et al., 2016b).

The bond wire lift-off is modelled by decreasing the active area of the chip by 12.5 %, meaning that one of the eight chips has failed. The latter assumption is based on the uniform heat and temperature distribution over the chip. However, despite the fact that the bond wires conduct the current in parallel, significant non-uniformity of the chip temperature over the chip surface has been detected in the tests performed in (Chen et al., 2012). Here, the temperature maximum is observed in the centre of the chip, and the bond wire failures start at the bond with the highest temperature swing. After the failure of one bond wire, the thermal stress is redistributed among the remaining bond wires. Thus, the heat flux is now generated in the remaining active area of the chip. Because the heat flux is measured on the base plate, the characteristics of the heat flux density distribution over the chip are hardly recognizable as a result of the smoothing effect of the module thermal impedance. In this context, the measured heat flux is related to the average power losses of the chip. It is pointed out that the additional ohmic losses generated by the bonds are ignored in the model owing to the calculation difficulties.

The degradation of the thermal grease is modelled by a 30 % decrease in the thermal conductivity of the layer. The reasons for this decrease could be the pump-out and dry-out of the thermal grease. The first phenomenon is caused by the relative motion in the contacting interface as a result of the cycling power loading of the module (Gowda, 2007). Thus, the thermal grease drifts away from the contact surfaces. The thermal grease dry-out occurs at high temperatures because of the separation of the polymer matrix and the

filler of the compound. This phenomenon leads to a low humidity level in the polymeric material, and thus, drying out of the thermal compound (Viswanath et al., 2000). Unfortunately, it is probably not possible to estimate the exact decrease in the thermal conductivity of the degraded thermal grease. Therefore, to observe the heat flux density deviation, a 30 % decrease in the thermal conductivity (from 1 to 0.7 W/(m·K)) has been selected for trial purposes.

In order to estimate the possible heat flux deviation in the abovementioned degradation cases, an input power of 7 W was applied as a heat source from all four chips in the FEM model. According to the FEM modelling results, the average heat flux density over the base plate is 1075 W/m^2. The heat flux density through the sensor is 1195 W/m^2, which corresponds to a 7.81 W heat flux. In Figure 5.6, the heat flux density over the base plate is shown for the broken bond wire and the thermal grease degradation cases.

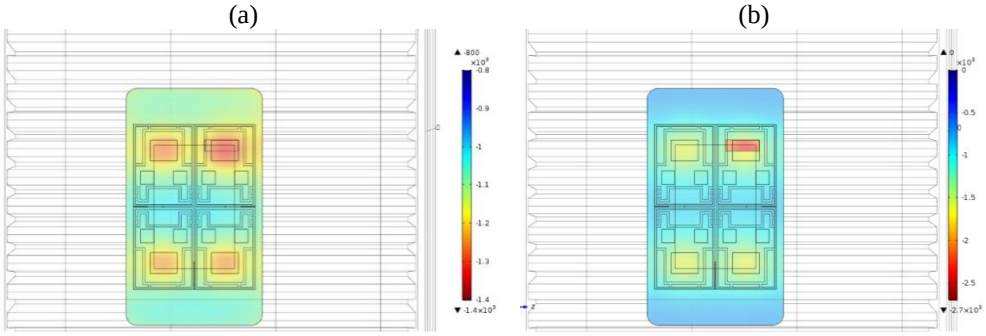

Figure 5.6: Heat flux density distribution over the base plate. (a) Bond wire lift-off. (b) Degraded thermal grease (Baygildina et al., 2016b).

In Table 5.4, a comparison of heat flux densities in four degradation cases is shown.

Table 5.4: Comparison of the heat flux density test results with the FEM modelling results.

Type of degradation	q (W/m^2)	Q_{sensor} (W)	ΔQ (%)
Bond wire lift-off	1277	8.34	6.86
Chip solder fatigue	1198	7.83	0.25
Base plate solder fatigue	1201	7.85	0.5
Grease degradation	2188	14.29	83.0

The heat flux through the sensor is calculated as follows

$$Q_{sensor} = qA_{sensor}. \tag{5.2}$$

The value for the area of the sensor A_{sensor} is given in Table 5.1.

As shown in Figure 5.6, the heat flux density under the chip with the broken bond wire is higher than the normally operating chips. Compared with the normally operating IGBT, the heat flux density through the sensor is increased by 6.86 % (Table 5.4).

The degradation of the thermal grease induces a decrease in the heat flux density over the whole surface of the base plate. However, the heat flux density through the sensor is about two times as high as the base plate averaged. The phenomenon can be explained by the high thermal conductivity of the sensor compared with the degraded thermal grease. Thus, according to Table 5.4, the thermal grease degradation is related to the highest deviation of the heat flux, compared with the properly functioning IGBT module heat flux, which is 83 %.

Negligibly small deviations are observed in the cases of chip and base plate solder fatigue, 0.25 and 0.5 %, respectively.

5.4 IGBT heat flux measurements

The GHFS is attached to the Infineon FZ400R17KE4 IGBT module, as mentioned above. The T-type thermocouple to measure the base plate temperature is also mounted next to the GHFS (Figure 5.7). The sensors are placed on the hottest spots on the base plate surface, located under the chip positions.

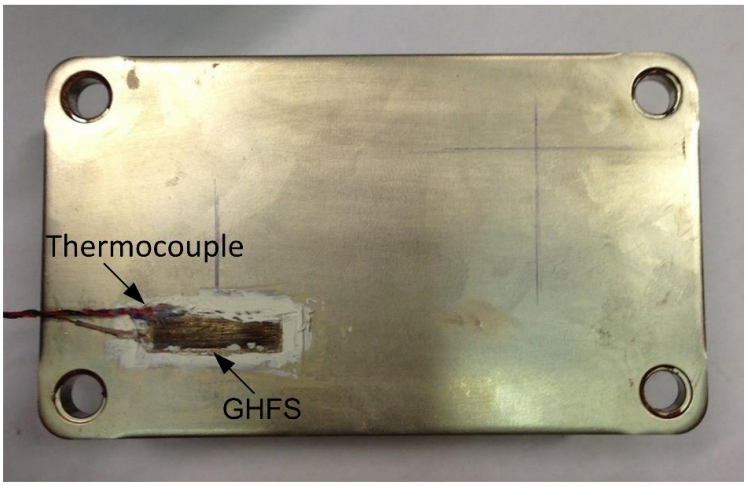

Figure 5.7: Attachment of the sensor to the base plate (Baygildina et al., 2016a).

The gate driver board for the IGBT module has been programmed to provide sinusoidal pulse-width modulation (PWM) with a switching frequency of 1 kHz. The fundamental frequencies are 0.1 and 7 Hz. In the test setup, two parallel IGBT modules are connected to the DC voltage source through a 4.1 mF capacitor bank connected in parallel and a 0.77 Ω load resistor. The parallel connection of the two IGBT modules, as shown in the

test setup (Figure 5.8), provides a continuous current flow because of the inverse gate signal of IGBT S_1. The IGBT switching is programmed in this way to obtain the half-wave sinusoids in the power loss of IGBT S_2. Correspondingly, the power loss in IGBT S_1 is the inverse half-wave sinusoids.

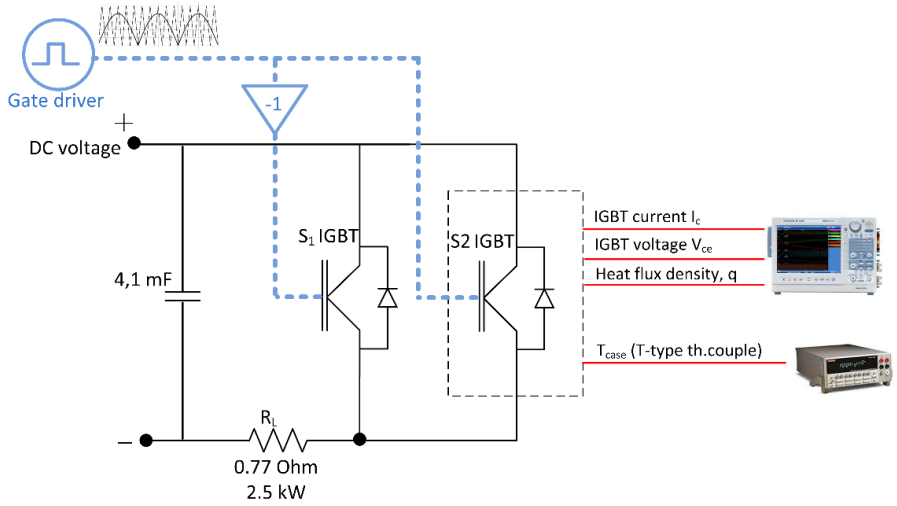

Figure 5.8: Test setup for the heat flux density measurement of the IGBT (Baygildina et al., 2016a).

The block diagram of the test setup modelled in the PLECS is presented in Figure 5.9.

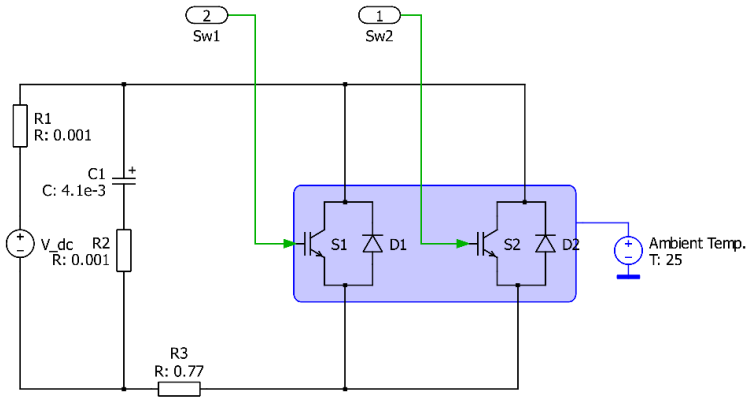

Figure 5.9: PLECS scheme of the test setup (Baygildina et al., 2016a).

Both IGBT modules are mounted on a common air-cooled heat sink, as shown in Figure 5.10.

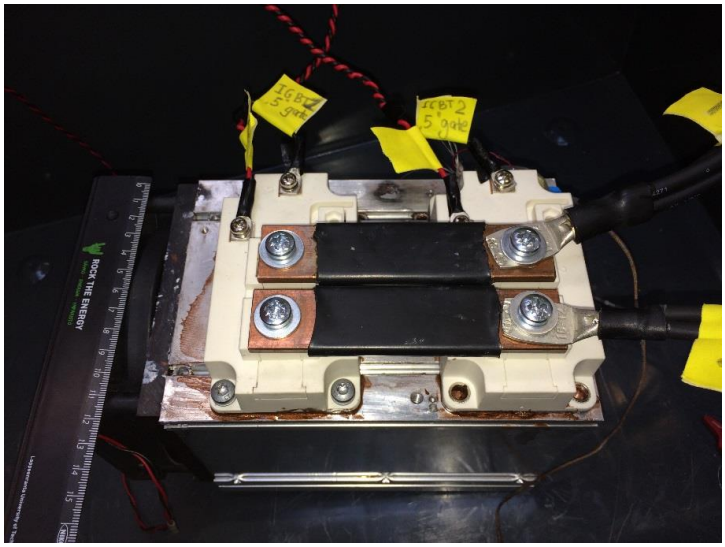

Figure 5.10: Photograph of the IGBT modules mounted on the air cooled heat sink (Baygildina et al., 2016b).

During the test, it was difficult to maintain the constant ambient temperature because of the external heat sources, such as the resistor bank and the power source. However, the initial heat sink temperature was 23ºC, and it has not been used to analyse the heat flux results.

Therefore, the input parameters of the system (Figure 5.9) are the variable operating current and the fundamental frequency. The signals observed during the test on IGBT S_2 are the collector-emitter voltage U_{ce}, the collector current I_c, and thermo-emf measured by the GHFS. The DL850 Scope Corder is used to observe and save the measured data.

The heat flux density q can be defined by

$$q = \frac{E_{\text{th}}}{A_{\text{sensor}} S_0}, \tag{5.3}$$

where A_{sensor} is the area, and S_0 is the volt-watt sensitivity of the GHFS.

Assuming a uniform heat flux distribution over the base plate, the heat flux $Q_{\text{baseplate}}$ can be defined as follows

$$Q_{\text{baseplate}} = qA_{\text{baseplate}}, \tag{5.4}$$

where $A_{\text{baseplate}}$ is the area of the base plate. The latter assumption could cause an error in the heat flux estimation because of the non-uniform heat flux distribution.

Additionally, the base plate temperature and the GHFS thermo-emf are measured by a Keithley 2700 data logger and observed in the LabView interface.

The parameters of the sensor and the IGBT module used to define the heat flux are presented in Table 5.5.

Table 5.5: Parameters of the GHFS and the IGBT module.

Parameter	Value
$A_{\text{baseplate}}$, cm^2	65.3
A_{sensor}, cm^2	0.85
S_0, V/W	15.9×10^{-3}

5.4.1 **Analysis of the heat flux measurements for the normally operating IGBT**

The IGBT loading has been tested at three steady-state currents 15, 30, and 60 A, which correspond to power losses of 6.9, 13.7, and 29.5 W. Owing to the current limit of the DC power source, the IGBT has not been tested at the full load. The test results measured by the Keithley 2700 data logger with the average sampling time of 0.13 s and analysed in the LabView interface are given in Figure 5.11.

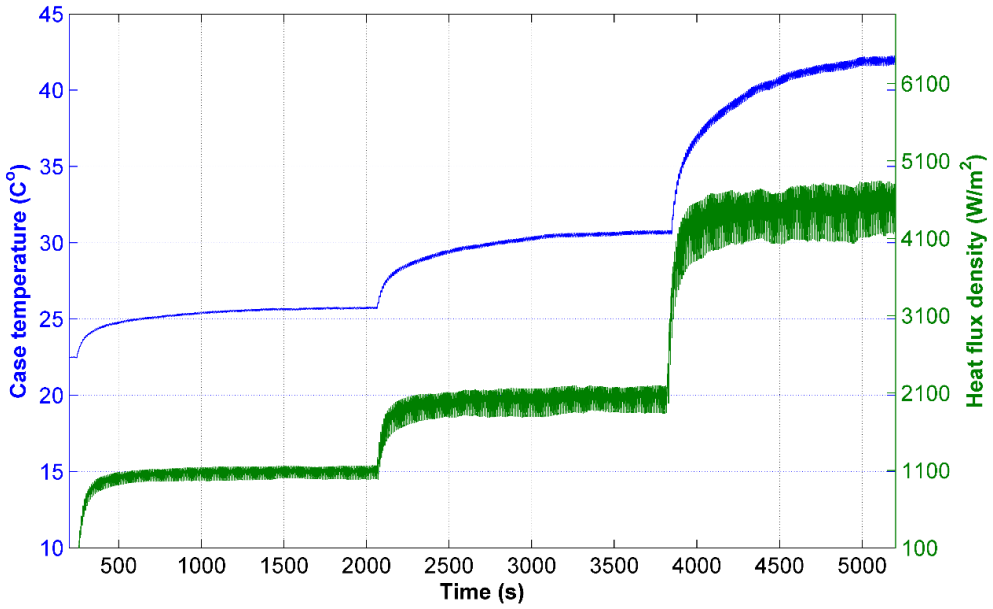

Figure 5.11: Heat flux densities and case temperatures in three steady-state conditions with load currents of 15, 30, and 60 A, a switching frequency of 1 kHz, and a fundamental frequency of 0.1 Hz (Baygildina et al., 2016a).

In Figure 5.11, the transient characteristics of the case temperature and the heat flux density are due to the thermal time response of the entire system, that is, the thermal capacity from the chip to the ambient.

In order to observe the fundamental frequency variations at the higher time resolutions, the heat flux density was measured by the DL850 Scope Corder at the 7 Hz, 15 A operating current and a 0.2 ms time resolution. The results at 0.1 and 7 Hz are combined in Figure 5.12.

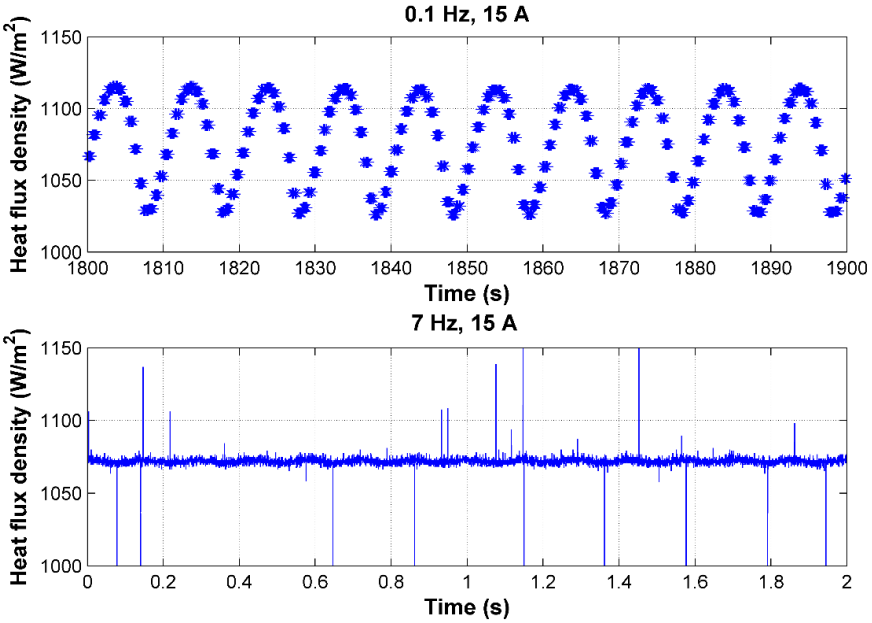

Figure 5.12: Heat flux densities at the fundamental frequencies 0.1 and 7 Hz, switching frequency 1 kHz, and operating current 15 A (Baygildina et al., 2016a).

The heat flux density has a form of half-wave sinusoids with periods of 10 and 0.14 s. At 7 Hz, the half-wave sinusoids are hardly recognizable because of the low amplitude of the sine waves and the significant noise content. As mentioned above, the observed heat flux density does not reflect the fast switching dynamics of the IGBT power loss because of the damping effect of the thermal impedance.

In order to compare the heat fluxes obtained during the test results and the PLECS simulation, the results were averaged by the fundamental frequency (Table 5.6). The differences between the modelled power loss P_{loss} and the measured heat flux Q_{meas} at 15, 30, and 60 A operating current are 1.1 %, 3.5 %, and 3.7 %, respectively.

Table 5.6: Comparison of the heat flux test results with the power loss defined by numerical modelling in Matlab PLECS.

Compared Signals	**Steady State Conditions, DC Current**		
	15 A	**30 A**	**60 A**
Power loss P_{loss} averaged by fundamental frequency, W (modelled by Matlab PLECS)	6.90	13.68	29.50
Measured heat flux Q_{meas} averaged by fundamental frequency, W	6.98	13.20	28.40

The heat flux densities q and q_{FEM}, measured and modelled by the FEM, respectively, are compared in Table 5.7.

Table 5.7: Comparison of the heat flux density test results with the FEM modelling results.

Compared Signals		**Steady State Conditions, DC Current**		
		15 A	**30 A**	**60 A**
Heat flux density (FEM model), q_{FEM} W/m^2	Through HFS	992	1870	4060
	Average over base plate	1075	2025	4332
Measured heat flux density q, W/m^2		1074	2025	4347

The difference between the modelled heat flux density and the heat flux density measured by the GHFS is 6.6 %–8 %. The difference can be explained by the thermal conduction properties of the GHFS–thermal grease combination in the FEM model and the actual case. A small change in the thickness of the thermal grease layer could lead to a significant change in the heat flux density.

5.4.2 **Analysis of the heat flux measurements for degraded IGBT**

The heat flux is measured in the modules with the broken bond wire and the degraded thermal grease. The heat flux density, instantaneous and averaged by the fundamental frequency, for three cases of the power module at 15, 30, and 60 A at 0.7 Hz are shown in Figure 5.13.

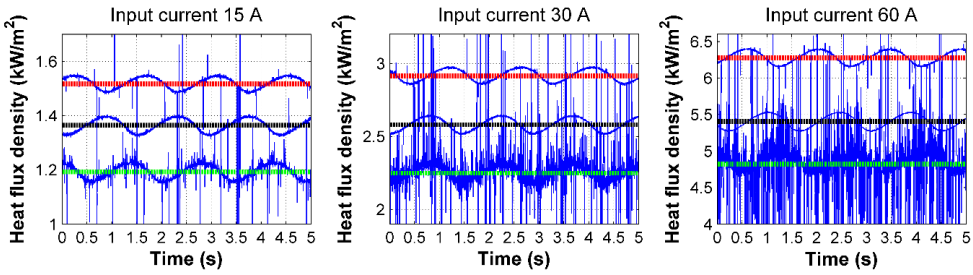

Figure 5.13: Measured heat flux density (blue) of the properly functioning module (IGBT1, green), broken bond wire (IGBT2, red), and degraded thermal grease (IGBT3, black) at 15, 30, and 60 A and 0.7 Hz (Baygildina et al., 2016b).

The heat flux through the sensor Q_{sensor}, averaged by the fundamental frequency, in the properly functioning IGBT is 7.8, 14.70, and 31.52 W at 15, 30, and 60 A, respectively. The corresponding heat flux of the degraded module and its deviation from the heat flux of the properly functioning module, ΔQ, are presented in Table 5.8.

Table 5.8: Measured heat flux Q_{sensor} and deviation from the expected power loss ΔQ.

IGBT status	Measured heat flux Q_{sensor} (W)			Deviation ΔQ (%)		
	15 A	30 A	60 A	15 A	30 A	60 A
Properly functioning IGBT	7.80	14.70	31.52	-	-	-
Broken bond wire (IGBT2)	9.91	19.05	41.02	28.04	30.30	30.14
Degraded thermal grease (IGBT3)	8.92	16.86	35.33	15.24	15.32	12.10

Therefore, the maximum deviation of the measured heat flux, 30.3 % at 30 A, is obtained in the case of the broken bond wire. However, the heat flux deviation in the module with the degraded thermal grease, 12.1–15.3 %, is also significant, and could not be ignored in real-life applications.

It is pointed out that the uncertainty of the measurements has to be reduced. To this end, the quality of the experiment has to be improved. In this context, small changes in the ambient temperature and extraneous heat sources should either be excluded from the measurement results or taken into account in the power loss comparison step. Additionally, the thickness of the thermal grease has a significant impact on the heat flux as a result of its sensitivity to the overall thermal conductivity.

5.5 Model of the CM system implemented in the WT

The basic concept of the proposed CM system is to detect the power semiconductor degradation or failure by measuring the heat flux Q_{sensor} and comparing it with the expected power losses P_{loss}. The latter poses a problem with the options available for fast and precise calculation of power losses. Because of the limited bandwidth of the heat flux measurements, the estimated power and the heat flux are averaged by the fundamental frequency f_{n}. Once the device degradation or failure occurs, a deviation ΔQ is detected.

To define the power losses of the device, the electrical parameters, such as the collector current I_c, the collector-emitter voltage U_{ce} , and the fundamental frequency for averaging are required. In (Zhou et al., 2005), the collector-emitter voltage is derived from look-up tables, where the dependence of U_{ce} on the collector current and the estimated junction temperature T_{j} are predefined. Owing to the high switching frequency and switching transients, a very small time step is required for the measurements. In order to avoid additional sensing circuits for the collector current and an extensive data handling procedure because of the high-frequency PWM, the converter load current I_{load}, that is, the current at the converter terminals can be used. In this case, the switching pattern of the power module should be used to detect the on- and off-states.

Therefore, the power module conduction and switching losses are predefined in look-up tables, where the input parameters are the converter current, the IGBT switching state, and the DC link voltage U_{DC}. In order to estimate the junction temperature, datasheet thermal model parameters and case temperature T_c measurements are required. The structure of the CM system is presented in Figure 5.14.

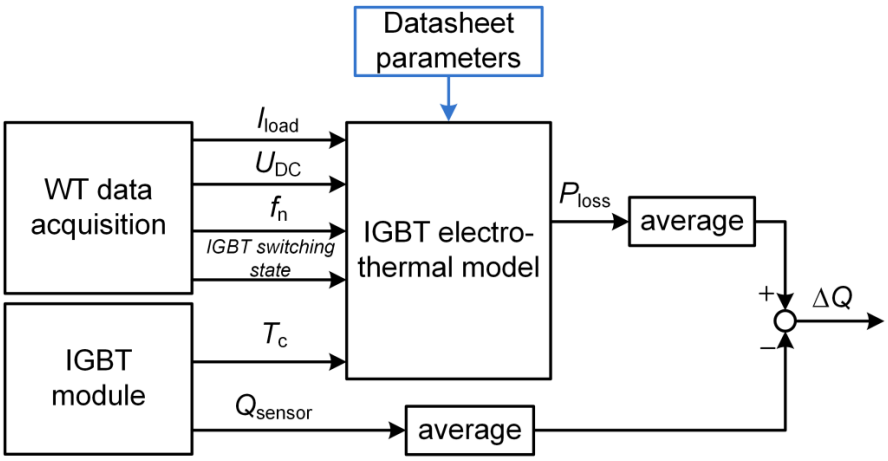

Figure 5.14: CM system for failure and ageing indication of the IGBT in the wind power converter (Baygildina et al., 2016b).

As discussed above, the heat flux measurements are sensitive to ambient temperature fluctuations. Thus, it is reasonable to consider the temperature inside the converter cabinet. The issue related to the dependence of the heat flux on the total thermal conductivity of the system and the uneven heat flux distribution over the base plate could be solved by performing the calibration process before running the CM system.

5.6 Summary

The HFS has been used to monitor IGBT power losses, and it has shown its functionality. The results obtained both by the FEM model and the test setup demonstrate that attention should be paid to increase the accuracy and reliability of the measurements. Indeed, proper thermal parameters of the FEM model would improve the accuracy of the modelling results. Moreover, the non-uniform heat flux density over the base plate obscures the fact how closely the measured heat flux is related to the total power losses.

Considering the GHFS as a technology to monitor the thermal loading of the IGBT in a wind power converter, the main drawback is the limited bandwidth of the heat flux measurement resulting from the thermal impedance of the module package. The sensor could be implemented inside the IGBT structure, under the chip. However, it would significantly disturb the heat flow because of the large differences in the thermal

conductivities of the materials. Thus, in order to compare the measured heat flux with the expected power losses, the results could be averaged by the fundamental frequency.

However, compared with other methods and technologies to monitor thermal loading of power electronics, for instance the present temperature and TSEP sensing circuits, the main advantage of the proposed method is the direct measurement of the thermal stress.

6 Conclusion

In the present research, the reliability problem of the wind power converter has been studied in terms of IGBT thermal load analysis and lifetime estimation. The focus of the study is on the DFIG-based WTs installed on low wind speed sites. The lifetime estimation model comprises the three main degradation factors of power electronics, namely the wind speed dynamics, the specific electrical loading of the DFIG in various wind speed conditions, and the IGBT module package-related failure mechanisms. The wind speed data used in the study have been collected in South-Eastern Finland from 1 June 2014 to 1 June 2015 at the height of 91 m using a LIDAR sensor.

6.1 Final conclusions

The characteristics of the IGBT and diode thermal loading at various wind speeds are found to be complex because of the bidirectional power flow in the DFIG power converter. At different wind speeds and the corresponding fundamental frequencies of the RSC, the IGBT and the diode on-state durations are also different. The rotor circuit parameters, such as the power factor and the modulation index, determine the power loss distribution between the IGBT and the diode. An increasing power factor in the sub-synchronous mode induces more power losses in the RSC IGBT than in the diode. The decreasing modulation index, which is a function of generator slip, instead, induces more stress on the diode. However, the IGBT power losses are dominating. In the GSC, the power losses are mostly affected by the power flow in the sub- and super-synchronous modes, because the modulation index and the power factor remain constant. In the sub-synchronous mode, the GSC is operating as a rectifier, thereby inducing more conduction losses in the diode, and on the other hand, more IGBT conduction losses in the inverter mode. However, because of the switching losses, the total power losses are dominating in the IGBT. More generally, the converter operation in the DFIG drive WTs and the corresponding power flow specify the ambiguous characteristics of the IGBT and diode power loss distribution over the wind speed range.

When considering the junction temperature behaviour at various wind speeds, the RSC has a higher mean junction temperature and amplitudes as a result of the lower operating fundamental frequency than in the GSC. The local maximum is at the synchronous operating point, which corresponds to 8.1 m/s. However, at the nominal wind speed, the average value of the junction temperature and the temperature swings are higher. Thus, the operation of II and III wind speed class WTs, which are manufactured for 7.5–8.5 m/s average speeds, could induce accelerated thermal wear-out of the power electronics. However, a reasonable choice at the design stage of the DFIG is to select the synchronous operation point other than operation point corresponding to the average wind speed.

The calculated power losses are used in the IGBT lifetime estimation model in the form of look-up tables. The model uses the turbulent wind and the wind speed distribution as inputs in order to reflect the effect of the site-specific wind conditions on the IGBT degradation. The model is built in such a way that the junction temperature contains the

variations associated with the turbulent dynamics of the wind speed. The corresponding temperature profile in the time domain is converted into a sequence of counted temperature cycles with specific mean values, swings, and periods of cycles. Each counted cycle causes an individual damage to the power device. Thus, the data of the counted cycles are applied to define the device lifetime using Miner's rule for accumulated degradation.

According to one-year consumed B10 lifetime, the highest probability of device failure is due to the bond wire lift-off both in the RSC and the GSC. The chip and base plate solders are found to be more stress-resistant. In the RSC, the peak of the consumed lifetime is obtained at 6 m/s, which is the average wind speed on the site, however, with the minimum TI level. In the GSC, the power device is more stressed at the nominal operating point.

It can be concluded that the lifetime consumption is mostly affected by the local wind speed distribution. Even though the wind speed fluctuations with a turbulence level are taken into account, a smoothing effect of the WT inertia takes place in the loading profile of the converter. Obviously, the high junction temperature fluctuations of the RSC in the synchronous operating point produce the degradation effect of the IGBT package; however, this effect is not explicitly visible in the diagrams.

The application of the GHFS in power electronics was analysed in the present research. The sensor has essential benefits over the temperature sensors and the temperature-based HFSs. These are the direct heat flux measurement, in other words, there is no need for additional processing of the temperature data; and the usability, that is, the sensor does not require an access to the internal structure of the module. According to the heat flux measurement results, the maximum deviation from the modelled power losses is 3.7 %. The uncertainty in the measurements is associated with the possible changes in the ambient temperature and the effect of the undesired heat sources near the test setup. The uncertainties in the FEM modelling could be explained by the erroneous thermal conductivity of the GHFS–thermal grease combination and the improper thicknesses of the layer.

The proposed method for the CM system may seem technologically immature owing to such factors as the uniform distribution of the heat flux density over the base plate, the high noise content at high frequencies, and the limited bandwidth of the measurements because of the thermal impedance of the IGBT module. However, the general idea of using the GHFS and the first integration steps in a power electronics application are considered in the present doctoral dissertation.

6.2 Suggestions for future work

Further work should concentrate on the effect of short-term and long-term temperature variations on the IGBT lifetime. Because the short-term thermal cycles are associated with the IGBT switching, and long-term thermal cycles are related to the seasonal changes

in the wind speed and the ambient temperature, it will be possible to combine both the IGBT thermal stress factors in one model. However, the calculation of the IGBT lifetime may consume considerable computer resources.

The present doctoral dissertation focused on the IGBT module topology. However, the lifetime model of the advanced packaging topology, such as press-pack IGBTs, where the solder and bond wires are eliminated, would be an interesting topic to investigate. Because of its higher power density than in the IGBT module topology, the press-pack package may induce new failure modes. Moreover, the failure modes of the press-pack technology are still to be developed by researchers and manufacturers.

Further work associated with the application of the HFS for thermal loading analysis would suggest performing more tests with heat flux measurements with complete knowledge of the thermal model and ambient conditions. Additionally, it would be interesting to observe the IGBT heat flux within the converter cabinet while the converter is loaded. However, the application of the HFS requires further work in advancing the usability of the sensor.

References

Abad, G. et al., 2011. *Doubly Fed Induction Machine. Modeling and Control for Wind Energy Generation.* Hoboken: John Wiley & Sons.

ABB, 2014a. *Load-cycling capability of HiPak IGBT modules,* Lenzburg: ABB.

ABB, 2014b. *IGBT Module 5SNA 1600N170100 datasheet,* ABB Switzerland Ltd.

ABB, 2016. *Technical data of ACS800 low voltage wind turbine converter.* [Online] Available at: http://new.abb.com/power-converters-inverters/wind-turbines/utility-scale/acs800/technical-data
[Accessed 29 March 2016].

Abu-Rub, H., Malinowski, M. & Al-Haddad, K., 2014. *Power electronics for renewable energy systems, transportation and industrial application.* Chichester: John Wiley & Sons.

Ackermann, T. & Söder, L., 2002. An overview of wind energy-status 2002. *Renewable and Sustainable Energy Reviews,* 6(1–2), pp. 67–127.

Akhmatov, V., 2003. Variable-Speed Wind Turbines with Doubly-Fed Induction Generators, Part III: Model with the Back-to-back Converters. *Wind Engineering,* 27(2), pp. 79–91.

Amro, R. & Lutz, J., 2004. *Power Cycling with High Temperature Swing of Descrete Components based on Different Technologies.* In IEEE 35th Annual Power Electronics Specialists Conference, pp. 2593–2598.

AnalogDevices, 2000. *Flux and Speed Estimation for Induction Machines,* Analog Devices Inc.

Andresen, B. & Birk, J., 2007. *A high power density converter system for the Gamesa G10x 4.5 MW Wind turbine.* In European Conference on Power Electronics and Applications, pp. 1–9.

Avenas, Y., Dupont, L. & Khatir, Z., 2012. Temperature Measurement of Power Semiconductor Devices by Thermo-Sensitive Electrical Parameters - A Review. *IEEE Transactions on Power Electronics,* 27(6), pp. 3081–3092.

Bartram, M., von Bloh, I. & De Doncker, R. W., 2004. *Doubly-Fed-Machines in Wind-Turbine Systems: Is this Application Limiting the Lifetime of IGBT-Frequency-Converters?.* In 35th Annual Power Electronics Specialists Conference, pp. 2583–2587.

Bayerer, R. et al., 2008. *Model for Power Cycling Lifetime of IGBT Modules - Various Factors Influencing Lifetime.* In 5th International Conference on Integrated Power Systems (CIPS), pp. 1–6.

Baygildina, E. et al., 2016b. Condition Monitoring of Wind Power Converters Using Heat Flux Sensor. *International Review of Electrical Engineering,* 11(3), pp. 239–246.

Baygildina, E. et al., 2016a. Application of a heat flux sensor in wind power electronics. *Energies,* 9(6).

Belu, R. & Koracin, D., 2012. *Effect of complex wind regimes and meteorlogical parameters on wind turbine performances.* In Energytech, pp. 1–6.

Berner, J., 2012. *Load-cycling capability of HiPak IGBT modules, ABB application Note 5SYA 2043-02,* ABB.

Birk, J. & Andresen, B., 2008. *Parallel-Connected Converters for Optimizing Efficiency, Reliability and Grid Harmonics in a Wind Turbine.* In European Conference on Power Electronics and Applications, pp. 1–7.

Blaabjerg, F. et al., 2011. *Power Electronics - Key Technology for Renewable Energy Systems.* In 3rd International Conference on Electric Power and Energy Conversion Systems (EPECS), pp. 1–6.

Blaabjerg, F., Liserre, M. & Ma, K., 2012. Power electronics converters for wind turbine systems. *IEEE Transactions on Industry Applications,* 48(2), pp. 708–715.

Blaabjerg, F. & Ma, K., 2013. Future on Power Electronics for Wind Turbine Systems. *IEEE Journal of Emerging and Selected Topics in Power Electronics,* 1(3), pp. 139–152.

Buist, J., 2014. *The 10 Biggest Turbines in the World.* [Online] Available at: http://www.windpowermonthly.com/10-biggest-turbines

Burton, T., Sharpe, D., Jenkins, N. & Bossanyi, E., 2001. *Wind Energy*. Chichester: Wiley.

Busca, C., 2011. *Modeling Lifetime of High Power IGBTs in Wind Power Applications - An overview*. IEEE International Symposium on Industrial Electronics (ISIE), pp. 1408–1413.

Bywaters, G. et al., 2004. *Northen power systems WindPACT Drive Train Alternative Design Study Report,* Golden: NREL.

Cauer, E., Mathis, W. & Pauli, R., 2000. *Life and Work of Wilhelm Cauer (1900-1945).* Perpignan, Princeton University.

Chamund, D., Coulbeck, L., Newcombe, D. & Waind, P., 2009. *High Power Density IGBT module for high reliability applications.* In IEEE 6th International Power Electronics and Motion Control Conference (IPEMC '09), pp. 274–280.

Chaudhary, S. K., Teodorescu, R., Rodriguez, P. & Kjær, P., 2009. *Chopper Controlled Resistors in VSC-HVDC Transmission for WPP with Full-Scale Converters.* In IEEE PES/IAS Conference on Sustainable Alternative Energy (SAE). [Online] Available at: http://vbn.aau.dk/files/19237667/Publication

Chen, Y. et al., 2012. *A comprehensive analytical and experimental investigation of wire bond life for IGBT modules.* In Twenty-Seventh Annual IEEE Applied Power Electronics Conference and Exposition (APEC), pp. 2298–2304.

Ciappa, M., 2000. *Some Reliability Aspects of IGBT Modules for High-Power Applications,* Zurich: Swiss Federal Institute of Technology.

Ciappa, M., 2002. Selected failure mechanisms of modern power modules. *Microelectronics Reliability* , pp. 653–667.

COMSOL, M., 2015. *COMSOL Multiphysics® Modeling Software, The Finite Element Method (FEM).* [Online] Available at: https://www.comsol.com/multiphysics/finite-element-method [Accessed 24 October 2016].

Coquery, G. & Lallemand, R., 2000. Failure criteria for long term Accelerated Power Cycling Test linked to electrical turn off SOA on IGBT module. A 4000 hours test on 1200A–3300V module with AlSiC base plate. *Microelectronics Reliability*, 40(8-10), pp. 1665–1670.

Coquery, G. et al., 1999. *Reliability Improvement of the Soldering Thermal Fatigue with AlSiC Technology on Traction High-Power IGBT Modules.* Lausanne, IEEE.

Cova, P. & Fantini, F., 1998. On the Effect of Power Cycling Stress on IGBT modules. *Microelectronics Reliabilty,* Issue 38, pp. 1347–1352.

Diller, T. E., 1999. Heat Flux. In: J. Webster, ed. *Handbook for measurement instrumentation sensors.* Boca Raton: CRC Press LLC, pp. 1127–1141.

Duvvury, C., Rodriguez, J., Jones, C. & Smayling, M., 1994. *Device integration for ESD robustness of high voltage power MOSFETs.* International Electron Devices Meeting (IEDM '94).

Faulstich, S., Lyding, P. & Hahn, B., 2010. *Electrical subassemblies of wind turbines - a substantial risk for the availability.* Warschau, European Wind Energy Conference and Exhibition (EWEC).

Fischer, K. et al., 2012. *Investigation of Converter Failure in Wind Turbines,* Stockholm: Elforsk.

Fischer, K. et al., 2014. Field-Experience Based Root-Cause Analysis of Power-Converter Failure in Wind Turbines. *IEEE Transactions on Power Electronics,* 30(5), pp. 2481–2492.

Fletcher, J. Y. J., 2010. *Introduction to the Doubly-Fed Induction Generator for Wind Power Applications, Paths to Sustainable Energy.* [Online] Available at: http://www.intechopen.com/books/paths-to-sustainable-energy/introduction-to-the-doubly-fed-inductiongenerator- [Accessed 4 August 2016].

Fovell, R. G., 2010. *Meteorology: An Introduction to the Wonders of the Weather,* Los Angeles

Gowda, A., 2007. *Reliability Testing Of Thermal Greases.* [Online] Available at: https://www.electronics-cooling.com/2007/11/reliability-testing-of-thermal-greases/ [Accessed 7 November 2016].

Gunturi, S. & Schneider, D., 2009. *Press pack power semiconductor module.* Switzerland, Patent No. US7538436 B2.

GWEC, 2016. *Global Wind Report, Annual Market Update,* Brussels: Global Wind Energy Council.

Harnefors, L. & Nee, H.-P., 1998. Model-Based Current Control of AC Machines Using the Internal Model Control Method. *IEEE Transactions on Industry Applications,* 34(1), pp. 133–141.

Hashin, Z. & Rotem, A., 1977. *A Cumulative Damage Theory of Fatigue Failure,* Tel-Aviv: School of Engineering Tel-Aviv University.

Heier, S., 2014. *Grid integration of wind energy conversion systems.* 3rd ed. New York: Jon Wiley & Sons.

Held, M. et al., 1997. *Fast Power Cycling Test for IGBT Modules in Traction Application.* In International Conference on Power Electronics and Drive Systems.

Hu, J. B., 1997. New Integration Algorithms for Estimation Motor Flux Over a Wide Speed Range. *IEEE Transactions on Power Electronic,*13(5), pp. 969-977.

IEC, 2005. *IEC 61400-1,* Geneva, Switzerland: International Electrotechnical Commission.

IEEE, 1994. *IEEE Recommended Practice for Electric Power Distribution for Industrial Plants,* s.l.: IEEE Std 141-1993.

Ikonen, M., 2012. *Power Cycling Lifetime Estimation of IGBT Power Modules Based on Chip Temperature Modeling.* Acta Universitatis Lappeenrantaensis 504, Lappeenranta University of Technology, Finland

Infineon, 2011. *Technical information for FZ400R17KE4 IGBT module,* Neubiberg: Infineon.

Infineon, 2016. *Increasing IGBT Inverter Power Density*. [Online] Available at: http://www.powerguru.org/increasing-igbt-inverter-power-density/

Ingeteam, 2016. *Technical data of Ingecon Wind DFM low voltage power convrter*. [Online]
Available at: http://www.ingeteam.com/Portals/0/Catalogo/Producto/Documento/PRD_889_Archivo_data-sheet-dfm-eu-august-2014.pdf
[Accessed 29 March 2016].

Irvine, T., 2011. *Rainflow Cycle Counting in Fatigue Analysis*, Pennsylvania: Pennsylvania State University.

Jones, R. & Waite, P., 2011. *Optimised power converter for multi-MW direct drive permanent magnet wind turbines.* In European Conference on Power Electronics and Applications, pp. 1–10.

Khanna, V. K., 2003. *Insulated Gate Bipolar Transistor, theory and design.* Chichester: John Wiley & Sons.

King, D., 1992. *Fluidized catalytic crackers: an engineering review*. New York, Engineering Foundation, pp. 15–26.

Kovacevic, I., Drofenik, U. & Kolar, W., 2010. *New Physical Model for Lifetime Estimation of Power Modules.* In International Power Electronics Conference (IPEC), pp. 2106–2114.

Luo, M., 2014. *Multi-Physical Domain Modeling of a DFIG Wind Turbine System using PLECS, Plexim Application Note,* Zurich: Plexim GmbH.

Ma, K., 2013. *Power electronics for the next generation wind turbine system,* Aalborg: UniPrint.

Ma, K., Bahman, A. S., Beczkowski, S. & Blaabjerg, F., 2015. Complete loss and thermal model of power semiconductors including device rating information. *IEEE Transactions on Power Electronics,* 30(5), pp. 2556–2569.

Ma, K. & Blaabjerg, F., 2012. The Impact of Power Switching Devices on the Thermal Performance of a 10 MW Wind Power NPC Converter. *Energies*, 5(7), pp. 2559–2577.

Ma, K., Liserre, M., Blaabjerg, F. & Kerekes, T., 2015. Thermal Loading and Lifetime Estimation for Power Device Considering Mission Profiles in Wind Power Converter. *IEEE Transactions on Power Electronics*, pp. 590–602.

Manwell, J., McGowan, J. & Rogers, A., 2009. *Wind Energy Explained - Theory, Design and Application.* Chichester: Wiley.

MathWorks, 2016. *Wind Turbine.* [Online]
Available at:
http://se.mathworks.com/help/physmod/sps/powersys/ref/windturbine.html
[Accessed 21 July 2016].

Mathworks, 2016. *Wind Turbine Doubly-Fed Induction Generator (Phasor Type).* [Online]
Available at:
http://se.mathworks.com/help/physmod/sps/powersys/ref/windturbinedoublyfedinductiongeneratorphasortype.html
[Accessed 21 July 2016].

Meshram, S., 2013. *What is the most efficient design for a wind turbine?.* [Online] Available at: https://www.quora.com/What-is-the-most-efficient-design-for-a-wind-turbine
[Accessed 23 September 2016].

Mityakov, A. V., Sapozhnikov, S. Z., Mityakov, V. Y. & Snarskii, A. A., 2012. Gradient heat flux sensors for high temperature environments. *Sensors and Actuators A: Physical*, Volume 176, pp. 1–9.

Muljadi, E., Singh, M. & Gevorgian, V., 2012. *Doubly Fed Induction Generator in an Offshore Wind Power Plant Operated at Rated V/Hz.* Raleigh, NREL.

Munteanu, I., Bratcu, A., Cutululis, N.-A. & Ceanga, E., 2008. *Optimal control of wind energy systems.* London: Springer.

Mutschler, P. & Hoffinann, R., 2002. *Comparison of Wind Turbines Regarding their Energy Generation.* In IEEE 33rd Annual Power Electronics Specialists Conference, pp. 6–11.

Nichita, C., Luca, D., Dakyo, B. & Ceanga, E., 2002. Large band simulation of the wind speed for real time wind turbine simulators. *IEEE Transactions on Energy Conversion*, 17(4), pp. 523–529.

Nieslony, A., 2009. Determination of Fragments of Multiaxial Service Lading Strongly Influencing the Fatigue of Machine Components. *Mechanical Systems and Signal Processing*, Issue 23, pp. 2712–2721.

Olivier, H., 2003. *Thin Film Gauges and Coaxial Thermocouples for Measuring Transient Temperatures*, Aachen: RWTH.

Ortolano, D. & Hines, F., 1983. A simplified approach to heat flow measurement. *Advances in Instrumentation*, 38(2), pp. 1449–1456.

Patil, N., Das, D., Goebel, K. & Pecht, M., 2008. *Failure Precursors for Insulated Gate Bipolar Transistors.* Denver.

Perpiñà, X. et al., 2012. Reliability and Lifetime Prediction for IGBT Modules in Railway Traction Chains. In: X. Perpinya, ed. *Reliability and Safety in Railway.* Rijeka: InTech, pp. 193–222.

Petersson, A., 2005. *Analysis, Modeling and Control of Doubly-Fed Induction Generators for Wind Turbines*, Göteborg: Chalmers University of Technology.

Petersson, A., 2005. *Analysis, Modeling and Control of Doubly-Fed Induction Generators for Wind Turbines*, Göteborg: Chalmers University of Technology.

PLECS library, A. n., 2016. *DFIG Wind Turbine System.* [Online] Available at: https://www.plexim.com/support/application-examples/282 [Accessed 4 April 2017].

PLECS, 2016. *Thermal Simulation.* [Online] Available at: http://www.plexim.com/plecs/thermal [Accessed 14 July 2016].

Poore, R. & Lettenmaier, T., 2003. *Alternative Design Study Report: WindPACT Advanced Wind Turbine Drive Train Design Study*, Golden: National Renewable Energy Laboratory.

Ragheb, A. M. & Ragheb, M., 2011. Wind Turbine Gearbox Technologies. In: R. Carriveau, ed. *Wind Turbine Gearbox Technologies, Fundamental and Advanced Topics in Wind Power.* Rijeka: InTech, pp. 189–206.

Reznik, A., Simoes, M., Al-Durra, A. & Muyeen, S. M., 2013. LCL Filter Design and Performance Analysis for Grid-Interconnected Systems. *IEEE Transactions on Industry Applications*, 50(2), pp. 1225–1232.

Roshanfekr, P., Thiringer, T., Lundmark, S. & Alatalo, M., 2012. *Selecting IGBT module for a high voltage 5 MW wind turbine PMSG-equipped generating system.* In IEEE Power Electronics and Machines in Wind Applications (PEMWA), pp. 1–6.

Sapozhnikov, S. Z. et al., 2012. The Calibration of Gradient Heat Flux Sensors. *Measurement Techniques,*, 54(10), pp. 1155–1159.

Schnell, R. S. U., 2004. *Realistic benchmarking of IGBT-modules with the help of a fast and easy to use simulation-tool.* Nuremberg, ABB Switzerland.

Senturk, O., 2011. *High Power Density Power Electronic Converters for Large Wind Turbines,* Aalborg: Aalborg University.

Sheng, S., 2013. *Report on wind turbine subsystem reliability - a survey of various databases,* Golden: NREL.

Smirnova, L., 2015. *Electromagnetic and Thermal Design of a Multilevel Converter with High Power Density and Reliability.* 2015: Acta Universitatis Lappeenrantaensis 504, Lappeenranta University of Technology, Finland.

Socie, D. & Marquis, G., 1999. *Multiaxial fatigue.* Chicago: University of Illinois at Urbana-Champaign.

Srajber, D. L. W., 1992. The calculation of the power dissipation for the IGBT and the inverse diode in circuits with sinusoidal output voltage. *Electronika,* pp. 52–58.

Tavner, P., 2011. *How Are We Going to Make Offshore Wind Farms More Reliable?.* Durham, Durham University.

Torsten, T., 2015. *Thinking Big, Offshore Wind Industry.* [Online] Available at: http://www.offshorewindindustry.com/news/thinking-big [Accessed 23 November 2016].

Valentine, N., Das, D. & Pecht, M., 2015. *Failure Mechanisms of Insulated Gate Bipolar Transistors (IGBTs).* Golden, NREL.

Van Hulle, F. & Fichaux, N., 2010. *Powering Europe: Wind Energy and The Electricity Grid,* Brussels: EWEA.

van Wachem, B. & Sasic, S., 2008. Derivation, simulation and validation of a cohesive particle flow CFD model. *AIChE Journal,* 54(1), pp. 9–19.

Vestas, M., 2016. *MHI Vestas Offshore Wind,* Aarhus.

VestasOffshore, 2016. *First V164-8.0 MW turbine installed at Burbo Bank Extension.* [Online] Available at: http://www.mhivestasoffshore.com/first-v164-8-0-mw-turbine-installed-burbo-bank-extension-2/ [Accessed 22 November 2016].

VestasWindSystems, 2011. *Vestas V164 brochure.* [Online] Available at: http://pdf.archiexpo.com/pdf/vestas/vestas-v164-80-mw/88087-134417.html
[Accessed 10 October 2016].

Viswanath, R., Wakharkar, V., Watwe, A. & and Lebonheur, V., 2000. Thermal Performance Challenges from Silicon to Systems. *Intel Technology Journal*, 4(3), pp. 1–16.

Wægter, J., 2009. *Stress range histories and rain flow counting*, Aalborg: Aalborg University.

Wang, X., Castellazzi, A. & Zanchetta, P., 2013. Observer Based Temperature Control for Reduced Thermal Cycling in Power Electronic Cooling. *Applied Thermal Engineering*, 64(1-2), pp. 10–18.

Wei, L. et al., 2011. Analysis of IGBT Power Cycling Capabilities Used in Doubly-Fed Induction Generator Wind Power System. *IEEE Transactions on Industry Applications*, 47(4), pp. 1794–1801.

Weiss, D. & Eckel, H.-G., 2013. *Fundumental Frequency and Mission Profile Wearout of IGBT in DFIG Converters for Wind Power.* In 15th European Conference on Power Electronics and Applications (EPE), pp. 1–6.

Wintrich, A., Nicolai, U., Tursky, W. & Reimann, T., 2015. *Application Manual Power Semiconductors*, Ilmenau: SEMIKRON International GmbH.

Yang, S. et al., 2010. Condition Monitoring for Device Reliability in Power Electronic Converters: A Review. *IEEE Transaction on Power Electronics*, 25(11), pp. 2734–2752.

Yun, C., Malberti, P., Ciappa, M. & Fichter, W., 2001. Thermal Component Model For Electrothermal Analysis of IGBT Module Systems. *IEEE Transactions on Advanced Packaging*, 24(3), pp. 401–406.

Zhou, D., Blaabjerg, F., Lau, M. & Tonnes, M., 2012. *Thermal Analysis of Multi-MW Two-level Wind Power Converter.* In 38th Annual Conference on IEEE Industrial Electronics Society (IECON), pp. 5858–5864.

Zhou, Z. et al., 2005. *A fast power loss calculation method for long real time thermal simulation of IGBT modules for a three-phase inverter system.* In European Conference on Power Electronics and Applications (EPE).

Appendix A: Control of machine-side and grid-side converters

A. RSC control scheme

The control system of the RSC consists of outer loops for the reactive power and rotational speed control, and an inner loop for current control. The stator-flux-oriented frame is applied in the current control system so that the stator flux vector Ψ_s is aligned with the d-axis.

In order to simplify the synthesis of the RSC current control system in the stator reference frame, it is reasonable to derive a Γ-type DFIG equivalent model, where the stator leakage inductance L_{ls} is moved to the rotor circuit (Figure A.1).

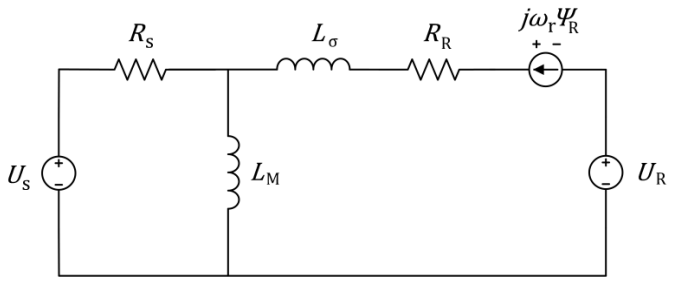

Figure A.1: Γ-type equivalent circuit of the DFIG in the stator reference frame.

In Figure A.1, U_s denotes the stator voltage, R_s is the stator resistance, L_M is the magnetizing inductance, L_σ is the leakage inductance in the Γ-type equivalent circuit, R_R is the rotor resistance, $j\omega_r\Psi_R$ is the voltage induced by the speed difference between the stator and rotor reference frames, and U_R is the rotor voltage.

The γ-parameter is introduced (Petersson, 2005);

$$\gamma = \frac{L_{ls}+L_m}{L_m}. \tag{A.1}$$

where L_m is the magnetizing inductance and L_{ls} is the leakage inductance in the T-type equivalent circuit (Figure 3.4). Thus, the electrical circuit parameters are modified as follows

$$U_R = \gamma\, U_r, \tag{A.2}$$

$$I_{\mathrm{R}} = \frac{I_{\mathrm{r}}}{\gamma}, \tag{A.3}$$

$$\Psi_{\mathrm{R}} = \gamma\, \Psi_{\mathrm{r}}, \tag{A.4}$$

$$R_{\mathrm{R}} = \gamma^2\, R_{\mathrm{r}}, \tag{A.5}$$

$$L_{\sigma} = \gamma L_{\mathrm{ls}} + \gamma^2 L_{\mathrm{lr}}, \tag{A.6}$$

$$L_{\mathrm{M}} = \gamma L_{\mathrm{m}}. \tag{A.7}$$

Representing the DFIG voltage equations in the general reference frame, rotating at the synchronous speed ω_{s},

$$U_{\mathrm{s}} = R_{\mathrm{s}} I_{\mathrm{s}} + j\omega_{\mathrm{s}} \Psi_{\mathrm{s}} + \frac{d\Psi_{\mathrm{s}}}{dt}, \tag{A.8}$$

$$U_{\mathrm{R}} = R_{\mathrm{R}} I_{\mathrm{R}} + j\omega_{\mathrm{slip}} \Psi_{\mathrm{R}} + \frac{d\Psi_{\mathrm{R}}}{dt}. \tag{A.9}$$

The stator flux Ψ_{s} and the rotor flux Ψ_{R} are defined as

$$\Psi_{\mathrm{s}} = L_{\mathrm{M}}(I_{\mathrm{s}} + I_{\mathrm{R}}), \tag{A.10}$$

$$\Psi_{\mathrm{R}} = (L_{\mathrm{M}} + L_{\sigma}) I_{\mathrm{R}} + L_{\mathrm{M}} I_{\mathrm{s}}\,. \tag{A.11}$$

In order to derive the reference voltage equations for the rotor current control scheme, it is reasonable to eliminate the stator current I_{s} and the rotor flux Ψ_{R} from Equations A.24 and A.25.

Modification of Equations A.26 and A.27 yields

$$I_{\mathrm{s}} = \frac{\Psi_{\mathrm{s}}}{L_{\mathrm{M}}} - I_{\mathrm{R}}, \tag{A.12}$$

$$\Psi_{\mathrm{R}} = \Psi_{\mathrm{s}} + L_{\sigma} I_{\mathrm{R}}. \tag{A.13}$$

- **Stator reactive power control**

Let us consider the DFIG stator power equations in the d-q-oriented frame. The apparent power S_{s} can be written as (Petersson, 2005)

$$S_{\mathrm{s}} = 3U_{\mathrm{s}} I_{\mathrm{s}}^{*} . \tag{A.14}$$

Taking into account Equation (3.25) and assuming that the stator flux remains constant, in other words, the stator flux derivative is neglected, Equation (A.14) yields

$$\begin{aligned} S_{\mathrm{s}} = 3(R_{\mathrm{s}} I_{\mathrm{s}} + j\omega_{\mathrm{s}} \Psi_{\mathrm{s}}) I_{\mathrm{s}}^{*} &= 3R_{\mathrm{s}} |I_{\mathrm{s}}|^2 + 3j\omega_{\mathrm{s}} \Psi_{\mathrm{s}} I_{\mathrm{s}}^{*} \\ &= 3R_{\mathrm{s}} |I_{\mathrm{s}}|^2 \\ &+ 3j\omega_{\mathrm{s}} \left(\left(\Psi_{\mathrm{sd}} + j\Psi_{\mathrm{sq}} \right) \left(I_{\mathrm{sd}} - jI_{\mathrm{sq}} \right) \right) \\ &= 3R_{\mathrm{s}} |I_{\mathrm{s}}|^2 + 3\omega_{\mathrm{s}} \left(\Psi_{\mathrm{sd}} I_{\mathrm{sq}} - \Psi_{\mathrm{sq}} I_{\mathrm{sd}} \right) \\ &+ 3\omega_{\mathrm{s}} j \left(\Psi_{\mathrm{sd}} I_{\mathrm{sd}} + \Psi_{\mathrm{sq}} I_{\mathrm{sq}} \right). \end{aligned} \tag{A.15}$$

Thus, the active and reactive power of the stator can be written as

$$P_{\mathrm{s}} = 3R_{\mathrm{s}} |I_{\mathrm{s}}|^2 + 3\omega_{\mathrm{s}} \left(\Psi_{\mathrm{sd}} I_{\mathrm{sq}} - \Psi_{\mathrm{sq}} I_{\mathrm{sd}} \right), \tag{A.16}$$

$$Q_{\mathrm{s}} = 3\omega_{\mathrm{s}} \left(\Psi_{\mathrm{sd}} I_{\mathrm{sd}} + \Psi_{\mathrm{sq}} I_{\mathrm{sq}} \right). \tag{A.17}$$

As the d-q coordinate system is oriented to the stator flux, the q-axis component Ψ_{sq} is set to zero, and $\Psi_{\mathrm{s}} = \Psi_{\mathrm{sd}}$. The active and reactive power can be represented as

$$P_{\mathrm{s}} = 3R_{\mathrm{s}} |I_{\mathrm{s}}|^2 + 3\omega_{\mathrm{s}} \Psi_{\mathrm{s}} I_{\mathrm{sq}}, \tag{A.18}$$

$$Q_{\mathrm{s}} = 3\omega_{\mathrm{s}}\Psi_{\mathrm{s}}I_{\mathrm{sd}} = 3\omega_{\mathrm{s}}\Psi_{\mathrm{s}}\left(\frac{\Psi_{\mathrm{s}}}{L_{\mathrm{M}}} - I_{\mathrm{Rd}}\right). \tag{A.19}$$

If the reactive power reference is set to zero, the d-axis current is

$$I_{\mathrm{Rd}}^{\mathrm{ref}} = \frac{\Psi_{\mathrm{s\_est}}}{L_{\mathrm{M}}}. \tag{A.20}$$

Assuming that the plant $G_{\mathrm{Q_sI_{Rd}}}$ uses the rotor d-axis current I_{rd} as an input and the reactive power Q_{s} as an output, the plant is

$$G_{Q_{\mathrm{s}}I_{\mathrm{Rd}}} = -3\omega_{\mathrm{s}}\Psi_{\mathrm{s\_est}}. \tag{A.21}$$

The magnetizing current in Equation (A.8), $\Psi_{\mathrm{s}}/L_{\mathrm{M}}$, is close to constant, and thus, it is compensated by the integration term of the controller. In order to derive the controller transfer function, the plant $G_{Q_{\mathrm{s}}I_{\mathrm{Rd}}}$ can be used. In this context, an internal model control (IMC) (Petersson, 2005) uses the reciprocate of $G_{Q_{\mathrm{s}}I_{\mathrm{Rd}}}$ to define the integrator gain $K_{\mathrm{rs\_id}}$ in such a way that the controller transfer function is expressed as

$$C(p) = \frac{\alpha}{p}G_{Q_{\mathrm{s}}I_{\mathrm{Rd}}}^{-1}, \tag{A.22}$$

where $p = \frac{d}{dt}$ is the Laplace variable. Therefore,

$$K_{rs\_id} = -\frac{\alpha_{\mathrm{Q}}}{3\omega_{\mathrm{s}}\Psi_{\mathrm{s\_est}}}, \tag{A.23}$$

where α_{Q} is the bandwidth of the closed-loop system, $\alpha_{\mathrm{Q}} = \frac{ln9}{t_{\mathrm{rise}}}$.

Assuming that the estimated stator flux $\Psi_{\mathrm{s\_est}} \approx U_{\mathrm{s\_nom}}/\omega_{\mathrm{s}}$, where $U_{\mathrm{s\_nom}}$ is the nominal value of the stator peak voltage, the integrator gain can be modified:

$$K_{\mathrm{rs\_id}} = -\frac{\alpha_{\mathrm{Q}}}{3U_{\mathrm{s_{nom}}}}. \tag{A.24}$$

- **Rotational speed control**

The WT rotational speed control scheme is described in detail in Section 2.2.4, where the generator torque is used as an input for the mechanical subsystem. In this context, the generator torque in Equation (2.17) is assumed to be equal to the reference generator torque, defined by the speed control system; $T_{\mathrm{g}} = T_{\mathrm{g}}^{\mathrm{ref}}$.

The reference q-axis current can be found as

$$I_{\mathrm{rq}}^{\mathrm{ref}} = \frac{2T_{\mathrm{g}}^{\mathrm{ref}}}{3p\Psi_{\mathrm{s\_est}}}. \tag{A.25}$$

The stator flux can be defined

$$\Psi_{\mathrm{s\_est}} = \int U_{\mathrm{s\_ph}} - I_{\mathrm{s}}R_{\mathrm{s}}dt\ . \tag{A.26}$$

In order to avoid DC drift problems associated with the ideal integrator, the estimation of the stator flux is carried out by implementing a low-pass filter, as proposed in (AnalogDevices, 2000), (Hu, 1997)

$$y = \frac{1}{s+\omega_{\mathrm{c}}}x + \frac{\omega_{\mathrm{c}}}{s+\omega_{\mathrm{c}}}y, \tag{A.27}$$

where y is the estimated stator flux $\Psi_{\mathrm{s\_est}}$, x is $U_{\mathrm{s\_ph}} - I_{\mathrm{s}}R_{\mathrm{s}}$, and ω_{c} is the cut-off frequency of the low-pass filter.

The first component of the right-hand side of Equation (A.27) is the low-pass filter, and the second component is responsible for the feedback compensation of the filter output.

- **D-q axis current control**

Thus, by substituting the stator current I_{s} (Equation (A.12)) and the rotor flux Ψ_{R} (Equation (A.13)) into Equations (A.8) and (A.9), the following voltage equations can be obtained

$$U_{\mathrm{s}} = R_{\mathrm{s}}\left(\frac{\Psi_{\mathrm{s}}}{L_{\mathrm{M}}} - I_{\mathrm{R}}\right) + j\omega_{\mathrm{s}}\Psi_{\mathrm{s}} + \frac{d\Psi_{\mathrm{s}}}{dt} = \tag{A.28}$$

$$= -R_{\mathrm{s}}I_{\mathrm{R}} + \Psi_{\mathrm{s}}\left(\frac{R_{\mathrm{s}}}{L_{\mathrm{M}}} + j\omega_{\mathrm{s}}\right) + \frac{d\Psi_{\mathrm{s}}}{dt},$$

$$U_{\mathrm{R}} = R_{\mathrm{R}} I_{\mathrm{R}} + \frac{d\Psi_{\mathrm{s}}}{dt} + L_{\sigma}\frac{dI_{\mathrm{R}}}{dt} + j\omega_{\mathrm{slip}}\Psi_{\mathrm{s}} + j\omega_{\mathrm{slip}}L_{\sigma}I_{\mathrm{R}} =$$
$$= \left(R_{\mathrm{R}} + j\omega_{\mathrm{slip}}L_{\sigma}\right) I_{\mathrm{R}} + \frac{d\Psi_{\mathrm{s}}}{dt} + L_{\sigma}\frac{dI_{\mathrm{R}}}{dt} + j\omega_{\mathrm{slip}}\Psi_{\mathrm{s}} = \quad (A.29)$$
$$= \left(R_{\mathrm{R}} + R_{\mathrm{s}} + j\omega_{\mathrm{slip}}L_{\sigma}\right) I_{\mathrm{R}} + L_{\sigma}\frac{dI_{\mathrm{R}}}{dt} + E,$$

where the EMF E is considered as a disturbance input of the system,

$$E = U_{\mathrm{s}} - \left(\frac{R_{\mathrm{S}}}{L_{\mathrm{M}}} + j\omega_{\mathrm{s}}\right)\Psi_{\mathrm{s}}. \quad (A.30)$$

Let us assume that the plant is given by the following expression

$$U_{\mathrm{R}} = \left(R_{\mathrm{R}} + R_{\mathrm{s}}\right) I_{\mathrm{R}} + L_{\sigma}\frac{dI_{\mathrm{R}}}{dt}. \quad (A.31)$$

Thus, the first-order system with the input parameter U_{R} and the state parameter I_{R} will be written as

$$L_{\sigma}\frac{dI_{\mathrm{R}}}{dt} = U_{\mathrm{R}} - \left(R_{\mathrm{R}} + R_{\mathrm{s}}\right) I_{\mathrm{R}}. \quad (A.32)$$

The transfer function from the rotor voltage U_{R} to the rotor current I_{R} is

$$G(p) = \frac{1}{pL_{\sigma} + R_{\mathrm{R}} + R_{\mathrm{s}}}. \quad (A.33)$$

To decouple $\omega_{\mathrm{slip}}L_{\sigma}I_{\mathrm{R}}$ in Equation (A.29), the feedforward component should be added to the control system. Similarly, to compensate the error in the back EMF disturbances, the estimated E_{est} should be added as a feedforward signal.

In (Petersson, 2005), in order to improve the damping of the back EMF E, an active resistance is introduced to the system so that

$$U_{\mathrm{R}} = U'_{\mathrm{R}} - R_{\mathrm{a}} I_{\mathrm{R}}. \quad (A.34)$$

Thus, taking into account the feedforward components, the latter equation is modified as

$$U_{\mathrm{R}} = U'_{\mathrm{R}} + \left(j\omega_{\mathrm{slip}} L_{\sigma} - R_{\mathrm{a}}\right) I_{\mathrm{R}} + E_{\mathrm{est}}, \tag{A.35}$$

where U'_{R} is the voltage control signal before the feedforward compensation terms, that is, the controller output (Figure A.2)

$$U'_{\mathrm{R}} = K_{\mathrm{rc\_pq}} e + K_{\mathrm{rc\_iq}} \int e dt \, . \tag{A.36}$$

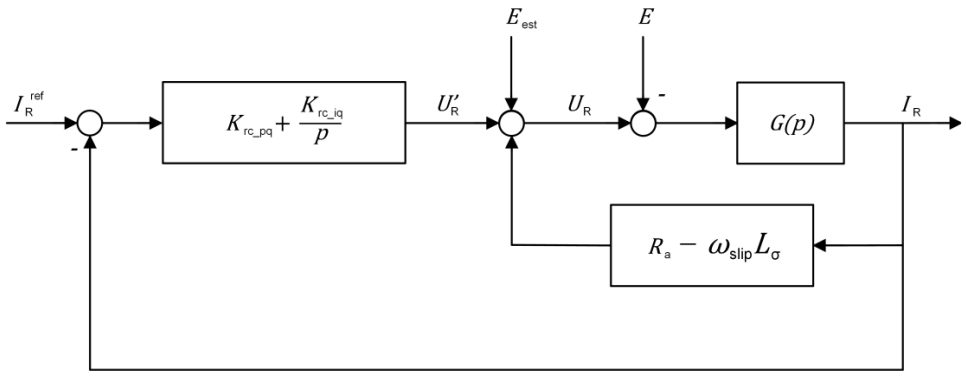

Figure A.2: DFIG control system with the introduced active damping using R_{a}.

Thus, taking into account the active resistance R_{a}, the plant model is modified as

$$G(p) = \frac{1}{pL_{\sigma} + R_{\mathrm{R}} + R_{\mathrm{S}} + R_{\mathrm{a}}}. \tag{A.37}$$

In order to define the integral and proportional gains of the current controller, the concept of the internal model control (IMC) is used. In this context, the controller transfer function is derived based on the plant inverse model $G^{-1}(p)$ and is written as

$$C(p) = \frac{\alpha}{p} G^{-1}(p) = K_{\mathrm{rc\_pq}} + \frac{K_{\mathrm{rc\_iq}}}{p}, \tag{A.38}$$

where α is the desired bandwidth of the closed-loop system

$$\alpha = \frac{ln9}{t_{\text{rise}}}. \tag{A.39}$$

Thus, the controller transfer function is

$$C(p) = \frac{\alpha}{p}(pL_\sigma + R_\text{R} + R_\text{s} + R_\text{a}) = \alpha\, L_\sigma + \frac{\alpha(R_\text{R}+R_\text{s}+R_\text{a})}{p}. \tag{A.40}$$

The proportional and integral gains, correspondingly, are

$$K_{\text{rc\_pq}} = \alpha\, L_\sigma, \tag{A.41}$$

$$K_{\text{rc\_iq}} = \alpha(R_\text{R} + R_\text{s} + R_\text{a}), \tag{A.42}$$

$$K_{\text{rc\_pd}} = \alpha\, L_\sigma, \tag{A.43}$$

$$K_{\text{rc\_id}} = \alpha(R_\text{R} + R_\text{s} + R_\text{a}). \tag{A.44}$$

Finally, the decoupled components of the reference rotor voltage

$$U_\text{rd}^\text{ref} = U'_\text{rd} - \omega_\text{slip} L_\sigma I_\text{Rq} - R_\text{a} I_\text{Rd} + E_{\text{est\_d}}, \tag{A.45}$$

$$E_{\text{est\_d}} = U_\text{sd} - \Psi_{\text{s\_est}} \frac{R_\text{s}}{L_\text{M}}, \tag{A.46}$$

$$U_\text{rq}^\text{ref} = U'_\text{rq} + \omega_\text{slip} L_\sigma I_\text{Rd} - R_\text{a} I_\text{Rq} + E_{\text{est\_q}}, \tag{A.47}$$

$$E_{\text{est\_q}} = U_{\text{sq}} - \Psi_{\text{s\_est}}\omega_{\text{slip}}. \quad \text{(A.48)}$$

B. GSC control scheme

The control system for the GSC consists of outer loops for the DC link voltage and reactive power control and an inner loop for the current control.

- **DC link voltage control**

The DC link voltage control is derived based on Equation (3.29), where the term P_{f} can be approximated as

$$P_{\text{f}} \approx 3I_{\text{fd}}U_{\text{gd}}\,, \quad \text{(A.49)}$$

where I_{fd} is the filter current on the converter side and U_{gd} is the filter voltage supplied from the grid side.

The active damping of the input disturbances can be added so that

$$I_{\text{fd}}^{\text{ref}} = I_{\text{fd}}'^{\,\text{ref}} + G_{\text{a}}\,, \quad \text{(A.50)}$$

where G_{a} is the active damping term.

Thus, the filter power in Equation (A.49) can be rewritten as

$$P_{\text{f}} = 3I_{\text{fd}}'U_{\text{gd}} + 3G_{\text{a}}U_{\text{gd}}\,. \quad \text{(A.51)}$$

Choosing the reference control input as $W = U_{\text{DC}}^2$, Equation (3.29) can be rewritten as

$$\frac{1}{2}C_{\text{DC}}\frac{dW}{dt} = \left(3I_{\text{fd}}'U_{\text{gd}} + 3G_{\text{a}}U_{\text{gd}}\right) + P_{\text{r}}. \quad \text{(A.52)}$$

Considering the rotor power P_{r} as the disturbance input, the transfer function from W to $I_{\text{fd}}'^{\,\text{ref}}$ can be derived

$$G(p) = \frac{6E_{\mathrm{gd}}}{pC_{\mathrm{DC}} + 3G_{\mathrm{a}}U_{\mathrm{gd}}}. \tag{A.53}$$

The proportional and integral gains of the PI controller are expressed as

$$K_{\mathrm{qc\_pw}} = \frac{\alpha_W C_{\mathrm{DC}}}{6U_{\mathrm{gd}}}, \tag{A.54}$$

$$K_{\mathrm{qc\_iw}} = \alpha_W G_{\mathrm{a}}. \tag{A.55}$$

The active damping is chosen as

$$G_{\mathrm{a}} = \frac{\alpha_W C_{\mathrm{DC}}}{6U_{\mathrm{gd}}}. \tag{A.56}$$

- **Current control**

Assuming that the resonant frequencies are damped by the control system, the LCL filter can be simplified as shown in Figure A.3.

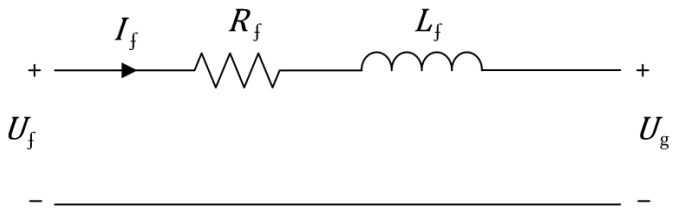

Figure A.3: Simplified equivalent circuit of the LCL filter.

The resistance R_{f} and the inductance L_{f} are defined as

$$R_{\mathrm{f}} = R_{\mathrm{f1}} + R_{\mathrm{f2}}, \tag{A.57}$$

$$L_{\mathrm{f}} = L_{\mathrm{f1}} + L_{\mathrm{f2}} . \quad \text{(A.58)}$$

The circuit can be described by Kirchhoff's voltage law

$$U_{\mathrm{g}} = -(R_{\mathrm{f}} + j\omega_{\mathrm{f}} L_{\mathrm{f}}) I_{\mathrm{f}} - L_{\mathrm{f}} \frac{dI_{\mathrm{f}}}{dt} + U_{\mathrm{f}} . \quad \text{(A.59)}$$

The latter expression can be rewritten in the form

$$L_{\mathrm{f}} \frac{dI_{\mathrm{f}}}{dt} = U_{\mathrm{f}} - (R_{\mathrm{f}} + j\omega_{\mathrm{f}} L_{\mathrm{f}}) I_{\mathrm{f}} - U_{\mathrm{g}} . \quad \text{(A.60)}$$

Including active damping, the filter voltage measured from the GSC side can be presented as

$$U_{\mathrm{f}} = U'_{\mathrm{f}} - (R_{\mathrm{f}} + j\omega_{\mathrm{f}} L_{\mathrm{f}}) I_{\mathrm{f}} . \quad \text{(A.61)}$$

Assuming U_{g} as a disturbance, the transfer function $G_{I_{\mathrm{f}} U_{\mathrm{f}}}(p)$ from the filter current I_{f} to the voltage U_{f} is derived based on Equation (A.61)

$$G_{I_{\mathrm{f}} U_{\mathrm{f}}}(p) = \frac{1}{L_{\mathrm{f}} p + R_{\mathrm{f}} + R_{\mathrm{af}}}, \quad \text{(A.62)}$$

where R_{af} is the damping resistance

$$R_{\mathrm{af}} = \alpha_{\mathrm{f}} L_{\mathrm{f}} - R_{\mathrm{f}}, \quad \text{(A.63)}$$

where α_{f} is the bandwidth of the current controller.

According to the IMC concept, the transfer function of the controller should be derived as

$$C(p) = \frac{\alpha_{\mathrm{f}}}{p} G^{-1}_{I_{\mathrm{f}} U_{\mathrm{f}}}(p) , \quad \text{(A.64)}$$

$$C(p) = \frac{\alpha_{\mathrm{f}}}{p}(L_{\mathrm{f}}p + R_{\mathrm{f}} + R_{\mathrm{af}}) = \alpha_{\mathrm{f}}L_{\mathrm{f}} + \frac{R_{\mathrm{f}}+R_{\mathrm{af}}}{p} \ . \tag{A.65}$$

Therefore, the proportional and integral gains are expressed as

$$K_{\mathrm{qc\_pd}} = \alpha_{\mathrm{f}}L_{\mathrm{f}} \ , \tag{A.66}$$

$$K_{\mathrm{qc\_id}} = \alpha_{\mathrm{f}}(R_{\mathrm{f}} + R_{\mathrm{af}}) = \alpha_{\mathrm{f}}^2 L_{\mathrm{f}} \ . \tag{A.67}$$

Finally, the d-q axis voltage components can be derived

$$\begin{aligned} U_{\mathrm{fd}}^{\mathrm{ref}} = {} & K_{\mathrm{qc\_pd}}\left(I_{\mathrm{fd}}^{\mathrm{ref}} - I_{\mathrm{fd}}\right) \\ & + K_{\mathrm{qc\_id}} \int \left(I_{\mathrm{fd}}^{\mathrm{ref}} - I_{\mathrm{fd}}\right)dt + U_{\mathrm{fd}} - I_{\mathrm{fd}} R_{\mathrm{qc\_a}} \\ & - I_{\mathrm{cfd}}R_{\mathrm{res\_a}} - \omega_{\mathrm{f}}I_{\mathrm{fq}}L_{\mathrm{f1}} \end{aligned} \tag{A.68}$$

$$U_{\mathrm{fq}}^{\mathrm{ref}} = K_{\mathrm{qc\_pq}}\left(I_{\mathrm{fq}}^{\mathrm{ref}} - I_{\mathrm{fq}}\right) + K_{\mathrm{qc\_iq}} \int \left(I_{\mathrm{fq}}^{\mathrm{ref}} - I_{\mathrm{fq}}\right)dt + U_{\mathrm{fq}} - I_{\mathrm{fq}} R_{\mathrm{qc\_a}} - I_{\mathrm{cfq}}R_{\mathrm{res\_a}} - \omega_{\mathrm{f}}I_{\mathrm{fd}}L_{\mathrm{f1}} \ . \tag{A.69}$$

Appendix B: Procedure of selecting the wind turbine parameters for the aerodynamic block

An approach to calculate the wind turbine parameters is to start with the initial information that is already known. Thus, the 2 MW wind turbine with the maximum power coefficient $C_{\mathrm{p\_max}}$ of 0.48 and the optimal tip speed ratio $\lambda_{\mathrm{opt}} = 8.1$ is given. Considering the appropriate value for the nominal wind speed, v_{nom} = 11 m/s could be the starting choice. It corresponds to the wind turbine rotor radius of 40.3, according to Equations (B.1) and (B.2).

$$r = \sqrt{\frac{P_{\mathrm{m\_nom}}}{\frac{1}{2}\rho\pi C_{\mathrm{p\_max}}\, {v_{\mathrm{nom}}}^3}}, \tag{B.1}$$

$$r = \sqrt{\frac{2\ \mathrm{MW}}{\frac{1}{2}\cdot 1.225\ \frac{\mathrm{kg}}{\mathrm{m}^2}\cdot\pi\cdot 0.48\cdot\left(11\ \frac{\mathrm{m}}{\mathrm{s}}\right)^3}} = 40.3\ \mathrm{m} \tag{B.2}$$

Therefore, the nominal rotational speed can be calculated by

$$\omega_{\mathrm{m\_nom}} = \frac{v_{\mathrm{nom}}\lambda_{\mathrm{opt}}}{r}, \tag{B.3}$$

$$\omega_{\mathrm{m\_nom}} = \frac{11\,\frac{\mathrm{m}}{\mathrm{s}}\cdot 8.1}{40.3\ \mathrm{m}} = 2.21\ \frac{\mathrm{rad}}{\mathrm{s}}. \tag{B.4}$$

The corresponding generator torque can be found in Figure B.1 (point 1) as an optimal operating point (equilibrium point of the aerodynamic and generator torques) at the wind speed 11 m/s and the rotational speed 2.21 rad/s, or calculated using Equation (B.5).

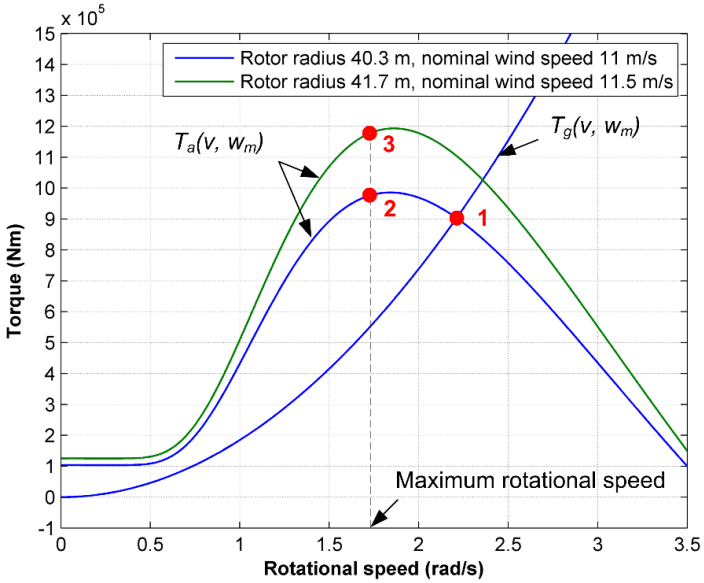

Figure B.1: Effect of the changed rotor radius and nominal wind speed on the aerodynamic torque curves.

$$T_{\mathrm{g\_nom}} = \frac{P_{\mathrm{m\_nom}}}{\omega_{\mathrm{m\_nom}}}, \tag{B.5}$$

$$T_{\mathrm{g\_nom}} = \frac{2\ MW}{2.21\ \frac{\mathrm{rad}}{\mathrm{s}}} = 9.05\ \cdot 10^5\ \mathrm{N \cdot m}\,. \tag{B.6}$$

However, the maximum rotational speed $\omega_{\mathrm{m\_max}}$ is limited by the slip operating range. The maximum rotational speed $\omega_{\mathrm{m\_max}}$ can be reached at the minimum generator slip s_{min}, and it is calculated as follows

$$\omega_{\mathrm{m\_max}} = \frac{2\pi\ (1 - s_{\mathrm{min}})}{N_{\mathrm{gear}} n_{\mathrm{p}}}, \tag{B.7}$$

where the gear ratio is $k_{\mathrm{ls\_hs}}$ = 100, and the number of pole pairs is n_{p} = 2. The minimum slip $s_{\mathrm{min}} = -0.1$.

$$\omega_{\text{m\_max}} = \frac{2\pi \cdot (1-(-0.1))}{100 \cdot 2} = 1.728 \frac{\text{rad}}{\text{s}}. \quad \text{(B.8)}$$

At the rotational speed $\omega_{\text{m\_max}} = 1.728$ rad/s and the nominal wind speed v_{nom} = 11 m/s, the aerodynamic torque is $T_{\text{a\_point2}}$ = 9.76 $\cdot 10^5$ N·m (point 2 in Figure B.1) and the mechanical power is

$$P_{\text{m\_point2}} = T_{\text{a\_point2}} \omega_{\text{m\_max}}, \quad \text{(B.9)}$$

$$P_{\text{m\_point2}} = 9.76 \cdot 10^5 \, Nm \cdot 1.728 \frac{rad}{s} = 1.69 \text{ MW}. \quad \text{(B.10)}$$

Therefore, in order to reach the nominal power at the rotational speed $\omega_{\text{m\_max}}$, the aerodynamic torque should be increased. In this case, the required aerodynamic torque $T_{\text{a\_req}}$ is

$$T_{\text{a\_req}} = \frac{P_{\text{m\_nom}}}{\omega_{\text{m\_max}}}, \quad \text{(B.11)}$$

$$T_{\text{a\_req}} = \frac{2 \, MW}{1.728 \frac{rad}{s}} = 1.16 \cdot 10^6 \, N \cdot m. \quad \text{(B.12)}$$

In order to increase the aerodynamic torque at the constant rotational speed $\omega_{\text{m\_max}}$, it is reasonable to increase the nominal wind speed and/or increase the wind turbine rotor radius. By the "trial and error" method, the final values for the nominal wind speed and the rotor radius are 11.5 m/s and 41.7 m, respectively. These parameters correspond to the aerodynamic torque $T_{\text{a\_nom\_final}} = 1.18 \cdot 10^6$ N·m (point 3 in Figure B.1) and the mechanical power $P_{\text{m\_nom\_final}} = 2.04$ MW.

Therefore, the aerodynamic and mechanical parameters are calculated in different operating modes, as shown in Table B.0.1.

Table B.0.1: Aerodynamic and mechanical parameters calculated in different operating modes.

Operating mode	Rotational speed (rad/s)	Wind speed (m/s)	Aerodynamic torque (kN·m)	Tip speed ratio	Power coefficient	Mechanical power (kW)
1	1.1	3.5	5.59	13.1	0.043	14.1
1	1.1	4	50.6	11.5	0.260	60.6
1	1.1	4.5	108	10.2	0.389	118
1	1.1	5	173	9.2	0.454	182
1	1.1	5.5	242	8.3	0.479	246
1	1.1	5.7	265	8.1	0.481	292
2	1.2	6.2	315	8.1	0.480	378
2	1.3	6.7	370	8.1	0.480	481
2	1.4	7.2	430	8.1	0.482	602
2	1.5	7.7	493	8.1	0.481	740
2	1.6	8.2	561	8.1	0.481	897
2	1.7	8.7	633	8.1	0.481	1080
2	1.728	8.9	654	8.1	0.481	1130
3	1.728	9	677	8.0	0.480	1170
3	1.728	9.5	786	7.6	0.474	1360
3	1.728	10	893	7.2	0.461	1540
3	1.728	10.5	994	6.9	0.444	1720
3	1.728	11	1090	6.5	0.423	1880
3	1.728	11.5	1180	6.3	0.400	2040

Appendix C: Calculating the wind turbine total inertia

The moments of inertia of the wind turbine components are listed in Table C.0.1 (Luo, 2014).

Table C.0.1: Moments of inertia of the wind turbine components.

Item	Moment of inertia (kgm^2)
Blade, J_b	1.13×10^6
Hub, J_h	6.03×10^4
Gearbox, J_{gb}	4.26×10^5
Rotor of DFIG, J_r	75

Taking into account that the moment of inertia of the rotor is given for the high-speed side of the machine shaft and referring all components to the low-speed side, the total inertia can be calculated as follows

$$J_{tot} = 3 \cdot J_b + J_h + J_{gb} + N_{gear}^2 \cdot J_r, \quad \text{(C.1)}$$

where N_{gear} is the gear ratio, $N_{gear} = 100$

$$J_{tot} = 3 \cdot 1.13 \cdot 10^6 + 6.03 \cdot 10^4 + 4.26 \cdot 10^5 + 100^2 \cdot 75 = 4.626 \cdot 10^6. \quad \text{(C.2)}$$

ACTA UNIVERSITATIS LAPPEENRANTAENSIS

731. SAVOLAINEN, JYRKI. Analyzing the profitability of metal mining investments with system dynamic modeling and real option analysis. 2016. Diss.

732. LAMPINEN, MATTI. Development of hydrometallurgical reactor leaching for recovery of zinc and gold. 2016. Diss.

733. SUHOLA, TIMO. Asiakaslähtöisyys ja monialainen yhteistyö oppilashuollossa: oppilashuoltoprosessi systeemisenä palvelukokonaisuutena. 2017. Diss.

734. SPODNIAK, PETR. Long-term transmission rights in the Nordic electricity markets: An empirical appraisal of transmission risk management and hedging. 2017. Diss.

735. MONTONEN, JUHO. Integrated hub gear motor for heavy-duty off-road working machines – Interdisciplinary design. 2017. Diss.

736. ALMANASRAH, MOHAMMAD. Hot water extraction and membrane filtration processes in fractionation and recovery of value-added compounds from wood and plant residues. 2017. Diss.

737. TOIVANEN, JENNI. Systematic complaint data analysis in a supply chain network context to recognise the quality targets of welding production. 2017. Diss.

738. PATEL, GITESHKUMAR. Computational fluid dynamics analysis of steam condensation in nuclear power plant applications. 2017. Diss.

739. MATTHEWS, SAMI. Novel process development in post-forming of an extruded wood plastic composite sheet. 2017. Diss.

740. KÄHKÖNEN, TOMMI. Understanding and managing enterprise systems integration. 2017. Diss.

741. YLI-HUUMO, JESSE. The role of technical dept in software development. 2017. Diss.

742. LAYUS, PAVEL. Usability of the submerged arc welding (SAW) process for thick high strength steel plates for Arctic shipbuilding applications. 2017. Diss.

743. KHAN, RAKHSHANDA. The contribution of socially driven businesses and innovations to social sustainability. 2017. Diss.

744. BIBOV, ALEKSANDER. Low-memory filtering for large-scale data assimilation. 2017. Diss.

745. ROTICH, NICOLUS KIBET. Development and application of coupled discrete and continuum models in solid particles classification. 2017. Diss.

746. GAST, JOHANNA. The coopetition-innovation nexus: Investigating the role of coopetition for innovation in SMEs. 2017. Diss.

747. KAPOOR, RAHUL. Competition and disputes in the patent life cycle. 2017. Diss.

748. ALI-MARTTILA, MAAREN. Towards successful maintenance service networks – capturing different value creation strategies. 2017. Diss.

749. KASHANI, HAMED TASALLOTI. On dissimilar welding: a new approach for enhanced decision-making. 2017. Diss.

750. MVOLA BELINGA, ERIC MARTIAL. Effects of adaptive GMAW processes: performance and dissimilar weld quality. 2017. Diss.

751. KARTTUNEN, JUSSI. Current harmonic compensation in dual three-phase permanent magnet synchronous machines. 2017. Diss.

752. SHI, SHANSHUANG. Development of the EAST articulated maintenance arm and an algorithm study of deflection prediction and error compensation. 2017. Diss.

753. CHEN, JIE. Institutions, social entrepreneurship, and internationalization. 2017. Diss.

754. HUOTARI, PONTUS. Strategic interaction in platform-based markets: An agent-based simulation approach. 2017. Diss.

755. QU, BIN. Water chemistry and greenhouse gases emissions in the rivers of the "Third Pole" / Water Tower of Asia". 2017. Diss.

756. KARHU, PÄIVI. Cognitive ambidexterity: Examination of the cognitive dimension in decision-making dualities. 2017. Diss.

757. AGAFONOVA, OXANA. A numerical study of forest influences on the atmospheric boundary layer and wind turbines. 2017. Diss.

758. AZAM, RAHAMATHUNNISA MUHAMMAD. The study of chromium nitride coating by asymmetric bipolar pulsed DC reactive magnetron sputtering. 2017. Diss.

759. AHI, MOHAMADALI. Foreign market entry mode decision-making: Insights from real options reasoning. 2017. Diss.

760. AL HAMDI, ABDULLAH. Synthesis and comparison of the photocatalytic activities of antimony, iodide and rare earth metals on SnO2 for the photodegradation of phenol and its intermediates under UV, solar and visible light irradiations. 2017. Diss.

761. KAUTTO, JESSE. Evaluation of two pulping-based biorefinery concepts. 2017. Diss.

762. AFZALIFAR, ALI. Modelling nucleating flows of steam. 2017. Diss.

763. VANNINEN, HEINI. Micromultinationals - antecedents, processes and outcomes of the multinationalization of small- and medium-sized firms. 2017. Diss.

764. DEVIATKIN, IVAN. The role of waste pretreatment on the environmental sustainability of waste management. 2017. Diss.

765. TOGHYANI, AMIR. Effect of temperature on the shaping process of an extruded wood-plastic composite (WPC) profile in a novel post-production process. 2017. Diss.

766. LAAKKONEN, JUSSI. An approach for distinct information privacy risk assessment. 2017. Diss.

767. KASURINEN, HELI. Identifying the opportunities to develop holistically sustainable bioenergy business. 2017. Diss.

768. KESKISAARI, ANNA. The impact of recycled raw materials on the properties of wood-plastic composites. 2017. Diss.

769. JUKKA, MINNA. Perceptions of international buyer-supplier relational exchange. 2017. Diss.